Radiation Induced Nonlinear Optical Effects in Optical Glasses and Sapphire

by

Bryan William Morgan

A dissertation submitted in partial fulfillment
of the requirements for the degree of
Doctor of Philosophy
(Nuclear Engineering and Radiological Sciences)
at the University of Michigan
2022

Doctoral Committee:

Professor Igor Jovanovic, Chair
Assistant Research Scientist Milos Burger
Professor Annalisa Manera
Dr. Piyush Sabharwall, Idaho National Laboratory
Professor Louise Willingale

Bryan William Morgan

bryanmo@umich.edu

ORCID ID: 0000-0002-2466-8764

To Phyllis

Acknowledgments

I would like to acknowledge Professor Igor Jovanovic, who advised me on both my masters and PhD studies, encouraged me to pursue an education at the PhD level, and has taught me so much about responsible engineering. Dr. Milos Burger provided constant mentorship in the laboratory and throughout my PhD studies, and has guided me through many challenging portions of my studies and research. I greatly appreciate the United States Army and my leaders there, military and civilian, who have afforded me the career opportunities I've had in service to the United States, to include graduate level education. The faculty and staff the the Ohio State University Nuclear Reactor Laboratory, specifically Professor Raymond Cao, Matthew Van Zile, Joel Hatch, Kevin Herminghuysen, Susan White, Andrew Kauffman, and Maria McGraw were all essential to the success of this research and it was simply a pleasure to work with all of them. I thank my loving parents for raising me and supporting me throughout my life. Finally, I am extremely grateful for my loving wife and children, who bring me so much joy every day.

Contents

List of Figures

List of Tables

List of Abbreviations

AES atomic emission spectroscopy.

ANSIL Applied Nuclear Science Instrumentation Laboratory.

CA closed-aperture.

CMOS complimentary metal oxide semiconductor.

CW continuous-wave.

DAQ data acquisition.

HPGe high purity germanium.

I302 Infrasil 302.

ICF inertial confinement fusion.

LIBS laser-induced breakdown spectroscopy.

NBOHC nonbridging oxygen-hole center.

NLA nonlinear absorption.

NLR nonlinear refraction.

NRL Nuclear Reactor Laboratory.

OA open-aperture.

OD optical density.

ODC oxygen deficient center.

OSU Ohio State University.

PIE post-irradiation examination.

PSU Pennsylvania State University.

RIA radiation induced attenuation.

RSEC Radiation Science and Engineering Center.

S2000 Spectrosil 2000.

SA saturable absorption.

TPA two-photon absorption.

UM University of Michigan.

UV ultraviolet.

VISTA Vehicle for Interplanetary Space Transportation Application.

Abstract

Advanced fast fission reactors, such as molten salt and liquid metal cooled reactors, offer enhanced safety and economic efficiency for commercial as well as emerging space nuclear power generation. Novel optical instrumentation has the potential to significantly enhance both the safety and economic efficiency of these advanced fission reactors. In the area of inertial confinement fusion energy, laser-driven systems require the placement of final optics in proximity of the target area. Laser-driven accelerator applications can also benefit from the use of optics for diagnostics purposes. Optical instruments deployed in such harsh radiation environments require careful material selection for high transparency and consistent performance under exposure to intense radiation and thermal conditions. This work experimentally evaluates the suitability of several optical materials for use in nuclear environments.

One technique that has been proposed for instrumentation in high-temperature gas-cooled reactors is laser-induced breakdown spectroscopy (LIBS), where it can identify trace chemical signatures within the coolant indicative of corrosion and material failure. In addition to the material indices of refraction and absorption, the material's nonlinear properties are also important in intense laser applications such as LIBS and laser-driven inertial confinement fusion, where high-power laser pulses traverse optical media.

This research presents a study of the linear and nonlinear optical characteristics of fused silica, sapphire, and borosilicate glasses under the nearly simultaneous conditions of irradiation and thermal annealing. A mobile post-irradiation examination (PIE) system

was developed to evaluate optical materials at the site of irradiation, reducing the delay between optical material irradiation, thermal annealing, and examination. The PIE system consists of a self-contained Z-scan setup that measures nonlinear refraction and nonlinear absorption, and a spectroscopy setup to measure linear attenuation. The PIE system was developed and validated at the University of Michigan, while the optical sample irradiation and thermal annealing is performed at the Ohio State University Nuclear Reactor Laboratory.

This study presents evidence for radiation-induced negative nonlinear absorption (NLA) in fused silica, sapphire, and borosilicate glasses consistent with the saturable absorption (SA) effect. Significant residual radiation-induced attenuation (RIA) is observed in low-OH fused silica and sapphire that may be explained by the competition between radiation damage and thermal annealing. The negative NLA coefficients suggest a benefit to instrument performance at high peak laser powers since they can counteract some of the RIA.

Chapter 1

Introduction

1.1 Motivation

The performance of optical materials in harsh radioactive and thermal environments is of great importance for optical instrumentation deployed in advanced fission and fusion reactor systems [1, 2], accelerators [3], and space applications [4]. An example of such instrumentation is LIBS, which relies upon the application of high-power laser pulses and spectroscopic measurements and has been implemented broadly in applications across industries that include undersea and outer space exploration [5]. The development of LIBS-based optical sensors for the nuclear fission power generation industry and for spent nuclear fuel analysis has the potential to significantly enhance the safety and economic efficiency of nuclear reactors through the provision of online and *in-situ* monitoring of internal reactor conditions [2, 6]. Such real-time monitoring of fission reactor operating conditions has the potential to provide instantaneous critical information on the integrity of internal components, which could enhance safety and reduce the frequency of shut-downs for inspection.

High-power lasers are an enabling technology for the development of inertial confinement fusion (ICF). Lasers are used as "drivers" to initiate the implosion of fusion fuel

capsule in the ICF process, which is illustrated in Figure 1.1 [1]. Intense laser pulses are focused through a final focusing optic onto the surface of the fusion fuel capsule to implode the capsule to sufficient density and temperature to initiate the fusion process. The resulting fusion releases large amounts of energy in the form of high-energy neutrons, gamma-rays, X-rays, and ions, which are in return incident on the final focusing optics. The final focusing optic in an ICF system located 20 m from the fuel capsule may ex-

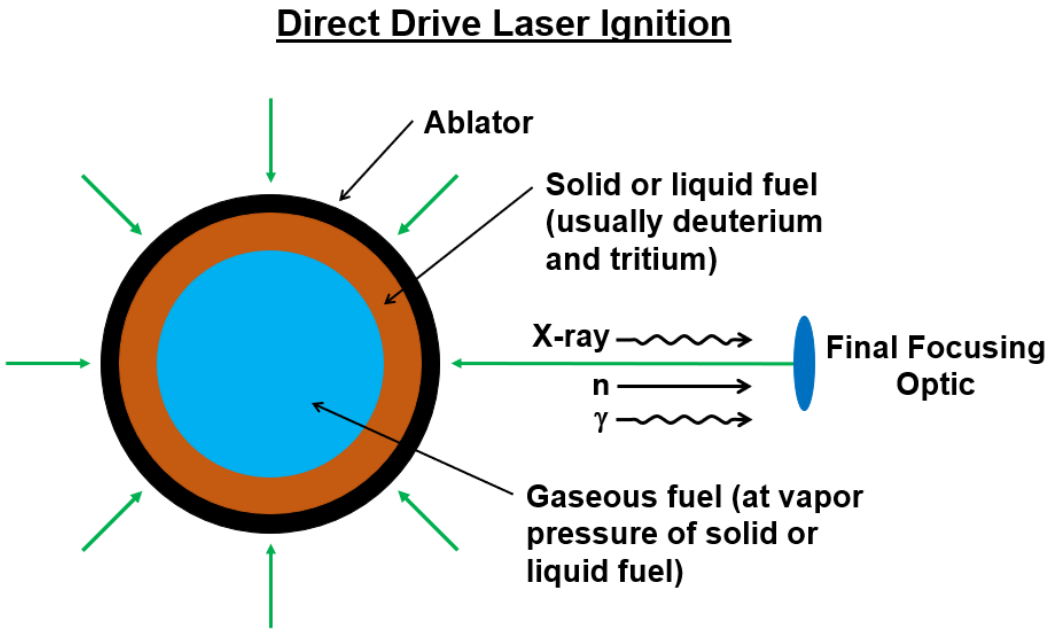

Figure 1.1: The ICF direct drive approach uses high-power lasers (green arrows) to drive implosion of a fusion fuel pellet encapsulated in an ablator shell [1].

perience both a total neutron flux of 2.1×10^{13} n $\cdot$ cm^{-2}s^{-1} and a gamma dose rate of 75.6 Mrad $\cdot$ hr^{-1}, which combined may cause significant radiation damage to the final focusing optics [1]. Both of these rates are $\approx$ 10 times greater than those produced in the OSU NRL research reactor and as will be seen in Chapters 4 and 5 can significantly alter the optical properties of bulk optical materials.

To evaluate the limits of operation of optical instrumentation and optical systems, a thorough understanding is needed of the radiation and thermal effects on various optical materials. Fused silica, sapphire, and borosilicate glass are common and well-

characterized materials used in many optical components, such as windows and lenses. These materials and their variants, such as high-OH and low-OH content fused silica and radiation-resistant borosilicate glass, have relatively well-understood linear optical properties such as the wavelength-dependent index of refraction and linear absorption. These properties, along with the mechanical characteristics, damage threshold, and cost govern the selection of materials for various applications [7, 8]. The linear optical properties of materials have been found to change when exposed to ionizing radiation, thermal annealing, or a combination of the two, manifesting as RIA [9], change of refractive index [10], and radiation-induced emission [11]. These radiation-induced changes have been extensively studied at various radiation doses, annealing temperatures, annealing times, and combinations of post-irradiation and concurrent-irradiation thermal annealing.

The nonlinear optical properties could have a similarly significant impact on applications that require high-power laser pulse propagation, and have been explored by various methods such as degenerate four-wave mixing, two-beam interferometry, and Z-scan, to name a few [12]. However, the ionizing radiation-induced changes of the nonlinear optical properties of materials have not seen the similar level of attention to date. Macroscopic nonlinear optical properties of materials depend on the light intensity and manifest as the NLR and NLA. They are usually parameterized as

$$n = n_0 + n_2 I_0, \tag{1.1}$$

$$\alpha = \alpha_0 + \beta I_0. \tag{1.2}$$

Here, n is the index of refraction, n_0 is the linear index of refraction, n_2 is the nonlinear index of refraction, α is the absorption coefficient, α_0 is the linear absorption coefficient, β is the NLA coefficient, and I_0 is the light intensity. The NLR index and NLA coefficient represent the aggregate effects of multiple components of the third-order nonlinear

susceptibility that contribute nonlinear optical phenomena such as two-photon absorption (TPA) [13], multiphoton absorption [13], SA [14], reverse saturable absorption [14], excited-state absorption [13], and thermal effects [13]. The NLR and NLA coefficients can be measured by the technique referred to as Z-scan [12, 13, 15], which simultaneously captures all constituent effects.

1.2 Laser-Induced Breakdown Spectroscopy

LIBS is a versatile method of elemental analysis based on atomic emission spectroscopy of laser-generated plasma [5]. Laser pulses are focused on a target sample surface to ionize a small portion of the material, resulting in the formation of plasma. The plasma, composed of ions, electrons and electronically excited atoms and molecules, emits light that can be spectrally resolved to reveal the elemental composition of the sample. The small isotope shift in atomic or molecular spectra can also be used to measure the isotopic composition. The LIBS method of elemental analysis is relatively simple and provides an *in-situ* sample evaluation capability that can be accomplished outside of an analytic laboratory with little to no sample preparation. This capability is of particular interest to applications that require rapid composition evaluation of liquids, gasses, and solids in a variety of environments, such as in nuclear counter-proliferation, reactor safety instrumentation and monitoring, and security [5].

The atomic emission spectroscopy (AES) is at the foundation of LIBS. Obtaining atomic emission from samples through ablation is minimally invasive when compared to destructive methods such as mass spectrometry. A number of heat sources may be used to vaporize the sample under analysis, but LIBS utilizes high intensity pulsed lasers to conduct AES. The resultant atomic emission spectrum is analyzed with a spectrometer. An example of a LIBS generated plasma in air is shown in Figure 1.2. The plasma in

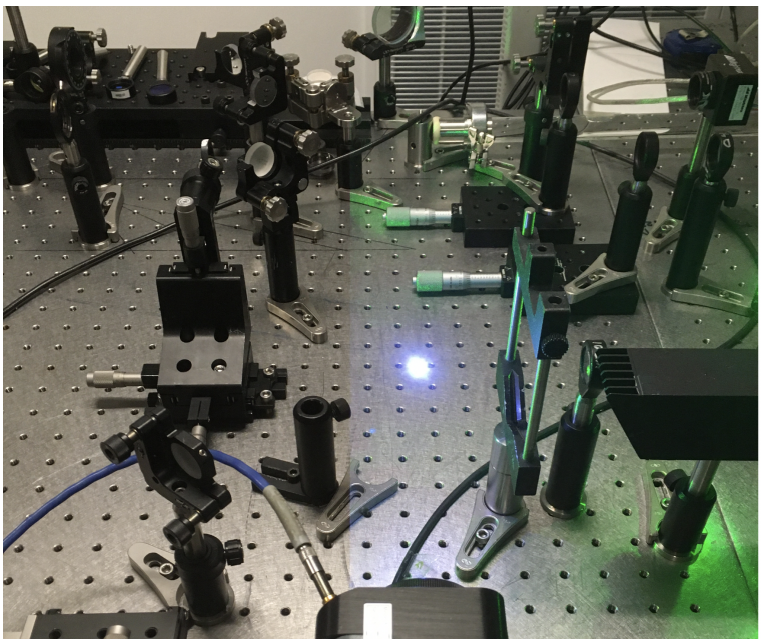

Figure 1.2: A laser spark generated in air by focusing a nanosecond laser.

Figure 1.2 is produced by focusing a ∼10-ns Nd:YAG laser. The plasma emission spectra are spectrally resolved, typically using a diffraction grating, before being imaged on a camera sensor.

The beam will ideally impact the LIBS target at the focal point to maximize plasma production and thus LIBS measurement. Accurate positioning the focal point of the laser on the surface of the target is essential for LIBS operation. The positioning is highly dependent on the known linear and nonlinear optical properties of the material the lens is composed of. In a nuclear reactor environment, the alteration of these optical properties can alter these properties significantly enough to not only change the focal position of the LIBS laser, but also change the amount of light transmitted to the spectrometer for analysis, as will be discussed later in this chapter.

The characteristic emission emitted by the laser-generated plasma must be resolved, recorded, and interpreted as part of the AES process and LIBS measurement. The minimum instrumentation involved in this process includes a spectrograph to spectrally

resolve the plasma light emission into its constituent wavelengths, and a detector to record the spectrally resolved emission spectra by wavelength or energy. Additional instrumentation to augment implementation of the LIBS measurement includes optics to collect the characteristic emission and transport it to the spectrograph. Again, with collection and transmission optics the radiation and thermally altered properties of the optical materials may have significant impact on the interpretation of the LIBS emission spectrum when the measurement is performed in a nuclear environment [2]. Attenuation within the fiber will alter the peak magnitudes of emission spectra in LIBS, skewing the results and possibly providing erroneous estimates of the chemical composition of the target if the attenuation is not accounted for. The spectrometer and laser would ideally have standoff to be isolated from exposure to radiation and extreme temperatures, but to accomplish standoff transmission and collection optical components would be utilized and exposed to ionizing radiation and high temperatures. A representation of a typical LIBS experimental setup with standoff optical components such as the focusing lens and transmission fibers is provided in Figure 1.3 [5].

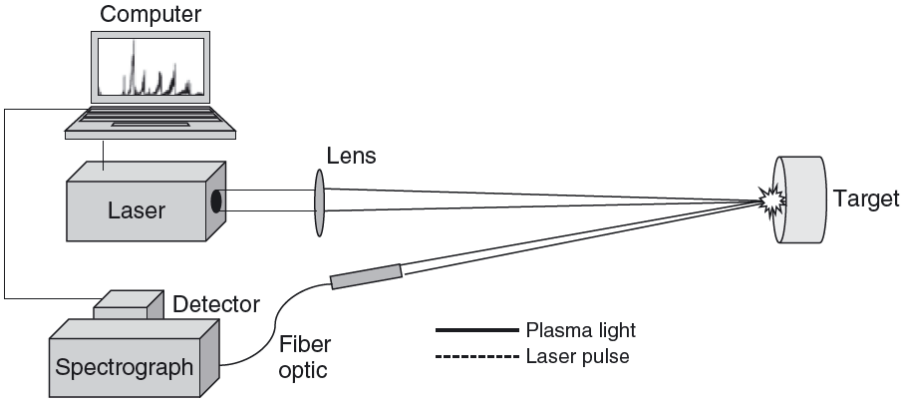

Figure 1.3: Basic equipment setup for a LIBS experiment [5].

1.3 Linear and Nonlinear Optical Material Properties

Linear optical properties of materials comprise the physical phenomena of refraction, reflection, absorption, emission, and scattering [16]. These phenomena, along with the material bandgap, govern how electromagnetic radiation is affected by transiting a medium or an interface between two different media. The linear properties of glasses are wavelength-dependent. Intensity-dependent nonlinear optical properties result largely from the third-order nonlinear optical susceptibility, which is the origin of the Kerr effect [17], third-harmonic generation [18], SA [14], and reverse SA [14]. These accumulated effects result in nonlinear optical effects such as NLR and NLA that alter the corresponding material refraction and absorption as described in Equations (1.1) and (1.2).

1.3.1 Linear Optical Properties

Refraction, reflection, absorption, emission, and scattering all affect the propagation of light as it transits a medium and transitions from one medium to another via an interface. The interaction of light with matter is described by Maxwell's equations, a consequence of which is the relation between the speed of light and refractive index:

$$v_p = c/n. \tag{1.3}$$

Here, c is the speed of light in vacuum and v_p is the phase velocity, which represents the speed of light in a medium with refractive index n. This example illustrates alteration of the speed of light based on the refractive index of the medium the light is traversing.

The material refractive index, n, originates from the interaction of the incident light with the electromagnetic field generated by the oscillating dipoles in the medium. This

effect can change the propagation direction of light as it transits the interface of two media, and likewise forms the basis for the phenomenon of reflection. The index of refraction is photon energy dependent, or wavelength dependent, and is frequently described using the Sellmeier equation:

$$n^2(\lambda) = 1 + \frac{B_1\lambda^2}{\lambda^2 - C_1} + \frac{B_2\lambda^2}{\lambda^2 - C_2} + \frac{B_3\lambda^2}{\lambda^2 - C_3}. \tag{1.4}$$

Here, B_i and C_i are the material-dependent Sellmeier coefficients. The dependence of the refractive index of on wavelength for fused silica, sapphire, and BK7 glass is plotted in Figure 1.4 as an example. The Sellmeier coefficients for these materials are provided in Table 1.1.

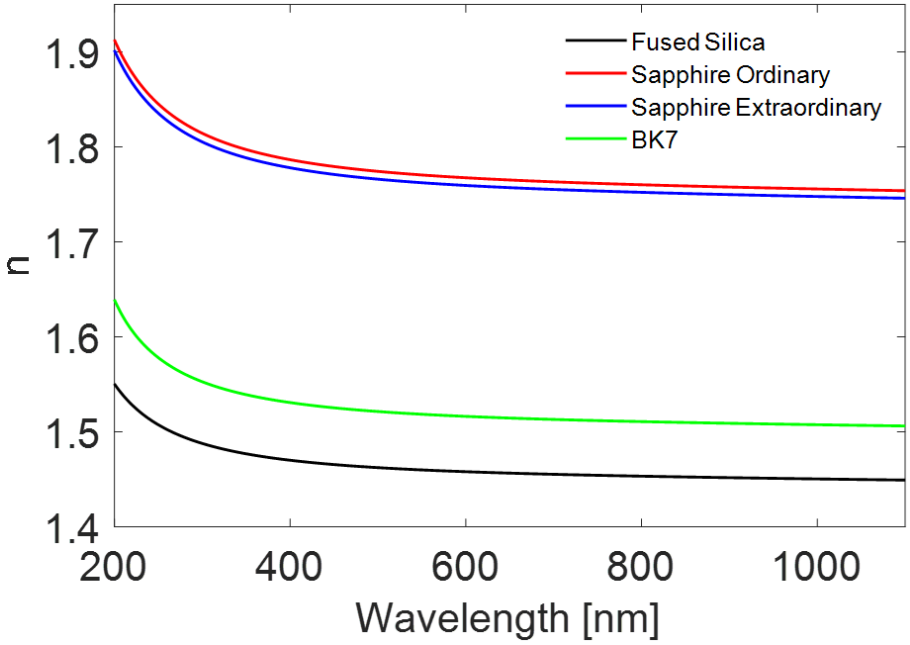

Figure 1.4: The wavelength dependent refractive index for fused silica, birefrigent sapphire, and BK7 glass, from 200 nm to 1100 nm.

Table 1.1: Sellmeier coefficients for fused silica, sapphire, and BK7 glass [19].

Material	Sellmeier Coefficient					
	B_1	B_2	B_3	C_1 [µm^2]	C_2 [µm^2]	C_3 [µm^2]
Fused Silica	0.69617	0.40794	0.89748	4.67915 $\times 10^{-3}$	1.35121 $\times 10^{-2}$	97.93400
Sapphire Ordinary	1.43135	0.65055	5.34140	5.27993 $\times 10^{-3}$	1.42383 $\times 10^{-2}$	325.01783
Sapphire Extraordinary	1.50398	0.55070	6.59274	5.48041 $\times 10^{-3}$	1.47994 $\times 10^{-2}$	402.89514
BK7	1.03961	0.23179	1.01047	6.00070 $\times 10^{-3}$	2.00179 $\times 10^{-2}$	103.56065

Refraction is described by Snell's law as

$$n_2 \sin(\theta_i) = n_1 \sin(\theta_t). \tag{1.5}$$

Here, n_1 represents the refractive index of the material the light is transiting into, n_2 the refractive index of the material the light is transiting from, θ_i the angle of incidence to the normal of the material interface, and θ_t the transmitted angle from the normal of the material interface. Material indices of refraction are carefully considered when designing optical systems. Variation of the index of refraction due to radiation effects must be considered for its potential to significantly alter the parameters of an optical system, such as the focal length of a lens in a LIBS instrument. Since the index of refraction is wavelength-dependent, refraction results in dispersion when polychromatic light is passed across the boundary of two media because different wavelengths refract at different angles. Dispersion separates the polychromatic light into a spectrum, as seen when light passes through a prism, for example. Fresnel reflection at the interface of two different materials occurs because of the different indices of refraction. In Fresnel reflection the reflected angle is equal to the incident angle ($\theta_r = \theta_i$). If a smooth optical surface of the material is assumed, then for an angle of incidence of $\theta_i = 0$, Fresnel's

formula provides the fraction of light reflected, R, as

$$R = \left(\frac{n_1 - n_2}{n_1 + n_2} \right)^2 . \tag{1.6}$$

Because of the dependence of Fresnel reflection on the refractive index, changes of the refractive index will likewise change the Fresnel reflection coefficient. Changes to the refractive index can be induced by the intensity-dependent refractive index shown in Equation 1.1, or by radiation effects that alter the refractive index [20]. Changing the refractive index also affects the intermodal dispersion [21] in optical fibers. Intermodal dispersion is the difference in the group delays of the modes within a multi-mode optical fiber [22], and mode dispersion in the fiber is determined by the wavelength-dependent refractive index which causes reflection and refraction of the light transiting the fiber. If the temporal pulse width transmitted through the fiber is comparable to or shorter than the intermodal dispersion, then the pulse width may be broadened [22]. This effect may also be enhanced or reduced due to the intensity-dependent or radiation-induced changes to refractive index, and has serious implications for fiber data networks that are data limited by intermodal dispersion [22], or in spectroscopy-based instruments such as LIBS, which transmit intense laser pulses and receive emission spectra via optical fibers that may also be exposed to radiation [5].

The primary mechanism for optical absorption at photon energies below 50 keV ($\lambda > 25$ pm) is the photoelectric effect, which leads to the microscopic origin of absorption that is the excitation of electron-hole pairs which causes electronic transitions within the material. Photoelectric absorption can occur if the bandgap is less than the energy of the incident photon. The magnitude of bandgap is the reason that optical glasses appear transparent to electromagnetic radiation in the visible spectrum. When the bandgap is smaller than the energy of incident photon, photoelectric absorption of photons produces excited electron-hole pairs. These electron hole-pairs can either decay

radiatively resulting in photon emission, or non-radiatively producing defect sites within the material [11]. The optical absorption of a medium follows the Lambert-Beer law as

$$I\left(L\right) = I_0 e^{-\alpha L}, \tag{1.7}$$

where L is the distance the light traverses in the medium, I is the light intensity transmitted through the experimental optical sample, and I_0 is the measured reference intensity of the light source without the material present.

Photon emission may be stimulated or spontaneous. Stimulated emission of photons produces photons of energy E_{photon} identical to the photon absorbed in the medium, given by

$$E_{photon} = \hbar\omega = hc/\lambda. \tag{1.8}$$

Here, h is Planck's constant, $\hbar = h/2\pi$, ω is the photon angular frequency, and λ is the photon wavelength. Light resulting from stimulated emission carries the same phase as the incident light, which is the basis of laser technology [23]. Spontaneous emission results from the decay of excited states of electrons or nuclei, with the distinction that gamma rays are the high energy photons resultant from nuclear decay. Irradiated optical materials such as sapphire, for example, can exhibit spontaneous emission from the decay of neutron-activated nuclei which, similar to absorption bands centered about a specific wavelength, exhibit emission bands likewise centered about specific wavelengths [24].

Optical scattering is the process of spontaneous emission of light following absorption. Scattering attenuates light within a medium in addition to absorption, and the aggregate effect of scattering and absorption is referred to as extinction. Attenuation due to scattering also follows an exponential law:

$$I = I_0 e^{-\tau_{scat} L}. \tag{1.9}$$

Here τ_{scat} is the scattering coefficient defined by the material scattering cross-section and packing fraction [16]. Rayleigh scattering has been found to be altered by ionizing radiation with a linear increase with radiation dose in single mode optical fibers [25].

1.3.2 Nonlinear Optical Properties

The nonlinear change of index of refraction, known as the Kerr effect, and the nonlinear change in optical absorption, as described in Equations (1.1) and (1.2), respectively, are optical effects that result from the third-order nonlinear susceptibility in the Taylor expansion of the nonlinear polarization [13, 26]:

$$P(E) = \epsilon_0 \chi^{(1)} E + \epsilon_0 \chi^{(2)} E^2 + \epsilon_0 \chi^{(3)} E^3 + ... \tag{1.10}$$

Here P is the polarization, E is the applied electric field, and $\chi^{(n)}$ is the n-th order susceptibility. Multiple physical processes can simultaneously contribute to third-order nonlinearities over a range of time scales. Multiphoton absorption, which includes TPA, is an ultrafast ($< 10^{-12}$ s) third-order nonlinearity that contributes to the nonlinear change of the refractive index and optical absorption. SA and reverse SA are slow, or cumulative third-order nonlinearities that also contribute to the total nonlinear absorption [13]. For lasers producing picosecond or shorter pulse duration, only ultrafast nonlinear effects have a significant effect on the light transmitted through a nonlinear medium because of the slower response of the cumulative nonlinearities. Conversely, in the slow regime, with pulse durations greater than 10^{-12} s, the light transmitted is susceptible to the cumulative effects of ultrafast and slow nonlinearities. Nonlinear optical coefficients are therefore defined and indexed by the applicable wavelength and pulse duration [7].

Depending on the pulse duration, the coefficients of nonlinear absorption or refraction may be better described by a cross-section rather than by single nonlinear susceptibility.

The nonlinear change in intensity within a sample reflecting the contributions of multiple absorption mechanisms σ_{ij} can be expressed by [13, 27]

$$\frac{dI}{dz'} = -\sum_{i=1,j>i}^{N} \sigma_{ij}\Delta N_{ij} I_0. \tag{1.11}$$

Here, ΔN_{ij} is the population difference between the two absorption states. This is synonymous to the weighted nuclear macroscopic cross-section.

Nonlinear refraction and nonlinear absorption are both nonlinear optical effects of interest in applications such as optical sensing [28] and ultrafast all-optical switching and logic gating [26]. The nonlinear change in refractive index may lead to phenomena such as self-focusing [29]. Nonlinear changes in absorption are important for the development of optical modulation and switching systems, particularly the changes to absorption induced by TPA and SA cumulatively represented by the nonlinear absorption coefficient β. TPA is the dominant and well-studied ultrafast third-order nonlinear susceptibility observed both in traditional optical media like fused silica and sapphire, and in semiconductors [7, 30]. The slow nonlinearity that accompanies SA is observed in semiconductors [31, 32], nanocomposites [27, 33], thin films [34], and recently in traditional optical media [35]. In the presence of both TPA and SA, their competition determines the total intensity-dependent effect of nonlinear absorption on transmitted laser power.

The effects of the nonlinear change in refractive index and absorption are linearly dependent on the applied intensity as described in Equations (1.1) and (1.2). The scale of these effects, however, is limited by the damage threshold of the material, which can be exceeded by the application of a high-intensity laser pulse or through the process of catastrophic self-focusing due to the nonlinear change in refractive index [28]. Thus the material damage threshold or plasma generation threshold are limiting factors to be considered when investigating the nonlinear optical effects.

1.3.3 Saturable Absorption

SA [14] is observed when the saturation intensity, I_S, is exceeded, resulting in the *Pauli blocking* effect: the material's available higher electronic energy states are filled due to photoelectric absorption and excitation of valence electron-carriers to the conduction band, and further photon absorption is constrained, which can ultimately result in a reduction of the material's absorption coefficient [36]. The SA coefficient, α_{SA}, is defined as [27, 34, 37]

$$\alpha_{SA} = \frac{\alpha_0}{1 + I_0/I_S}, \tag{1.12}$$

where I_S is the saturation intensity.

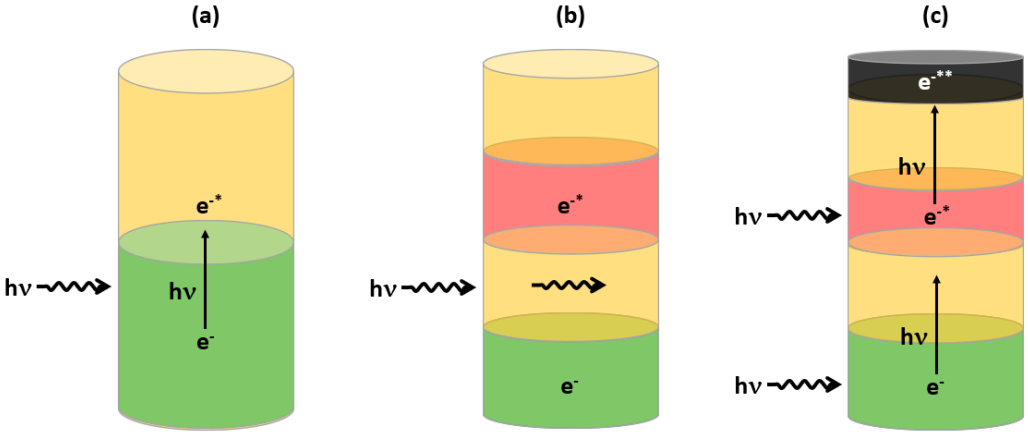

Figure 1.5: The processes of saturable absorption and reverse saturable absorption. (a) A photon of energy $h\nu$ is photoelectrically absorbed by an electron in the valence band, exciting it to the conduction band. (b) At intensity I_S a large number of electrons enter the conduction band, such that it is saturated and the absorption is reduced. (c) In reverse saturable absorption the excited electrons absorb photons again and transition to a second excited state.

SA, also called absorption saturation, is a phenomenon attributable to electron excited state filling [38]. This is a electron-carrier density-dependent band-filling process that may occur by trapping electrons into shallow traps that act as a sink for conduction band electrons. These sinks may be created by radiation damage within the material and explain why this phenomenon is observed following irradiation [35]. SA is a time-

dependent process in which a competition takes place between the rate of electron-carrier generation via the photoelectric effect and the relaxation of trapped carriers back to the valence band via radiative (spontaneous photon emission) or non-radiative (phonon relaxation) processes [38]. SA occurs when the trapped electron-carrier relaxation time is long enough compared to the pulse duration that a sufficient amount of excited and trapped valence electrons prevents additional absorption of light due to filled electron excited states, resulting in the *Pauli blocking* effect [39]. Conversely, reverse saturable absorption occurs when the excited state electrons in the valence band further absorb additional photons and excite to higher states [40]. These processes are illustrated in Figure 1.5.

1.4 Radiation Interactions and Effects in Optical Materials

Ionizing radiation, such as high-energy gamma rays and neutrons produced by nuclear decay, alter material properties through a variety of interactions. Gamma radiation may excite electrons to the conduction band through the process of Compton scattering to generate electron-hole pairs. When the electron-hole pairs recombine non-radiatively, they may displace lattice atoms through the generation of phonons [11]. Electromagnetic gamma radiation can also generate electron-hole pairs that combine with existing precursor oxygen deficient center (ODC) and to form an oxygen vacancy with a trapped hole, referred to as E' sites or centers [41]. Neutrons displace lattice atoms and break chemical bonds through direct atomic displacement, known as knock-on collisions, resulting in various types of atomic deficiency sites, and in the presence of gamma radiation these radiation induced deficiency sites may also be transformed into E' sites [1]. Atomic deficiency and E' sites absorb light at various wavelengths based on the type of chemical

bond they are associated with. The absorption resultant from radiation effects which is cumulative with linear absorption already present in the material is RIA [11]. RIA is a time- and wavelength-dependent phenomenon, differentiated by the defect type which determines the wavelength of absorption and the defect decay or annealing rate [42]. Annealing of material defects is accomplished through multiple means, such as electron-hole recombination, interstitial migration, and repair of defect sites, which can be accelerated through the addition of energy through heating [42, 43]. An example of neutron

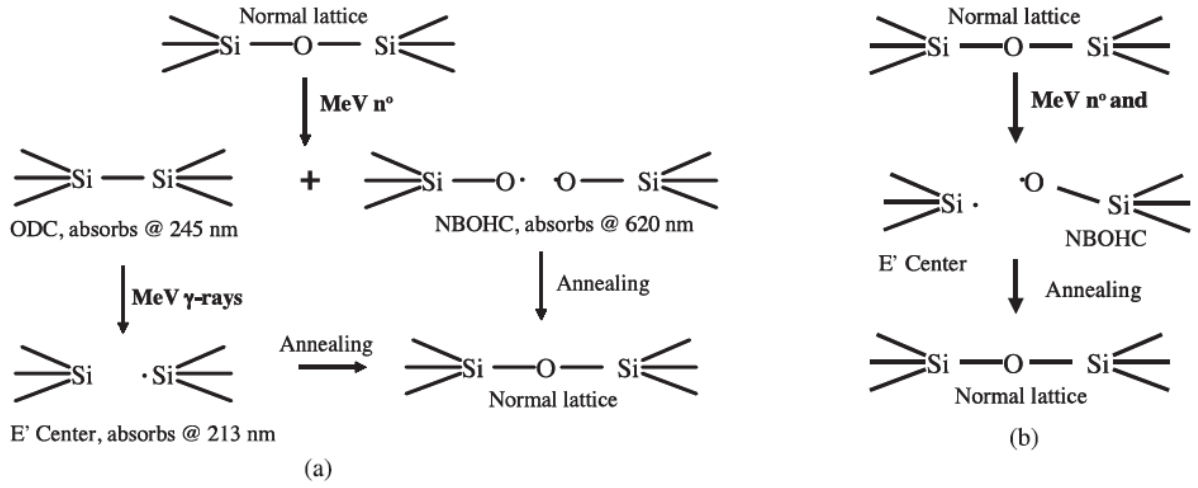

Figure 1.6: Examples of gamma- and neutron-induced defects in fused silica. (a) Generation of ODC and NBOHC by neutron interaction with subsequent E' center generation by gamma interaction. (b) E' center and NBOHC generation from neutron interaction with subsequent repair by thermal annealing [1].

generation of ODC, nonbridging oxygen-hole center (NBOHC) with E' centers, gamma-generated E' centers, and annealing processes is shown in Figure 1.6 [1]. Here, the defects generated in fused silica, which is composed of amorphous SiO_2, are each labelled with the corresponding wavelength of RIA.

The case of fused silica is a useful illustration of the multiple factors that effect defect generation and annealing in an irradiated material. For example, E' center concentrations, which absorb light at 213 nm in fused silica, are dependent on the pre-existence of

precursor defects in a material, the generation of defects from interactions with ionizing radiation, the gamma flux which generates E' centers from ODC, and the annealing of defects through natural decay or the addition of energy through the application of heat. In Figure 1.6(a) ODC and NBOHC are shown to be generated through the knock-on interactions with fast neutrons. ODC may also be present in low-OH content fused silica without neutron irradiation as a precursor from the manufacturing process. In either case the ODC as a precursor or generated by neutron interaction may be transformed by gamma radiation into an E' center [44]. The generation of E' centers in irradiated fused silica is then simultaneously dependent on the presence of precursor ODC and how readily additional ODC are created by neutron interactions, in addition to the gamma flux which ultimately creates the E' centers. As can also be seen in Figure 1.6(a), the E' centers anneal to Si-O-Si bonds that constitute fused silica, which reduces the amount of E' centers and is a fourth component affecting the concentration of E' centers in irradiated fused silica.

The compositions of fused silica glass and borosilicate glasses will have variations based on the manufacturing methods or by design for specific purposes. For example there are four different types of fused silica glasses that will vary in purity and OH content depending on their manufacturing process. High purity fused silica glasses tend to have low metallic impurities that allow good UV transmissions, and high-OH content that limits IR transmission [8]. Impure fused silica glass will have trace metallic elements, with Al being the most prominent, but lower-OH content. The variations of OH content and purity will affect radiation damage within different types of fused silica such as the example previously discussed of low-OH content fused silica that enhances radiation damage due to the presence of ODC precursors and Al metallic impurities [45]. Likewise, the lack of OH content may hinder thermal annealing processes because of the lack of mobile hydroxyls [42].

Borosilicate crown glass, primarily composed of SiO_2 with B_2O_3 added as a glass network former, is a hard glass that is desirable for its durability and ease of handling [46]. Borosilicate glasses are similarly susceptible to the radiation damage described for fused silica because of the SiO_2 content. Schott NBK7 is a type of borosilicate crown glass that is free of lead and arsenic, and Schott BK7G18 has been doped with cerium to make the crown glass radiation-resistant by destabilizing radiation induced point defects within the glass and facilitating annealing [47]. BK7G18 is a popular radiation-resistant glass that has found wide use in space applications, but recently when studied under true *in-situ* irradiation and spectroscopic examination was found to have higher RIA than the undoped BK7 glass while exposed to irradiation [47]. It was found that studying BK7G18 even 1 hour after irradiation would provide a misleading underestimation of the RIA, which highlights the importance of *in-situ* studies of optical materials under conditions of irradiation and thermal annealing to support the development of optical instruments and systems for intense radioactive applications.

Sapphire, which is composed of crystalline Al_2O_3, will generate various types of aluminium-oxygen vacancy and paired vacancy centers, known as F and F_2 centers respectively, via direct collisions with energetic particles when exposed to neutron radiation [24, 48]. F centers can be further altered to form different ionization states through the absorption of electrons and holes when exposed to gamma irradiation [9]. The ionization states include F^+, a single oxygen-vacancy center occupied with one electron, and paired vacancy centers F_2^+, and F_2^{2+} that are occupied by three and two electrons, respectively [24]. Figure 1.7 shows the relative energy band position of F center defects in sapphire and how these defects transform into other defect types through the exchange of electrons under the effect of photobleaching. This exchange can be induced by exposure to gamma irradiation as well as thermal annealing and excitation of electrons to the conduction band.

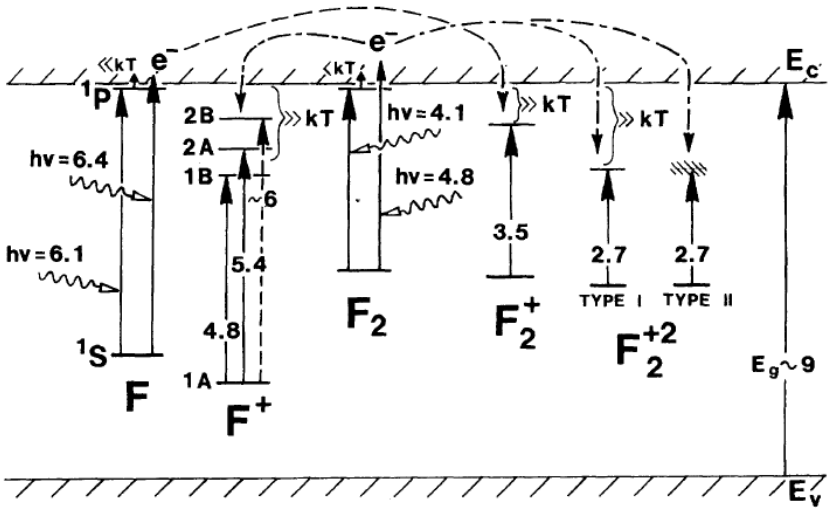

Figure 1.7: The relative energy positions with respect to band edges of paired oxygen vacancies in sapphire [24].

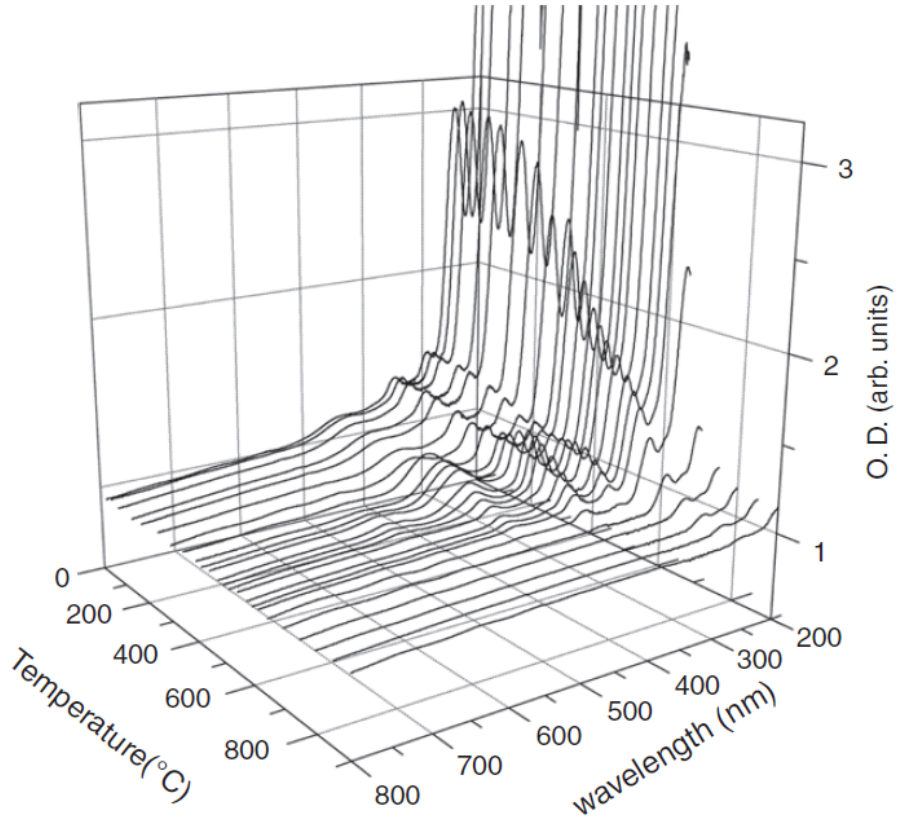

Figure 1.8: Post-irradiation thermally annealed RIA spectrum in neutron irradiated sapphire [49].

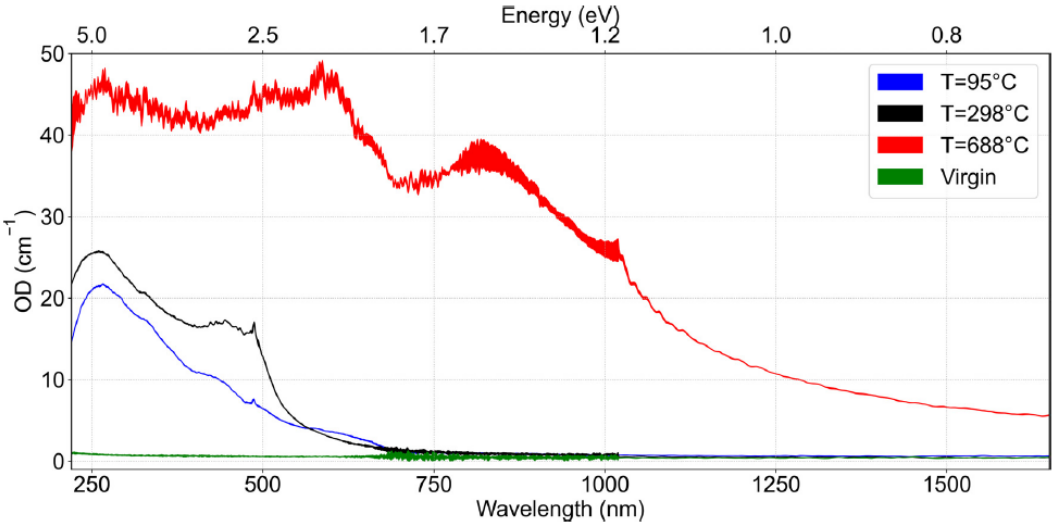

Figure 1.9: Concurrent-irradiation thermally annealed RIA spectrum in neutron irradiated sapphire [50].

Thermal annealing in the context of this research is the process of restoring radiation induced changes, or damage, in the optical material's chemical structure to the unirradiated state. It is the basis of the thermoluminescence dosimetry process which measures the radiation dose deposited in a material based on the emission spectrum of the thermally annealed irradiated material [51]. Corundum α-Al_2O_3 thermoluminescence detectors, the same chemical composition as sapphire, are an example of this process that develop F and ionized F centers when irradiated, as previously discussed. When thermally annealed, these centers emit a characteristic optical spectrum due to the absorption of electrons and holes liberated from deep traps under thermal excitation [51]. In this example the thermally annealed corundum emits a 420-nm photon after converting an F^+ center to an F center by the absorption of an electron, and emits a 330-nm photon after conversion of an F center to an F^+ center by absorption of a hole. Annealing of Al_2O_3 F center defects also occurs under thermal excitation. F and F^+ centers coalesce into F center clusters F_2, F_2^+, and F_2^{2+} between temperatures of 350 °C and 500 °C, due to increase mobility in the lattice structure, and these F clusters repair the broken bonds

above 650 °C [49].

Fused silica SiO_2 develops radiation damage in the form of ODC, E' centers, NBOHC, Al E' centers in low-OH high-impurity content fused silica [1, 42]. The application of heat during thermal annealing can repair E' centers and NBOHC by allowing recombination of the broken Si-O bonds, and this process can be enhanced in high-OH high purity content fused silica due to increased mobility of hydroxyls [42]. Likewise in low-OH content fused silica this annealing process is hindered due to the lack of OH, and the precursor E' and ODC introduced in the manufacturing process are considered thermally stable. The mechanism for neutron induced ODC annealing can be conversion to an E' center by gamma irradiation followed by recombination with a NBOHC [1]. The gamma radiation induced Al E' centers are annealed by the excitation of electrons from traps during thermal annealing [43].

The thermal annealing effects of RIA in optical materials is illustrated by the example of sapphire in Figures 1.8 and 1.9. In Figure 1.8 optical grade sapphire is irradiated in a nuclear reactor with a neutron and gamma mixed flux and then thermally annealed post-irradiation. Here the sapphire is irradiated to a neutron fluence of 9.1×10^{17} n $\cdot$ cm^{-2} (fast neutrons) and the RIA is measured at room temperature and after annealing up to 900 °C. The RIA spectrum is shown to decrease consistently after heating for each post-irradiation thermal annealing step up to 900 °C. Figure 1.9 shows the case of concurrent-irradiation thermal annealing of sapphire irradiated to a fluence of 2.4×10^{21} n $\cdot$ cm^{-2} (fast neutrons) while being concurrently thermally annealed at three temperatures shown in the legend [50]. Under the conditions of concurrent-irradiation thermal annealing sapphire shows that applying heat to the irradiated sapphire increase the RIA with increasing temperature. Similar to the discussion of BK7G18 crown glass, this illustration also emphasises the importance of *in-situ* measurements of optical materials to determine the performance of the materials under the condition of concurrent-irradiation thermal

annealing.

Information on the *in-situ* performance of optical materials under simultaneous effects of ionizing radiation and thermal annealing is essential to determine the suitability of optical materials to serve as sensitive optics exposed to continuous ionizing radiation. This exposure may be for multiple days to generate sufficient thrust in the case of Vehicle for Interplanetary Space Transportation Application (VISTA) [4], or years for power generation in the case of ICF [1] or instrumentation of advanced fission reactors [2]. The optics may not remain serviceable for the duration of these time frames, but the knowledge of their performance will at least inform how frequently they must be replaced, and how instruments such as lasers and spectrometers must compensate for the radiation and thermally induced changes to the material linear and nonlinear optical properties.

1.5 Optical Material Characterization and Evaluation

The performance and selection of optical materials are influenced by many factors that include the optical properties among others such as mechanical qualities and economic efficiency to produce. The optical properties, linear and nonlinear, can be evaluated by spectroscopy and Z-scan, respectively. Here the basic concepts, capabilities, and limitations of both techniques are discussed.

1.5.1 Spectroscopy

Spectroscopy is the study of the interaction between matter and electromagnetic radiation, and a means by which the linear absorption of light by materials may be measured. Spectroscopic measurements of attenuation typically require a reference light source to transmit through a material sample, a spectrometer with diffraction grating to separate

the light by wavelength and intensity and resolve the measurement into an observable spectrum, and coupling hardware to interface the light source with the material to be measured and the detector. Coupling hardware may include fiber-optic cables to transmit light from the source through the sample and collect the light after the sample to transmit to the spectrometer. Mounting hardware to interface the material sample with the light source and spectrometer fiber-optic cables, and to isolate background light from the measurement, may also be required. Spectroscopy measurements may be configured to measure the linear attenuation in the material, the reflection losses from the surfaces of the materials, or a combination of both. In instances where the measurement is only configured to measure the linear attenuation, the reflection loses may be accounted for by data of the optical samples provided by the manufacturer, by calculating the Fresnel reflection losses from the Sellmeier equation and Snell's law, or by comparison of a known reference sample to an experimental sample both measured by the same spectroscopy system.

Linear absorption measurements in literature are commonly quantified and represented by OD in [cm^{-1}] which is defined as [16, 52]

$$OD = \frac{1}{L} \log_{10} \left(I_0 / I \right) . \tag{1.13}$$

Here, L is the optical sample width, I_0 is the measured reference intensity of the incident light, and I is the light intensity transmitted through the experimental optical sample. The reference intensity may be measured without an optical sample present, or it may be measured with a reference optical sample present for comparison to the spectrum measured with the experimental optical sample. The latter method is useful to account for reflection losses when reflection is not measured. Optical density, or absorbance A, represents the cumulative effects of scattering, absorption, and depending on the spectroscopy setup the reflectance as well. The absorption coefficient represents only

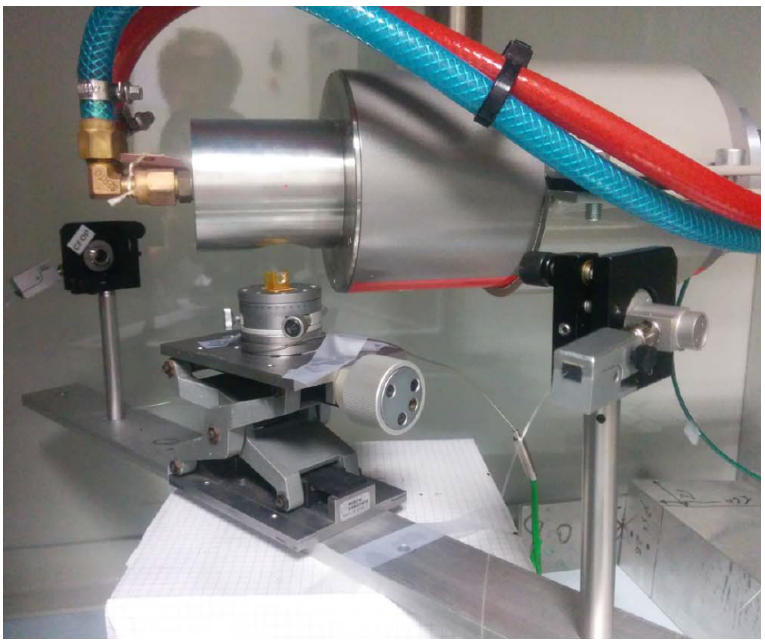

Figure 1.10: Example *in-situ* spectroscopy measurement of RIA in borosilicate glass [47]. The glass sample is situated between two collimating lenses for transmitting and receiving the reference light source through the sample and to the spectrometer.

absorption in a material from the photoelectric effect generation of electron-hole pairs and does not account for scattering or reflection losses. The absorption coefficient is related to the OD, in the absence of reflection losses, by [53]

$$OD = \frac{\alpha L}{\ln 10} \tag{1.14}$$

The use of OD is useful for many experimental applications where the attenuation is determined without differentiating between losses due to absorption and scattering, such as *in-situ* radiation-induced attenuation spectroscopy experiments like that shown in Figure 1.10.

1.5.2 The Z-Scan Technique

The Z-scan technique, originally developed by M. Sheik-Bahae and E. W. Van Stryland, is a simple technique to measure the nonlinear refractive index and nonlinear absorption of optical glasses, semiconductors, nanocomposites, and other media [12]. A single laser beam is used, and measurements are made of the laser power incident on, and transmitted through, the optical material sample as it is translated on the laser propagation axis, z (hence the name Z-scan), through the intense focus of the laser, as depicted in Figure 1.11. In this example an optical sample is translated through the intense focus of the pulsed laser beam. At each increment of the position, the reference laser pulse power P_0, corresponding to the power incident on the sample, and the transmitted laser pulse power P_T, after transiting through the sample, are measured. The ratio of the transmitted pulse power and reference pulse power, measured for multiple positions as the sample is translated through the focus, represents the NLR and NLA of the sample. The use of an aperture to restrict the transmitted pulse power at the sensor after the sample, as depicted in Figure 1.11(a), allows the measurement of the NLR of the sample. The Z-scan without an aperture on the detector, as depicted in Figure 1.11(b), measures the NLA and is referred to as an open-aperture (OA) Z-scan, while the Z-scan when an aperture is used is referred to as an closed-aperture (CA) Z-scan [13]. It is important to note that the OA aperture Z-scan without an aperture present is a measurement of the power lost as the light transits the sample, whereas the the CA Z-scan is a geometrically dependent measurement of the change of the beam profile incident on the aperture induced by the change in focal position due to optical self-focusing or defocusing. The CA Z-scan is therefore dependent on the beam profile incident upon the aperture as well as the absorption that occurs within the sample [13]. A limitation of the Z-scan method is that, in general, it is not able to determine the underlying physical processes resulting in nonlinear effects because the Z-scan is sensitive to all nonlinearities, especially in the

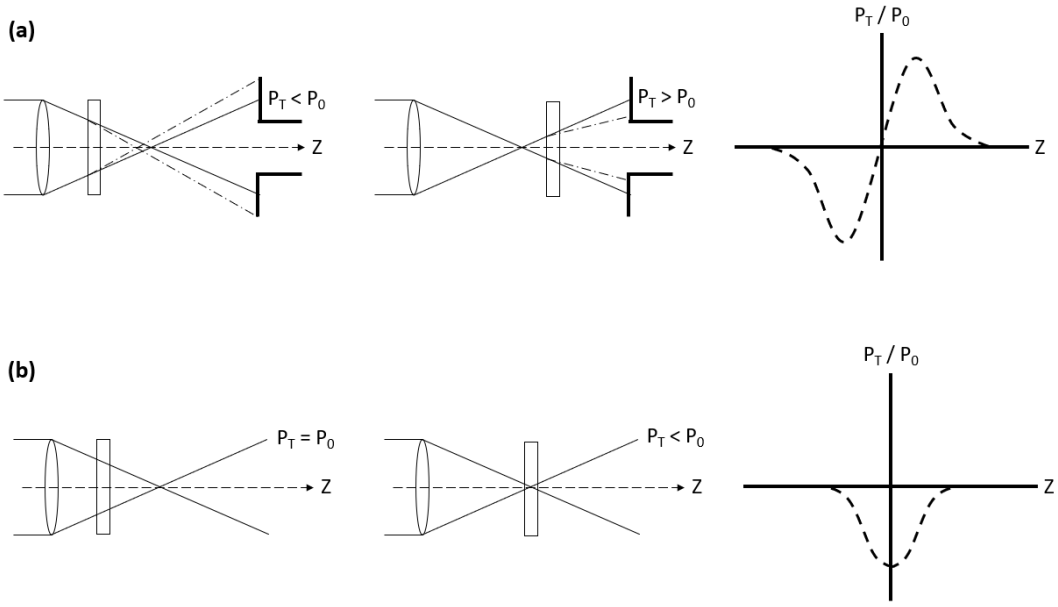

Figure 1.11: (a) Closed-aperture Z-scan measurement principle for a sample with positive nonlinearity translated through the laser beam focus. Based on Ref. [54]. As the sample is translated through the focus, the nonlinear refractive index changes the focal position and alters the size of the beam incident on the aperture, thus changing the transmitted power P_T. (b) In the open-aperture case the maximum NLA occurs when the laser pulse reaches maximum intensity within the sample, resulting in the drop in the Z-scan curve below unity for a positive nonlinearity.

"slow" regime, for pulse durations $\gtrsim 10^{-12}$ s [13]. Ultrafast picosecond and femtosecond lasers are often used in Z-scan measurements to resolve ultrafast from slow nonlinear mechanisms. A nanosecond laser was selected for this research for two reasons: nanosecond lasers are more reliable for sustained operation and more compact than their ultrafast counterparts, which is desirable for remote operation of the PIE outside of a dedicated optics laboratory, and because nanosecond lasers that emit 532 nm or 1064 nm light are common in LIBS applications, which this research supports [5].

Accurate nonlinearity measurement using the Z-scan technique relies upon an thorough characterization of the laser pulse spatial and temporal profile, a nearly-Gaussian spatial profile, and proper simulation of the Z-scan based upon the optical sample dimensions relative to the laser Rayleigh length at focus [12, 55]. Figure 1.12 shows the

Z-scan design that was developed for this research [56]. This design contains all of the

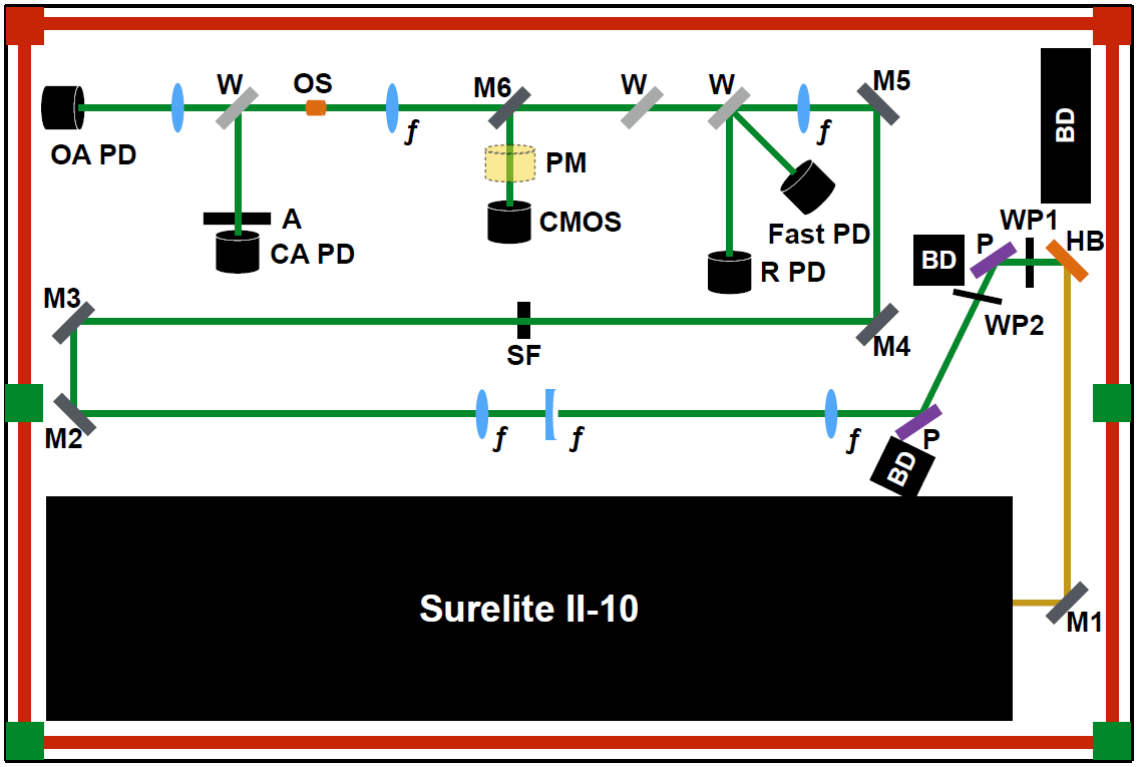

Figure 1.12: Schematic of Z-scan apparatus for acquiring CA and OA Z-scan signals [56]. This design includes power modulation and profile conditioning modules, laser spatial and temporal profile characterization sensors, and signal sensors for capturing the OA and CA Z-scan signals. The listed components are: mirror (M), harmonic beamsplitter (HB), beam dump (BD), half-wave plates (WP), polarizers (P), lenses (f), spatial filter (SF), aperture (A), wedge (W), photodiode (PD), power meter (PM), CMOS camera, and the optical sample (OS).

necessary elements to construct a functioning Z-scan experiment with the components to characterize the laser spatial and temporal profile and condition the beam to obtain a nearly-Gaussian spatial profile. Immediately after the nanosecond pulsed Nd:YAG laser is a harmonic beamsplitter and beam dump to separate the 532-nm light for Z-scan, followed by two polarizer and half-wave plate combinations used to modulate the power of the transmitted laser. 532 nm light was selected for the Z-scan because it produces a longer Rayleigh length than 1064 nm light, according to Equation 2.3, which allows the Z-scan design to obtain a higher intensity at focus while retaining a suitable Rayleigh

length to ensure the Z-scan signal is discernible. It is important to obtain the intense focus because much of the laser power will be lost in spatial filtering, which is discussed further in Chapter 2. The loss of power can be compensated for by reducing the diameter at focus, at the cost of Rayleigh length and therefore the length on the z-axis over which the Z-scan characteristic curve evolves, shown in Figure 1.11. The 532-nm light has twice the Rayleigh length of the 1064-nm light and this advantage along with the use of thick samples allows the laser to be focused to a small size while ensuring the Z-scan curve evolves over a large enough z-axis range to be detectable. The polarizer and half-wave plate combinations are used to achieve the desired intensity at focus near the damage threshold of the sample. Maximizing the laser intensity near the material damage threshold provides the greatest amplitude of the Z-scan trace, which is useful for observing small nonlinearities. The power modulation elements are also important to protect the optics in the system from damage due to the high intensities involved in the Z-scan, and for this purpose two sets of half-wave-plate and polarizer combinations are installed to ensure damage thresholds are not exceeded. The beam is next spatially filtered by gradually focusing the beam through a spatial filter to obtain an nearly TEM_{00} Gaussian spatial mode of the laser. This is accomplished by reducing the beam diameter through a Galilean telescope and then using a focusing lens to focus the beam into a spatial filter. Next the spatially filtered beam is collimated by a lens before a series of wedges is used to reflect a fraction of the laser to the reference photodiode to measure the laser pulse power prior to transiting the optical sample under examination. Here also is a fast photodiode for measuring the laser pulse temporal profile. Two identical wedges are used to reflect a portion of the beam and also to nullify aberrations in the beam profile and steer the beam onto the correct path for the Z-scan experiment. A removable mirror diverts the beam into a power meter which is used with the half-wave-plates and polarizers to tune the laser power appropriately for the sample. Behind the removable power meter is a camera

to obtain the laser spatial profile and for diagnostics and alignment of the spatial filter. A focusing lens then focuses the laser and here is where the optical sample is translated through the focus to perform the Z-scan. After the optical sample is a third wedge which splits the beam into the OA and CA signal photodiodes. The photodiodes, camera, and power meter are connected to an oscilloscope and computer which forms the DAQ and automation suite to perform the Z-scan experiment by translating the sample through focus and recording the synchronized photodiode signals.

A Gaussian laser spatial profile is ideal to both achieve a high-amplitude Z-scan signal and to accurately interpret the nonlinear coefficient values through modeling of the Z-scan experiment [15]. The Z-scan is modeled by solving Maxwell's equations assuming a Gaussian beam profile, the slow varying envelope approximation, and for 'thin samples', where $L \ll z_R$ and z_R, assuming that the laser spatial profile does not change within the thin sample from diffraction or nonlinear refraction [12, 13]. If the laser is non-Gaussian then not only is the Gaussian assumption in the solution of Maxwell's equations not valid, but it may be entirely impossible to obtain a Z-scan signal due to the inability to achieve sufficient intensity within the sample to induce a signal from nonlinear effects. One solution to perform Z-scan with non-Gaussian beams has been shown in Figure 1.12, which is to condition the beam through a spatial filter to obtain the TEM_{00} spatial mode, at the cost of a significant portion of the laser power. Another solution is to use a reference optical sample of known nonlinearity with the same width L as the experimental sample. Z-scans are then performed with the energy modulated to obtain Z-scan curves of equivalent magnitude for both the reference and experimental samples to determine the experimental sample's nonlinearity [13]. The equations to simulate Z-scan and determine the nonlinear coefficients in the thin sample regime are provided below, where δT_{pv} is the difference between the maximum and minimum magnitude of the closed aperture Z-scan curve, S the transmittance through the closed aperture, $\Delta\Phi_0$ the accumulated

phase shift, L_{eff} is the effective sample width, $\Delta T(z)$ is the open aperture Z-scan trace, Z is the sample position, and Z_0 is the Rayleigh length at focus.

$$\Delta T_{pv} \cong 0.406\,(1-S)^{0.27}\,|\Delta\Phi_0|\,, \tag{1.15}$$

$$\Delta\Phi_0 = \frac{2\pi}{\lambda} n_2 I_0 L_{eff}, \tag{1.16}$$

$$L_{eff} = \frac{1-e^{-\alpha L}}{\alpha}, \tag{1.17}$$

$$\Delta T\,(z) \approx -\frac{\beta I_0 L_{eff}}{2\sqrt{2}} \frac{1}{[1+Z^2/Z_0^2]}, \tag{1.18}$$

Conversely, the "thick sample" regime of Z-scan, where $L \gg z_R$ is considered more complex to model because in a thick sample the laser beam diameter and focal position will change significantly enough from diffraction or nonlinear refraction that these changes can not be neglected [55]. A method for modeling thick-sample Z-scan is discussed in Chapter 2. Examples of CA and OA Z-scan fitting curves in the thick sample regime are provided in Figure 1.13 [35]. The thick sample method, however, has a greater sensitivity

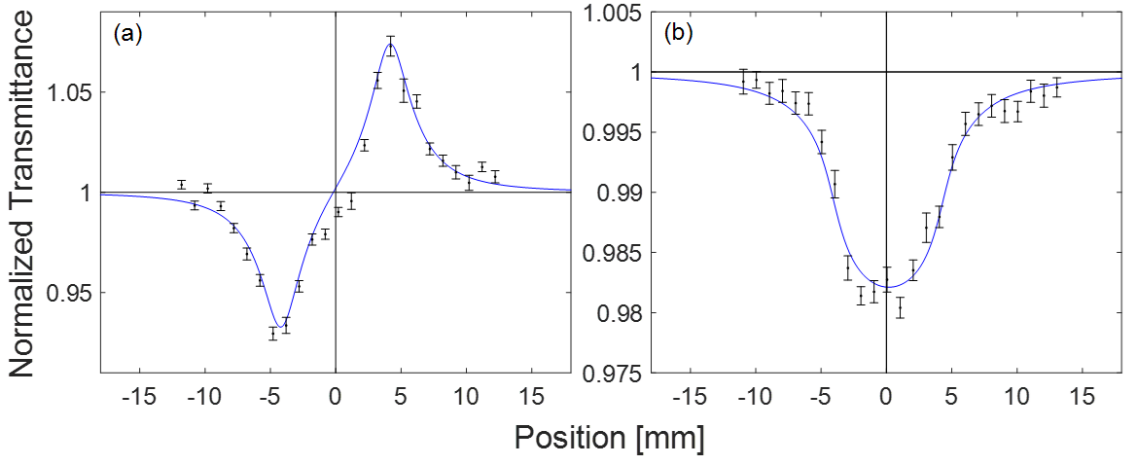

Figure 1.13: Example Z-scan traces with simulated fit curves in blue for the (a) CA n_2 measurement and the (b) OA β measurement.

to nonlinearities as can be seen in the case of NLR and the B-integral, where an increased sample width is accompanied by an increase in accumulated on-axis nonlinear phase

shift [28]:

$$B = \frac{2\pi}{\lambda} \int n_2 I\left(z\right) dz. \tag{1.19}$$

Here, B represents the accumulated on-axis phase shift, λ is the laser wavelength, and $I(z)$ is the optical intensity along the beam axis z. As the sample width L is increased along the laser propagation axis z, the accumulated phase shift as the pulse traverses the sample is increased, resulting in greater nonlinear effect and an enhanced Z-scan signal. The first-order theory of Hermann and McDuff [55, 57] is an analytic solution of the beam propagation equation that accurately simulates Z-scan for thick samples, and will be discussed later in Chapter 2.

1.6 Dissertation Structure

The following chapters summarize the development of the experimental apparatus for this research, the test plan structure for irradiation and evaluation of samples, and the contributions of this work to the understanding of radiation effects in optical materials. This work provides information on the nearly *in-situ* performance of bulk optical materials to determine their suitability for high-intensity laser applications in extreme radioactive and thermal environments. This is accomplished by examining the RIA, and the radiation-induced changes to NLA and NLR under the conditions of post-irradiation and concurrent-irradiation thermal annealing. Chapter 2 describes the development of the PIE setup with Z-scan and spectroscopy experiments, and Chapter 3 summarizes the irradiation and thermal annealing schedule for optical material samples. Chapter 4 summarizes the original contributions of this research in understanding linear RIA and the competing effect of thermal annealing, and Chapter 5 summarizes the contributions to understanding radiation-induced changes to NLR and NLA.

Chapter 2

Post-Irradiation Examination System Development

The PIE system is a compact and self-contained optical material evaluation suite consisting of a Z-scan laser experiment and a linear attenuation spectroscopy experiment with DAQ oscilloscope and computer. It is compact so that it can be located at the site of sample irradiation for expedient evaluation of samples without the robust support of a fully equipped optical laboratory. It is self-contained inside of its own class IV laser barrier so that it can easily meet the laser safety requirements of any standard facility.

The PIE system was initially developed and validated at the University of Michigan (UM) in the Applied Nuclear Science Instrumentation Laboratory (ANSIL). To accommodate this, an optical laboratory was established in ANSIL which helped to develop the safety validation procedures for the PIE Z-scan experiment. Optical samples to validate the PIE were shipped to the OSU NRL for irradiation to 500 krad gamma in the ^{60}Co irradiator pool dry tube.

2.1 Spectroscopy

The linear absorption setup is designed to measure the transmission of optical windows and fibers over the wavelength range of 200–1100 µm. The setup employs an Ocean Insight HR4000 CG-UV-NIR spectrometer and a DH-2000-BAL deuterium/halogen light source. The 600-µm diameter solarized optical fiber pigtails couple the light source to the sample and then to the spectrometer. The data are collected with OceanView software and analyzed in MATLAB. The setup is shown in Figure 2.1 configured to analyze window samples in the stand with collimating lenses coupled to the pigtails.

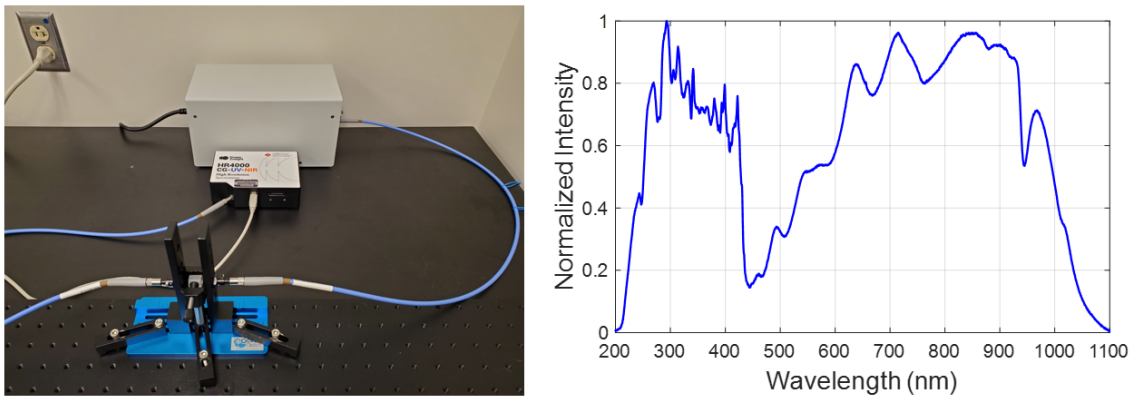

Figure 2.1: Left: the tabletop spectroscopy setup with Ocean Insight DH-2000-BAL light source, HR4000-CG-UV-NIR spectrometer, and optical sample mounted in the stand. Right: reference spectrum of the DH-2000-BAL light source.

The transmission spectrum of every optical sample was measured prior to irradiation to provide a reference spectrum for comparison to the sample's irradiated spectrum. Sample transmission spectra were also recorded immediately after irradiation, after each thermal annealing step, and after irradiation with concurrent-irradiation thermal annealing. The comparison of the sample reference spectrum to the irradiated and thermally annealed transmission spectra allows the identification of RIA in the sample and evaluation of the effects of thermal annealing in restoring the sample's properties prior to irradiation. Before each transmission measurement the background was subtracted, and

a reference measurement of the light source, I_0, was taken to account for light source drift over time. The measured stability of the DH-2000-BAL as a function of time was 0.01% h^{-1} at 254 nm and 700 nm. A reference measurement was therefore taken for every transmission measurement to minimize the impact of the light source intensity drift over time on the results. The raw spectral data were then combined and analyzed in MATLAB to determine the optical density using Equation (1.13) and examine changes that can be attributed to irradiation and annealing.

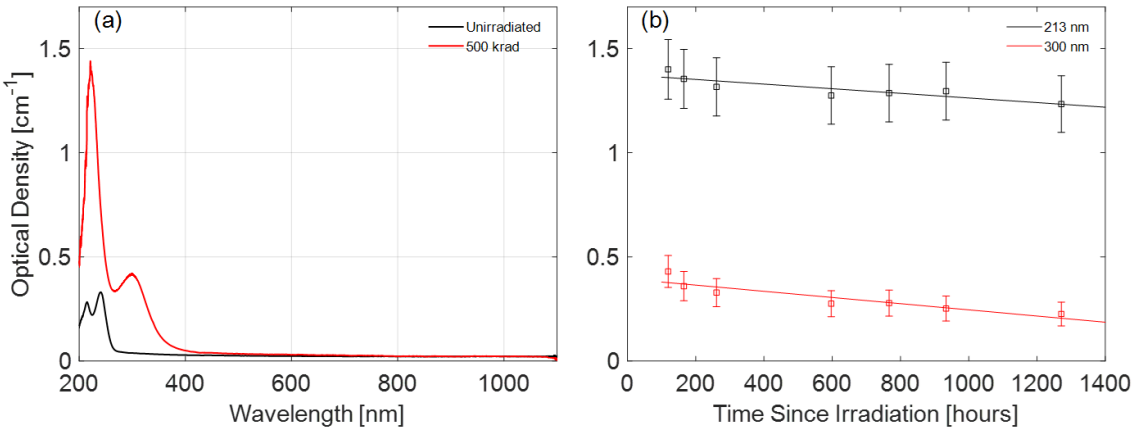

Figure 2.2: (a) Unirradiated and 500-krad gamma-irradiated OD measured for I302 used in validation of the PIE system. (b) Measured decay of attenuation peaks observed in 500 krad gamma irradiated I302 for 213 nm and 300 nm, with an exponential decay fit.

The spectroscopy experiment was validated with 500-krad gamma-irradiated optical samples of Heraeus S2000 high-OH content fused silica, Heraeus I302 low-OH content fused silica, and optical grade sapphire. The samples were shipped to the OSU NRL for irradiation and then returned to the UM ANSIL for evaluation by the PIE. I302 is the only material sample that exhibited significant RIA at 500 krad. The OD measurement with exponential fit to the decay of the RIA is presented in Figure 2.2. The 500-krad OD measurement was performed 119 hours (∼5 days) after irradiation, with subsequent measurements occurring up to 52 days later. The observation of irradiated I302 demonstrates the importance of rapid PIE following irradation and the ability of the spectroscopy ex-

periment to capture the changes in attenuation following irradiation. A comparison of the 500 krad irradiated I302 RIA measurement to a similar example from literature of a comparable low-OH content synthetic fused silica, Heraeus Infrasil 301, is provided in Figure 2.3 [58]. Here the RIA spectrum for both samples exhibits the known attenuation

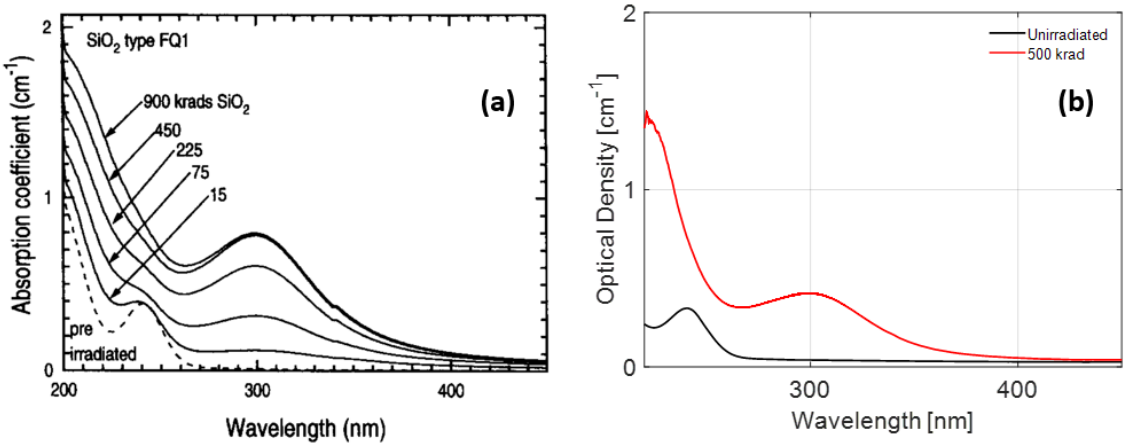

Figure 2.3: (a) RIA spectrum for gamma-irradiated Heraeus Infrasil 301 low-OH content fused silica with doses listed from Ref. [58]. (b) RIA spectrum for 500 krad gamma irradiated I302 as measured by the PIE system.

peak at 300 nm, and the continuous rise in attenuation in the UV as the wavelength decreases down to 213 nm, which are discussed further in Chapter 4.

2.2 Z-Scan

The Z-scan experiment was designed based on the concepts, principles, and previous works described in Section 1.5.2 [56]. The initial proof of concept of the Z-scan experiment was performed in the Lambda Cubed laboratory of the Gérard Mourou Center for Ultrafast Optical Science at UM prior to moving the experiment into its compact and self-contained configuration for validation in ANSIL. The PIE Z-scan experiment was performed at 532 nm with a nanosecond pulsed Nd:YAG laser. The 532 nm wavelength was selected because it is a common wavelength for LIBS, in addition to 1064 nm [2, 5, 6].

Likewise, the nanosecond pulse duration is common for more compact and reliable lasers employed in most LIBS applications. Figures 2.4 and 2.5 show the schematic design of the Z-scan concept and the initial Z-scan experiment on a laboratory optics table, respectively.

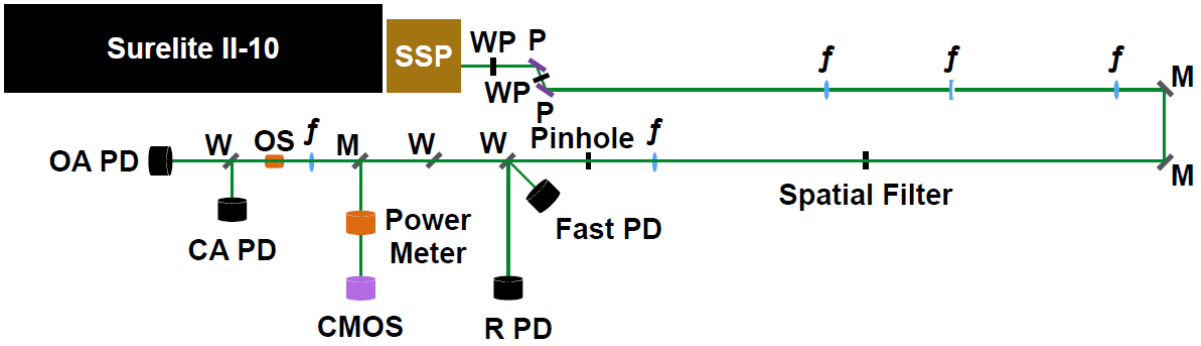

Figure 2.4: Conceptual design for the Z-scan proof of concept prior to integration into the PIE setup. The second-harmonic 532-nm and 1064-nm ns laser pulses from the the Surelite II-10 laser enter the Surelite Separation Package (SSP), which separates the two wavelengths into separate laser paths through a combination of harmonic beamsplitters and mirrors. The 1064-nm pulse is dumped, while the 532-nm pulse continues through two half-wave-plate (WP) and polarizer (P) combinations for continuous power adjustment. A combination of lenses (f) reduces the beam diameter from 6 mm to 1 mm before the spatial filter, which produces a Gaussian laser profile. The pulse is then collimated by a lens before passing through a pinhole to trim the diffraction rings. Two wedges (W) reflect portions of the pulse into the reference photodiode (R PD) and fast photodiode (Fast PD), then a removable mirror (M) reflects the beam into a power meter and camera for laser profile diagnostics. a final lens focuses the pulse into the optical sample (OS), and a wedge splits the pulse into the CA (CA PD) and OA (OA PD) photodiodes.

The Z-scan experiment is built around Amplitude Surelite II-10 nanosecond pulsed laser, as seen in Fgiure 2.5(a), which stimulates the nonlinear effects within the optical materials, and provides the signal to measure the nonlinear effects. The Surelite II-10 output is a 6-mm diameter, 1064-nm pulse, with 532-nm pulses produced by a second-harmonic generator within the laser head. The combined 532/1064 nm output beam is passed through a combination of harmonic beamsplitters in a surelite separation package to obtain only the 532 nm while the 1064 nm beam is terminated in a beam dump. The 532-nm beam passes through a combination two half-wave plates and two polarizers for

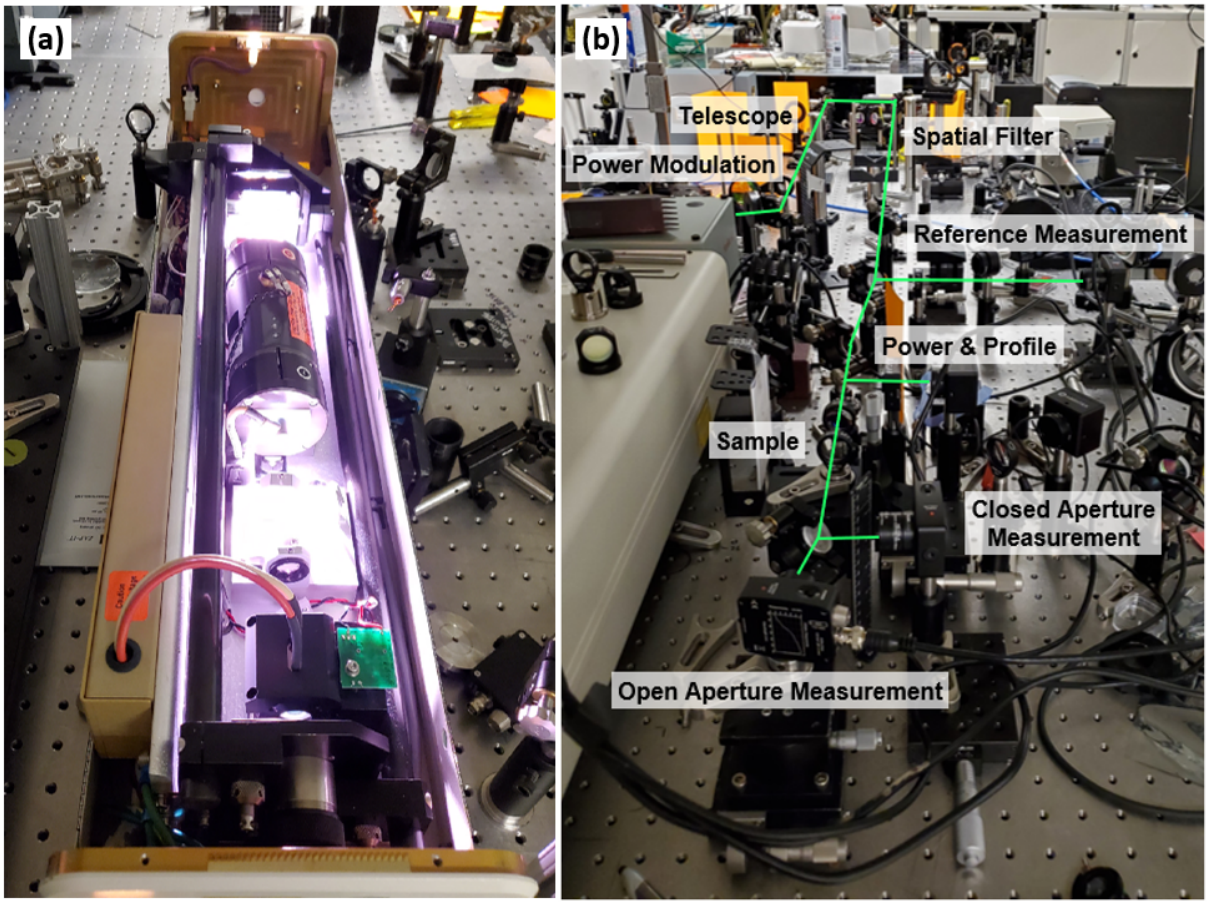

Figure 2.5: (a) Surelite II-10 laser head opened for alignment of resonance cavity mirrors and flashlamp maintenance. (b) Z-scan laboratory proof of concept with Surelite II-10 laser head at the left edge of the image.

power modulation. The first half-wave plate and polarizer are set to prevent the laser power from exceeding the damage threshold of the supporting optics of the Z-scan, such as the lenses and mirrors. The second set of half-wave plate and polarizer are used to fine tune the laser power to be near the damage threshold of the optical material under examination to maximize the nonlinear signals of the Z-scan.

The laser is next conditioned to obtain a nearly Gaussian (TEM_{00}) spatial mode that is essential to obtain an adequate Z-scan signal and to accurately estimate the nonlinear coefficients from the simulation [12, 13]. A convex and concave lens are first used in the configuration of a Galilean telescope to reduce the beam diameter from 6 mm to 1 mm.

The beam reduction is performed so that the laser may be gradually focused into the spatial filter by a 75 cm focal-length lens, with a high f-number of $f/\# = 750$. The purpose of the beam reduction and gradual focus with a high $f/\#$ is to avoid ablation of the spatial filter due to high laser intensity, which is common when spatially filtering a laser to obtain the TEM_{00} mode. To further reduce potential ablation of the spatial filter a custom fabricated 400 μm diameter diamond spatial filter with a copper heat sink plate manufactured by Lenox Laser is used. Figure 2.6 shows the spatial profile of the surelite output beam, the spatially filtered and collimated laser profile before the Z-scan focusing lens, and the laser profile at the extreme focus of the Z-scan experiment. The laser quality M^2 is measured using the second moment beam waist definition by Siegman, which for this spatial filtering configuration is $M^2 \approx 1.3$ [59]. Ablation of the

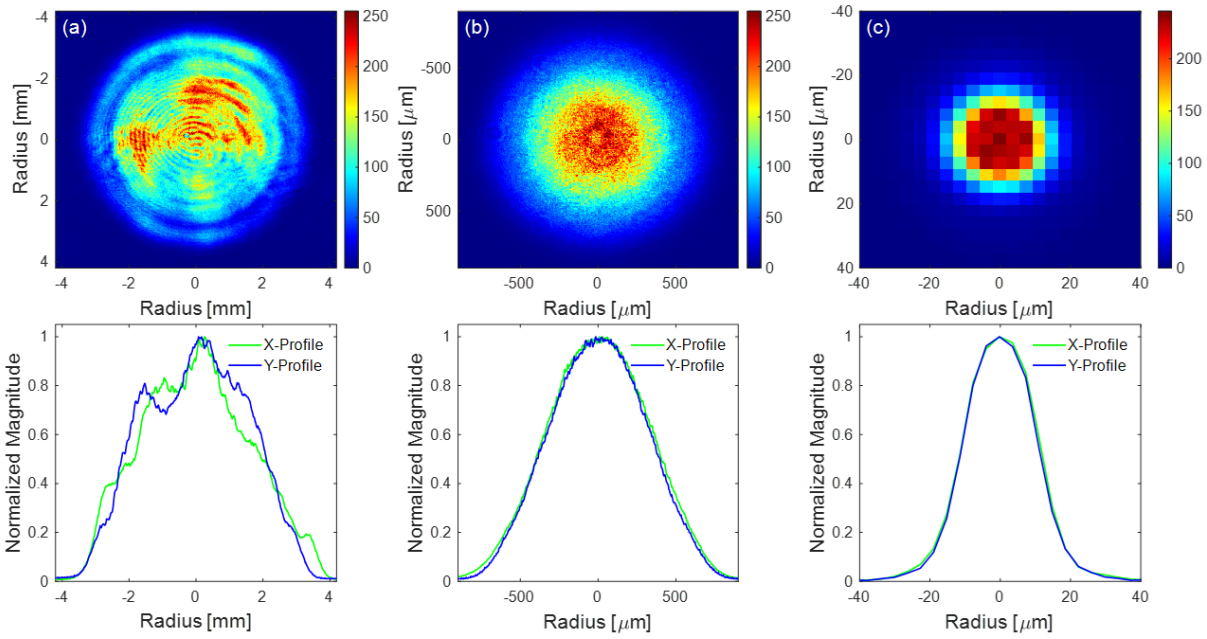

Figure 2.6: Surelite 532 nm spatial profile image with profile plot below (a) emerging from the harmonic beamsplitter, (b) after the spatial filter, and (c) at maximum focus in the Z-scan.

spatial filter would necessitate a vacuum system to prevent contamination and damage of the experiment optics from ablated spatial filter material, and replacement of the

spatial filter as the material degrades from laser ablation. Installation of a vacuum system and frequent replacement of the spatial filter would significantly hinder the long term and repetitive performance of the Z-scan experiment over the duration of many measurements of irradiated and thermally annealed materials, hence why a nondestructive spatial filtering system is developed. The cost of such a system however is the increased dimensions of the Z-scan experiment, specifically the additional 160 cm of beam length added to the setup to reduce the beam diameter, spatially filter the beam, and expand a collimate the beam after spatial filtering. As will be seen in the compact and self contained configuration of the Z-scan PIE system, this space cost is managed. The nondestructive spatial filtering was successful as the spatial filter in the Z-scan did not need to be replaced during 10 months of continuous use and exposure to $\sim$ 20 million laser pulses.

After the spatial filter the beam is allowed to expand again to a 1 mm diameter and is collimated by a lens. A Lenox Laser custom molybdenum high-power aperture is used immediately after the collimating lens to trim the Airy diffraction rings from the laser profile induced by the spatial filtering. Trimming the Airy rings produces the singular central Gaussian spatial profile seen in Figure 2.6 and prevents the diffraction rings from potentially causing interference as the laser is focused into the optical material sample during the Z-scan. At this point $\sim$ 98 % of the laser pulse power has been lost due to spatial filtering and trimming of the diffraction rings, which is another cost of a gradual focus into a spatial filter. The maximum average power allowable for the pulse at this point due to optical damage thresholds of the supporting optics is $\sim$ 2.8 mW. This was anticipated in the design however and is more than sufficient to achieve the damage thresholds of the optical materials at focus in the Z-scan experiment.

After trimming the Airy rings the laser profile is considered to be conditioned appropriately for the Z-scan by obtaining the nearly Gaussian mode, and the Z-scan experiment

begins with sampling and characterizing the laser pulse temporal, spatial, and power profiles. The laser pulse characterization begins at wedge 1 in Figure 2.7, where the optical wedge reflects ~ 10 % of the beam into two reflected beams. The primary perpendicular beam is reflected into the reference photodiode which, according to its label, serves as a reference pulse power measurement for each signal pulse measured by identical photodiodes in OA and CA configurations after the optical material sample during the Z-scan. An example of the measured laser pulse by the photodiodes is shown in Figure 2.7(a). The secondary wedge reflection is directed to a fast photodiode, as depicted in Figure 2.4, to obtain the temporal profile shape. The temporal profile measurements are used to obtain the effective temporal pulse duration, $\tau_e \approx 5$ ns, using the following relation where p represents the temporal profile measured by the fast photodiode similar to the profile shown in Figure 2.7(a) [54]

$$\tau_e = \frac{1}{\sqrt{2\pi}} \frac{\left(\int p\left(t\right) dt\right)^2}{\int p^2\left(t\right) dt}. \tag{2.1}$$

A second wedge equivalent to the first wedge and opposed 180° is used to steer the beam to the Z-scan focusing lens and counter any aberrations induced in the beam by the first wedge. A removable mirror is located after this wedge and before the Z-scan focusing lens to direct the beam to a power meter and CMOS camera. The power meter is used to set the laser power incident in the optical sample to near the damage threshold by manipulating the second half-wave plate and polarizer combination discussed earlier. The CMOS camera is used to check the beam quality and align the spatial filter if necessary. The CMOS camera is also used to characterize the beam profile at focus by mounting it to the optical sample holder and imaging the beam profile at the focal point of the Z-scan focusing lens. With this image and the known input beam profile the effective area A_{eff}

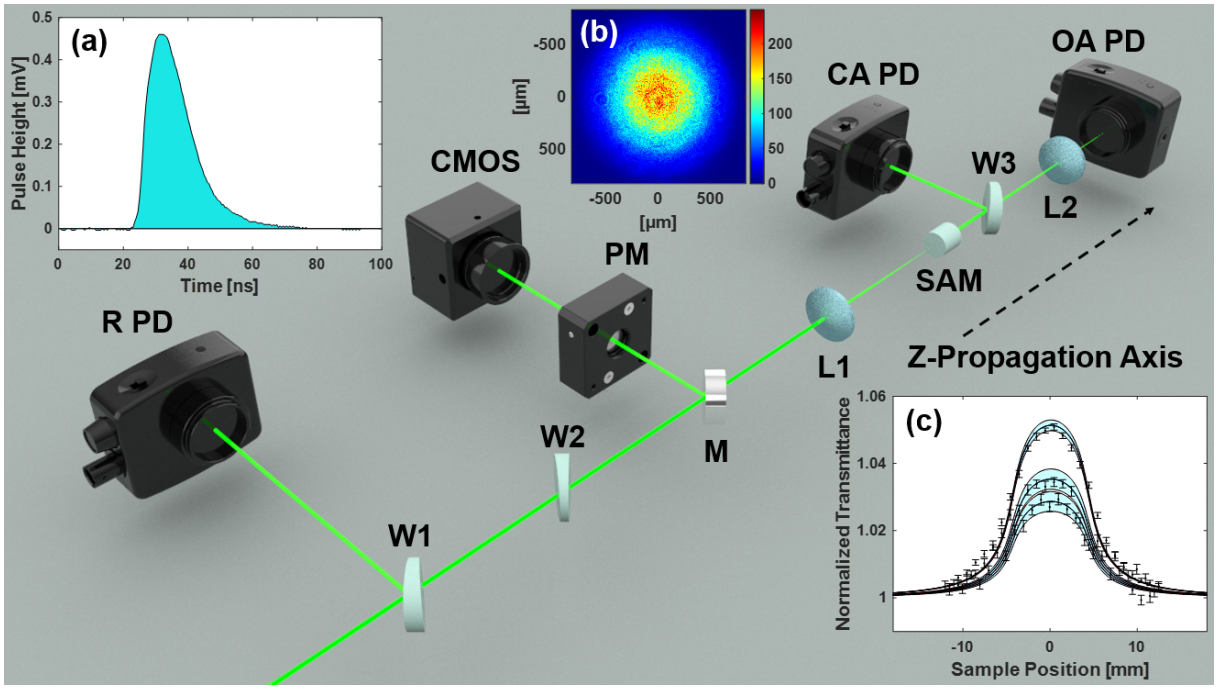

Figure 2.7: Z-scan experiment after spatial filtering: optical wedges (W1–3), the reference (R PD), closed-aperture (CA PD) and open-aperture (OA PD) photodiodes, power meter (PM) and CMOS camera after a removable mirror (M), focusing lenses (L1, L2), and the optical sample (SAM) under examination. Inset: (a) an example pulse time profile, (b) spatially filtered laser beam profile, and (c) normalized transmittance curves obtained by the ratio of the OA photodiode to the reference photodiode during an open-aperture Z-scan measurement.

is obtained, as is the Rayleigh length at focus, z_R, using the following relations [15]

$$A_{eff} = A_{pixel} \cdot \sum_{pixels} I_{pixel}\left(i,j\right) / max_{pixels}\left[I_{pixel}\left(i,j\right)\right]. \tag{2.2}$$

$$z_R = \frac{\pi \omega_f^2}{\lambda}. \tag{2.3}$$

Here A_{pixel} is the area of each pixel of the CMOS camera, I_{pixel} is the integer value of the pixel at coordinate (i,j), max_{pixels} is the maximum pixel integer value over the entire camera, ω_f is the beam waist at focus which is determined from A_{eff}, and λ is the laser wavelength. Using this method a Rayleigh length of $z_R = 1.2$ mm is obtained.

The measured power, effective pulse duration, and Rayleigh length at focus are the three experimental parameters necessary to simulate the Z-scan to extract the nonlinear coefficients from the measured Z-scan curves, as will be discussed later in this section.

Continuing in Figure 2.7, after the removable mirror is located the final Z-scan focusing lens (L1). For this experiment a 5 cm fused silica focusing lens is used. The fused silica lens does not have an anti-reflective coating as the coating was found to damage, likely from focused back reflections produced by the samples as they are translated through the Z-scan. The optical material sample is located near the focal position of the lens mounted to an electronic translation stage which is controlled by LabVIEW software on a computer. The translation stage has a travel range of 25 mm, which is a compromise between the large translation range necessary for thick sample Z-scans but the compact space requirements necessary for the PIE system. The Z-scan uses the full 25 mm range for each measurement, in 0.5 mm segments, for a total of 51 measurement positions for each Z-scan. The central position of the Z-scan is set by moving the location of the focusing lens along the laser propagation Z-axis and positioning the lens to center the maximum nonlinear effect within the translation stage range. This requirement to move the focusing lens relative to the translation stage reinforces the necessity for a precise and consistent alignment of optics throughout the Z-scan experiment to ensure a well collimated and constant beam profile is directed into the Z-scan focusing lens and sample.

After the optical material sample is a third wedge. The primary reflection of the third wedge is directed to the CA photodiode, while the main beam continues after the wedge into the OA photodiode. The reference, CA, and OA photodiodes are identical Thorlabs DET36A2 silicon photodiodes with 14 ns rise times. Each photodiode is filtered appropriately to prevent saturation of the diode, and the filtering is tailored specifically for each optical material type and the material's Z-scan power setting near the damage

threshold. A lens is also located after the third wedge to focus the expanding beam onto the OA photodiode to ensure the entire beam is captured on the 13 mm^2 sensor area. The reflected beam continues to expand before impinging on the 700 μm diameter aperture of the CA photodiode, which produces a transmittance $S \approx 0.1$ [13]. The CA photodiode is mounted on a two axis translations stage so that it may be aligned to the center of the incident beam using an oscilloscope and maximizing the signal voltage when the optical sample is far from the focal position.

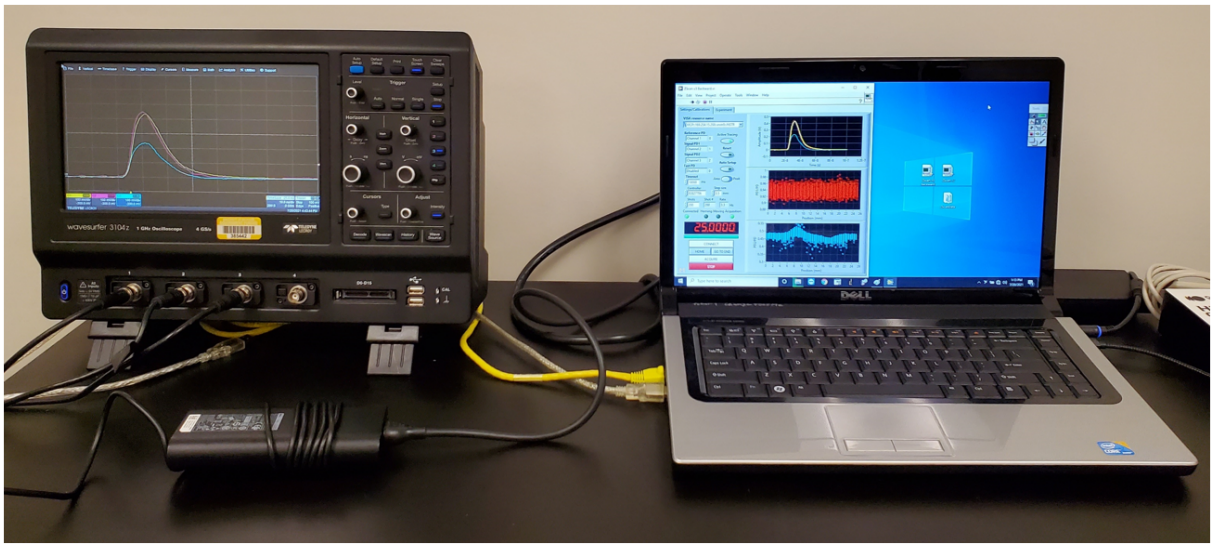

Figure 2.8: DAQ system with oscilloscope on the left and computer running the LabVIEW software for Z-scan data collection on the right.

The execution of the Z-scan experiment is automated via LabVIEW software that controls the electronic translation stage of the optical material sample while simultaneously collecting the correlated pulse measurements of the reference, CA, and OA photodiodes. Figure 2.8 shows the DAQ system consisting of a Teledyne LeCroy Wavesfurfer 1 GHz oscilloscope and computer running the LabVIEW control and acquisition program. The program moves the sample via the translation stage to each position and proceeds to record all three correlated photodiode signals triggered by the reference photodiode. The position increments and the number of measurements per position may be customized

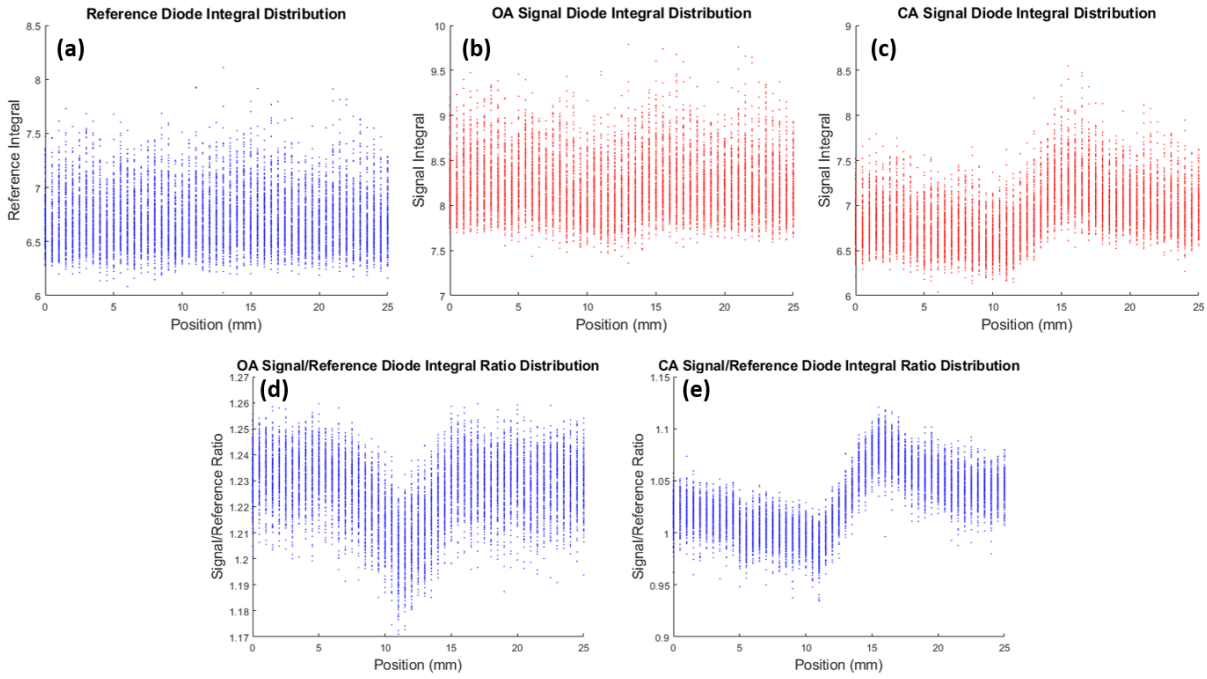

Figure 2.9: Correlated pulse data from the first successful Z-scan using BK7 borosilicate glass. (a) Reference photodiode, (b) OA photodiode, and (c) CA photodiode pulse integral distributions for 200 pulses per position. (d) Ratio of OA to reference photodiode correlated pulse integrals and (e) ratio of CA to reference photodiode correlated pulse integrals. In (d) and (e) the rough shape of a nonlinear absorption and refraction measurement curve, respectively, can be seen.

in the software. The pulse data is saved onto the PC into text files for later processing in MATLAB software. OA and CA Z-scan curves are displayed in real time by the LabVIEW software, as are the signal pulses of the diodes on the oscilloscope. The real time display of data is useful for monitoring the progress of the Z-scan and in observing sample damage. Sample damage is evident by a loss of signal in the OA and CA photodiode signals on the oscilloscope, which results in the transmittance falling to zero on the Z-scan traces in the LabVIEW software. Damage may be verified by observing intense scattering in the optical material sample caused by the damaged spot.

A complete Z-scan using both an OA and CA configuration will provide the data set shown in Figure 2.9, which is the data obtained from the first successful Z-scan for this experiment using Thorlabs BK7 glass. For this Z-scan 200 pulses were recorded for each

position, and the sample was translated through the 25 mm translations range in 0.5 mm increments for a total of 51 positions. The first three plots (a through c) shows the pulse integral distributions for the reference, OA, and CA photodiodes. Plots (d) and (e) show the distributions of the ratios of the OA to reference and CA to reference pulse integrals, respectively. The ratio distributions in (d) and (e) are averaged and the standard error is propagated, and the curves are normalized to unity per Z-scan convention to form the characteristic open and closed aperture Z-scan curves shown in Figure 2.10 [12].

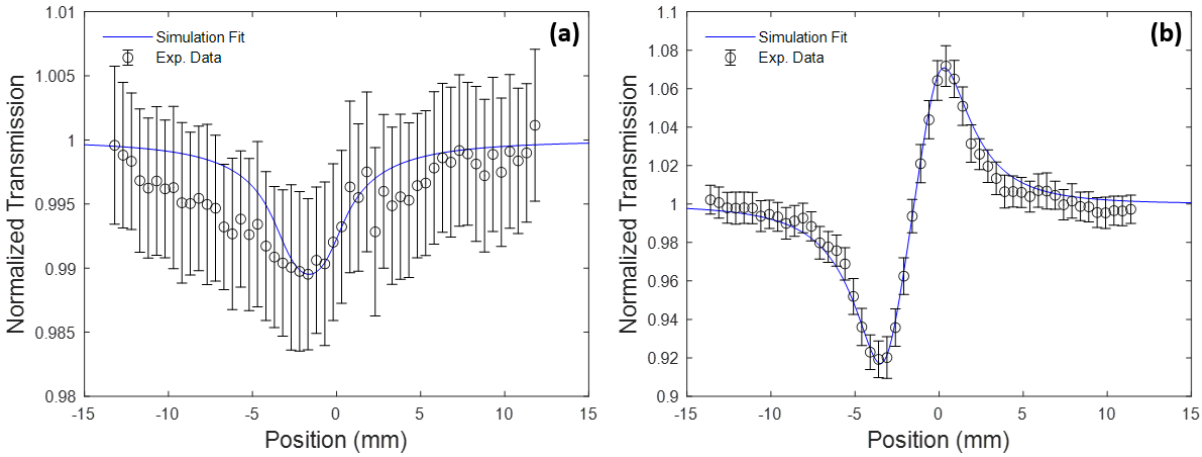

Figure 2.10: Z-scan measurements of a Thorlabs BK7 window sample. (a) OA measurement of NLA and (b) CA measurement of NLR.

Figure 2.10 represents the first successful Z-scan curves obtained with this Z-scan experiment for a 5 mm thick Thorlabs BK7 borosilicate glass sample. Figure 2.10(a) is the OA curve that represents the measurement of NLA, and Figure 2.10(b) is the CA curve that represents the measurement of NLR. The experimental data with error bars is the mean of the ratio distributions shown in Figure 2.9 and the propagated standard error, respectively. The blue curve represents the simulation fit using the first-order theory of Hermann and McDuff for think samples [13, 55, 57]. The simulation of the Z-scan curve is the means by which the coefficient values for NLA and NLR are estimated. The thick sample simulation is appropriate here because the sample width $L = 5$ mm is greater than the Rayleigh length at focus $z_R = 1.2$ mm. The first-order theory of

Hermann and McDuff accounts for the axial shift of the beam waist location caused by the linear refractive index n_0 within a thick sample, which is illustrated in Figure 2.11. Here the dashed line represents the unshifted propagation of the focused laser through

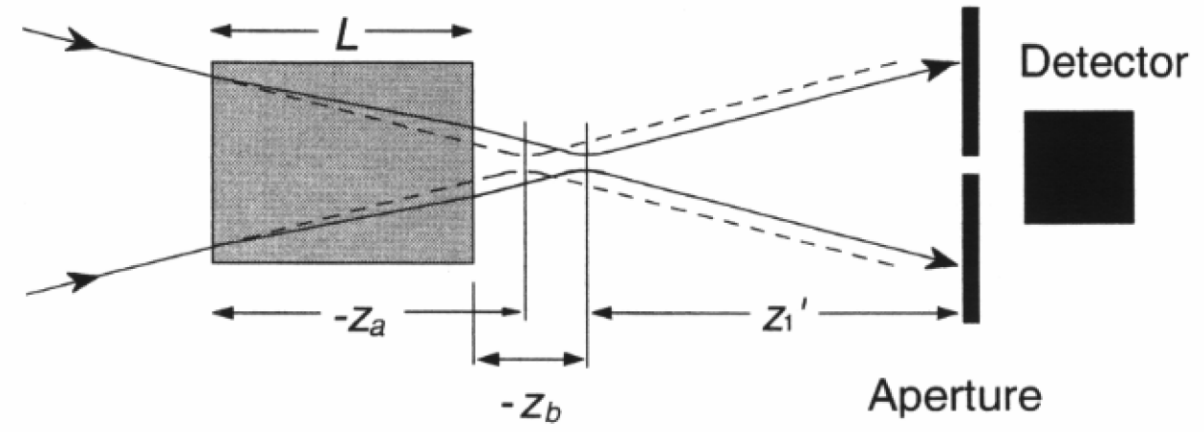

Figure 2.11: The thick sample scenario, with a CA detector, of an optical material sample translating through the focus of an intense laser with the unshifted beam waist (dashed line), and the shifted beam waist (solid line) caused by the linear refractive index within the thick sample [55].

the sample. The solid line represents the shifted position of the waist of the focused laser propagated through the sample due to the reduced rate of beam evolution over the length of the sample, which is proportional to $L(1-1/n_0)$. As the sample approaches focus this shift becomes more prominent due to the nonlinear effect of self focusing, shifting the beam waist location in addition to changing the beam waist and Rayleigh length. These changes become even more prominent in the thick sample regime, and so the assumption of the thin sample approximations discussed in Chapter 1 are no longer valid. Herman and McDuff approximate the solution to the nonlinear wave equation in the thick sample regime by treating the wave propagation to the first order in the nonlinear phase shift, $\Delta\Phi_{0R}$, for small nonlinearities [13, 55, 57]. This is an appropriate approximation due to the small reported values of n_2 for the optical materials intended for this study and is in fact the reason why the thick sample approach is taken with optical materials [7]. The

transmittance according to this solution is given by

$$T = 1 + \frac{1}{4}e^{\alpha_0 n_0 z_a}\Bigg[\left(\Delta\Phi_{0R} + \frac{1}{2}Q_{0R}A\right)\ln\left(1+\nu^2\right) - \left(\Delta\Phi_{0R} - \frac{3}{2}Q_{0R}A\right)\ln\left(9+\nu^2\right) + \left(Q_{0R} - 2\Delta\Phi_{0R}A\right)\tan^{-1}\nu + \left(Q_{0R} + 6\Delta\Phi_{0R}A\right)\tan^{-1}\left(\nu/3\right)\Bigg]_{\nu_a}^{\nu_b} \tag{2.4}$$

Here $\Delta\Phi_{0R}$ is the nonlinear phase-shift as previously mentioned, Q_{0R} is the absorption, ν is a linear phase parameter for the sample entrance and exit face, z_a is the distance from the unshifted beam waist to the sample entrance face, and z_b is the distance from the shifted beam waist to the sample exit face. Figure 2.11 illustrates these parameters in addition to z_1', the distance from the shifted waist to the observation plane of the detector. These parameters are further defined below where the parameter d is the distance from the unshifted beam waist to the observation plane of the detector [55]:

$$\Delta\Phi_{0R} = \frac{2\pi}{\lambda}n_2 I_0 n_0 z_R, \tag{2.5}$$

$$Q_{0R} = \beta I_0 n_0 z_R, \tag{2.6}$$

$$\nu_i = \frac{1}{z_R}\left(z_i + \frac{z_R^2 + z_i^2}{z_1' - z_i}\right) \text{ for } i = a, b, \tag{2.7}$$

$$z_b = z_a + \frac{L}{n_0}, \tag{2.8}$$

$$z_1' = d - z_a - z_b - L, \tag{2.9}$$

$$A = \alpha_0 n_0 z_R. \tag{2.10}$$

The simulation is carried out in MATLAB by fitting Equation 2.4 to solve for the β and n_2 with z_R and I_0 determined by from the pulse profile parameters previously discussed, and z_a treated as the sample position [15, 54]. Known samples including borosilicate

glass and fused silica were used to validate the simulation based on their listed nonlinear coefficients in literature [7, 12].

Upon successful execution of the first Z-scans with BK7 borosilicate glass the Z-scan experiment was transitioned to the compact and self-contained configuration for the PIE system, shown in Figure 2.12. The experiment was mounted to a wheeled 550 lb capacity laboratory cart for transport and operation. The optics supporting the Z-scan experiment were reconfigured and mounted with the laser head within a class IV laser barrier on a Nexus honeycomb optical breadboard as seen in Figure 2.12(a) and according to the design presented in Figure 1.12. Initial tests of the PIE configured Z-scan revealed severe Z-scan instability due to shifting of the optics, particularly the spatial filter, as a result of thermal expansion of the optical mounting plate from heat generated by the laser during operation. The instability was identified by observing null Z-scans without an optical sample present and noting that the CA Z-scan curve did not remain at unity (display a flat line) as the z s-can progressed through the positions. This observation indicated a change in alignment of the spatial filter and degradation of the beam quality and pointing stability, resulting in misalignment on the CA photodiode aperture and inconsistent transmission due to the poor pointing stability. The misalignment of the spatial filter would have implications for the CA measurement as well if a sample were present in that the nonlinear absorption would be less prominent with a degraded beam quality, and the beam may become misaligned from the detector as well if the spatial filter become displaced enough. This problem was remedied by installation of the Nexus honeycomb optical breadboard which stabilized the optics as the laser heated and reduced the variation of the null Z-scans to 0.6 %, which allows the measurement of expected small NLA and NLR curves of 2 % to 6 % magnitude change as expected with materials such as fused silica and borosilicate glass.

Final validation of the Z-scan consisted of integration of the DAQ and measurement

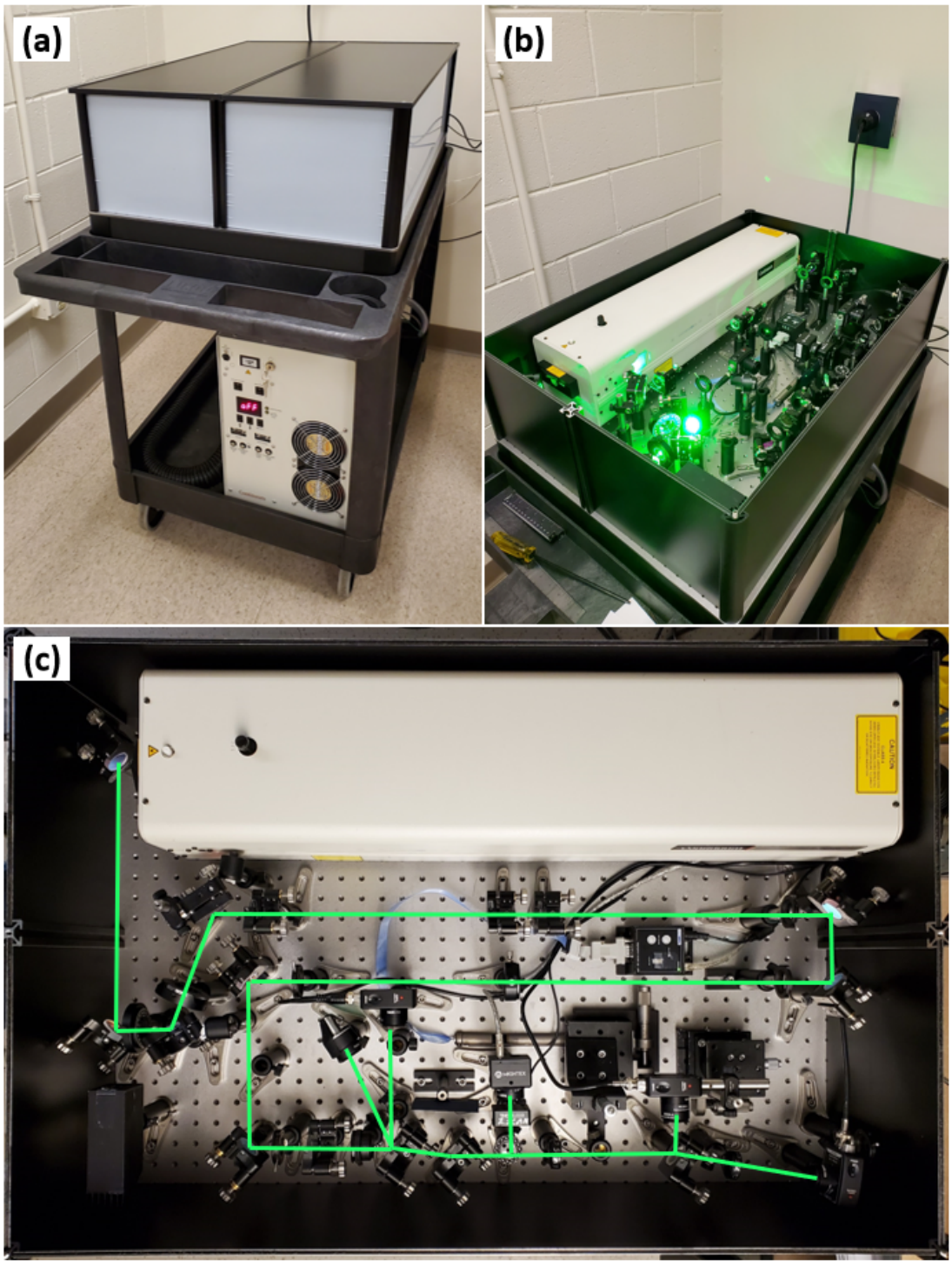

Figure 2.12: (a) The PIE sytem with the laser power control unit mounted in the lower deck and the class IV laser barrier surrounding the upper deck. (b) The operational Z-scan experiment in the PIE system at the OSU NRL. (c) Z-scan experiment reconfigured within the PIE system class IV laser barrier.

of known fused silica and sapphire NLR indices. The DAQ LabVIEW program with oscilloscope and computer was tested repeatedly to refine how the data was recorded into text format for simplicity of transfer to MATLAB for data processing, with pulse data for all three photodiode sensors written to one individual text file per measured laser pulse. Initial validation Z-scans were performed by recording 200 pulses every 0.5 mm over the 25 mm scan range for a total of 51 positions, resulting in 10,200 text files per Z-scan and each Z-scan requiring $\sim$ 1 hour to complete. Validation Z-scans of S2000, I302, and sapphire samples with widths of L = 12.7 mm are shown in Figure 2.13. Known n_2 values from literature for each sample type were used to validate the simulation of each Z-scan [7]. These three samples each had NLA coefficients that were too small for

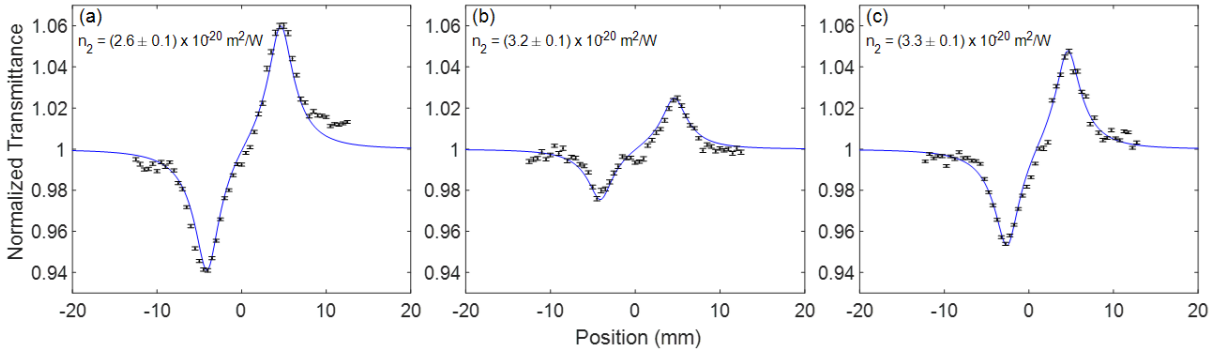

Figure 2.13: Validation Z-scans using literature values for n_2 of (a) S2000, (b) I302, and (c) sapphire. The known n_2 values for simulation validation are provided in each plot.

this Z-scan experiment to detect, but Schott NBK7 borosilicate glass samples with width L = 12.7 mm were later obtained and the NLA measurements were validated, which is shown in Figure 1.13(b). After validation the PIE system was moved by truck to the OSU NRL into a dedicated laser laboratory in the NRL annex adjacent to the nuclear reactor. The PIE system was set up within 24 hours to analyze samples which included cleaning and alignment of optics after transportation. To allow expedient completion of the multiple Z-scans required during irradiation experiments the number of measurements per position was changed to 40, and the position increments were increased to 1 mm,

reducing the Z-scan times to $\sim$ 20 minutes. This change is reflected in all the following Z-scan plots presented in this manuscript.

Chapter 3

Irradiation and Thermal Annealing Testing

Irradiation of optical material samples took place primarily at the OSU NRL nuclear reactor, shown in Figure 3.1, and the co-located ^{60}Co irradiator dry tube facility. A single sample of I302 was also irradiated at the Pennsylvania State University (PSU) Radiation Science and Engineering Center (RSEC). Post and concurrent-irradiation thermal annealing of irradiated samples was also performed at the NRL. The PIE system was located at the NRL annex building adjacent to the nuclear reactor. This allowed expedient examination of irradiated and thermally annealed optical material samples by reducing the time between irradiation, thermal annealing, and examination. The ultimate goal of this process was to obtain nearly *in-situ* and real-time information on the optical characteristics of materials under the conditions of simultaneous irradiation and thermal annealing.

The OSU NRL ^{60}Co irradiator produces 1.17-MeV and 1.33-MeV gamma rays at an average dose rate in Si of 12.38 krad $\cdot$ hr^{-1} inside the sample annealing furnace and dry tube where the samples were suspended for exposure. The decay of ^{60}Co and the resultant change of dose rate are accounted for over the duration of the experiments to ensure a consistent gamma dose is received for comparison of post- and concurrent-irradiation

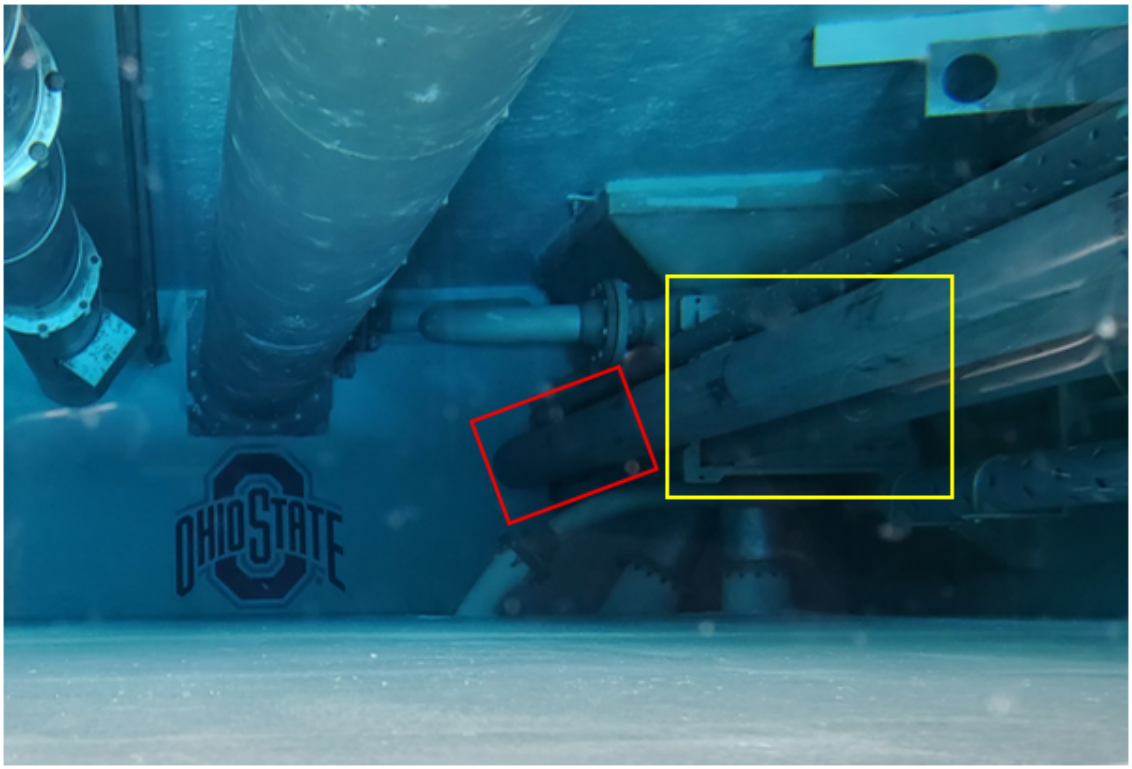

Figure 3.1: The OSU NRL nuclear research reactor. The core is denoted by the yellow box, and a movable dry tube is situated next to the core denoted by the red box.

Table 3.1: Irradiation and thermal annealing conditions. The estimated gamma dose for each neutron fluence is provided below in parenthesis. All indicated gamma doses are silicon-equivalent, and all neutron fluences are total (fast and thermal).

Source	Dose/Fluence	Anneal Type	Temp.	Time
^{60}Co	600 krad 1.2 Mrad 3.6 Mrad 10 Mrad	Post	200 °C 400 °C 600 °C 800 °C	30 min. 30 min. 30 min. 30 min.
^{60}Co	600 krad 1.2 Mrad 3.6 Mrad	Concurrent	800 °C	Duration
Reactor	3.4×10^{16} n $\cdot$ cm^{-2} (42 Mrad) 1.7×10^{17} n $\cdot$ cm^{-2} (211 Mrad)	Post	200 °C 400 °C 600 °C 800 °C	30 min. 30 min. 30 min. 30 min.
Reactor	3.4×10^{16} n $\cdot$ cm^{-2} (42 Mrad) 1.7×10^{17} n $\cdot$ cm^{-2} (211 Mrad)	Concurrent	800 °C	Duration

thermal annealing cases. The gamma flux inside the thermal annealing furnace mounted within the NRL ^{60}Co dry tube was measured by four single-point radiation monitoring nanoDot dosimeters spread across the 6-inch peak flux profile. The PSU RSEC utilizes a cylindrical fixture with surrounding ^{60}Co gamma sources that supplies a dose rate of 18 krad $\cdot$ hr^{-1} within a 4 in. diameter by 4 in. depth cylindrical isodose region. One I302 material sample was mailed to PSU for irradiation to 10 Mrad and was mailed back to OSU for PIE and thermal annealing. The gamma doses and associated annealing temperatures are listed in Table 3.1.

The OSU NRL nuclear reactor flux was estimated inside of the furnace by irradiating bare and cadmium-covered sets of metal rods and comparing their post-irradiation gamma-ray emission spectrum using the Spectrum Analysis by Neutron Detectors iterative computer code [60]. The estimated neutron fluxes inside the furnace inserted into the nuclear reactor dry tube adjacent to the core were 1.7×10^{12} n $\cdot$ cm^{-2}s^{-1} total, 1.3×10^{12} n $\cdot$ cm^{-2}s^{-1} thermal ($E_n < 0.5$ eV), and 4.4×10^{11} n $\cdot$ cm^{-2}s^{-1} fast (epi-cadmium, $E_n > 0.5$ eV), and the gamma dose rate was 7.6×10^6 rad $\cdot$ hr^{-1}. The estimated gamma and neutron fluxes were used to determine the reactor doses in Table 3.1. The two reactor neutron doses listed in the table of 3.4×10^{16} n $\cdot$ cm^{-2} and 1.7×10^{17} n $\cdot$ cm^{-2} are referred to throughout the text as n-Dose 1 and n-Dose 2, respectively. All neutron irradiations were performed with the samples mounted within the furnace by the silica-based mounting hardware within the furnace, which is inserted into the nuclear reactor dry tube.

A photograph of the thermal annealing furnace suspended above the ^{60}Co irradiator dry tube is provided in Figure 3.2(a). The samples were suspended within the furnace using silica-based sample mounting hardware shown in Figure 3.2(b) during irradiations in the ^{60}Co dry tube and the nuclear reactor dry tube. The furnace was custom fabricated for insertion into the dry tube to allow for thermal annealing samples while they are being

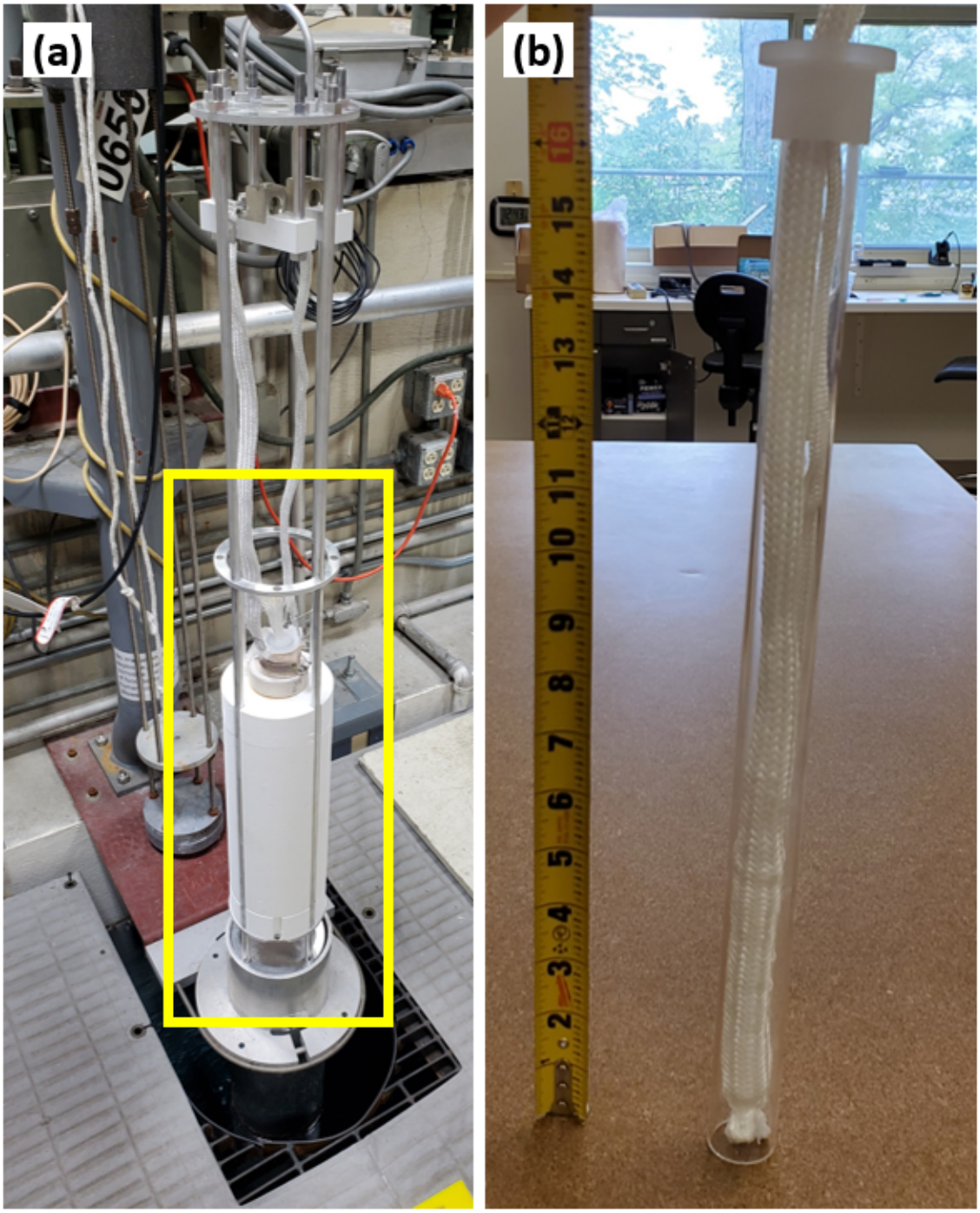

Figure 3.2: (a) Custom-fabricated furnace suspended for sample insertion into the ^{60}Co pool dry tube and concurrent thermal annealing. The silicon carbide heating element and silica-alumina insulation are denoted by the yellow box. (b) Fused silica tube and silica sleeve that suspend the window samples within the furnace's silicon carbide heating element and alumina insulation during irradiation.

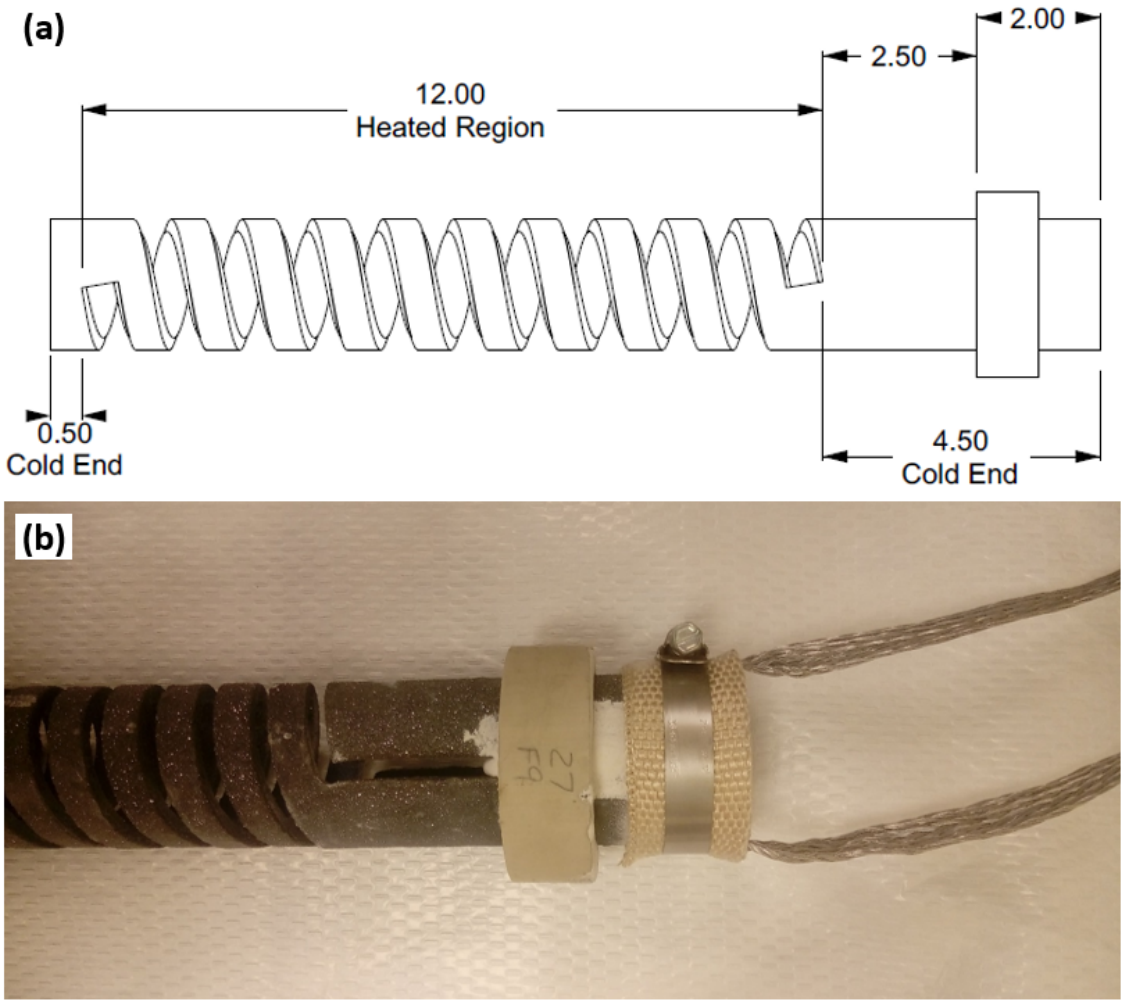

Figure 3.3: (a) Schematic of the thermal annealing furnace silicon carbide heating element that the samples are suspended within by silica-based mounting hardware (dimensions in inches). (b) Electronic leads coupled to the heating coil for temperature control [61].

irradiated, or to heat the samples post-irradiation external to the dry tubes. The window samples were stacked within the white silica sleeve shown in Figure 3.2(b), which was suspended within a silica glass tube to physically separate the samples from the furnace heating coil. A schematic of the silicon carbide heating coil is provided in Figure 3.3(a). The samples within the silica tube were then inserted vertically in the coiled heating element within the white insulated portion of the heater shown in the yellow box of Figure 3.2(a). Two thermocouples were mounted to the sample silica sleeve, adjacent to

the samples within the silica glass tube, to monitor temperature and ensure the samples do not overheat. The ambient temperature within the furnace inside the ^{60}Co dry pool was measured to be 20 °C and was assumed constant throughout the unheated irradiations.

Prior to each irradiation, every sample was characterized by Z-scan and spectroscopy to record the unirradiated linear attenuation and nonlinear properties. These same measurements were repeated again immediately after irradiation, in both the post and concurrent-irradiation thermal annealing cases. Samples subjected to post-irradiation thermal annealing were thermally annealed post-irradiation at 200 °C, 400 °C, 600 °C, and 800 °C, for 30 minutes at each temperature. After each annealing step the material samples were again evaluated by Z-scan and spectroscopy. For concurrent-irradiation thermal annealing experiments the samples were heated to 800 °C for the duration of the irradiation.

Table 3.2: Optical sample information

Material	Vendor	Type	OH Content
High-OH Fused Silica	Heraeus	Spectrosil 2000	$\leq$ 1300 ppm
Low-OH Fused Silica	Heraeus	Infrasil 302	$\leq$ 8 ppm
Sapphire	Guild Optical Associates	Optical Grade	
Borosilicate Glass	Schott JML Optical	NBK7	
Borosilicate Glass	Schott JML Optical	BK7G18	

The optical materials selected for examination are listed in Table 3.2. All samples were cylinders with a thickness of 12.7 mm and a diameter of 12.7 mm, with the axis of the cylinder parallel to and the Z-scan laser axis of propagation (z-axis). S2000 fused silica is a type III commercial silica with a high purity and high-OH content [8]. I302

fused silica is a type I commercial silica with a higher metallic impurity content than type III, the most significant being aluminium (20 ppm), and a lower OH content [8]. The sapphire is optical grade with the c-axis oriented normal to the flat optical face and parallel to the laser propagation axis. The Schott borosilicate glass (NBK7) is a popular and common crown glass free of lead and arsenic with high transmission range down to 350 nm, and the Schott radiation-resistant borosilicate glass (BK7G18) is crown glass doped with 1.8 w% cerium. The samples are shown in Figure 3.4 after irradiation to a total neutron fluence of 3.4×10^{16} n $\cdot$ cm^{-2} (42 Mrad γ). Prior to irradiation, the apparent transparency of all samples was similar to that of S2000, which is shown on the far left of Figure 3.4.

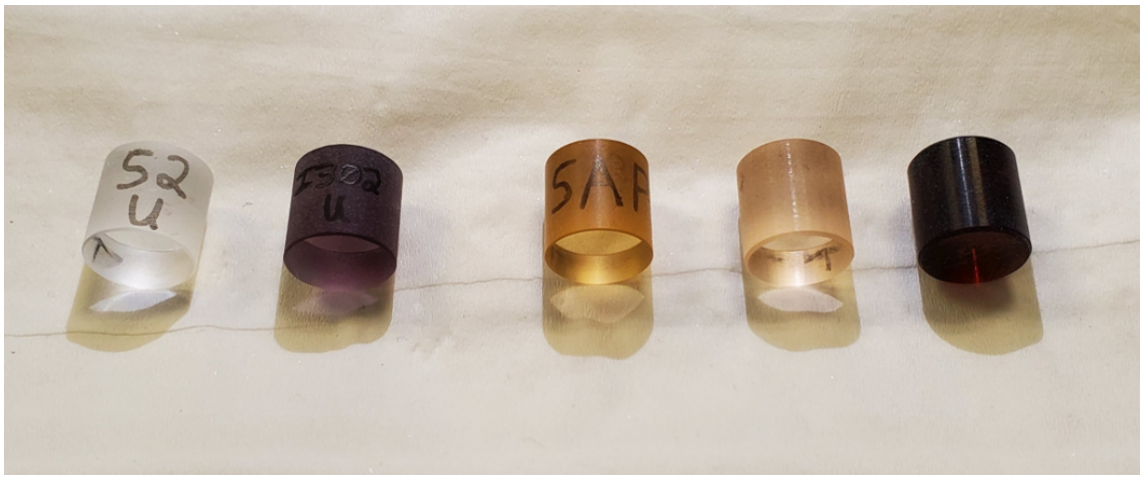

Figure 3.4: Window samples after irradiation to n-Dose 2 with total neutron fluence of 3.4×10^{16} n $\cdot$ cm^{-2} (42 Mrad γ). From left to right: S2000, I302, sapphire, BK7G18, and NBK7. The samples prior to irradiation were all as transparent as S2000 appears at left.

Radioactive decay of the optical samples following neutron capture reactions during neutron irradiation is a concern for the safety of experimenters during this research. A neutron activation analysis of each sample based on the manufacturer provided composition was performed using the National Institute of Standards and Technology Center for Neutron Research neutron activation and scattering calculator. Neutron activation

analysis of irradiated samples was also performed prior to performing the experiments by irradiating a set of the optical samples at the OSU NRL research reactor and measuring their gamma emissions and monitoring the decay activity. An example HPGe gamma-spectrum of sapphire following neutron irradiation is presented in Figure 3.5

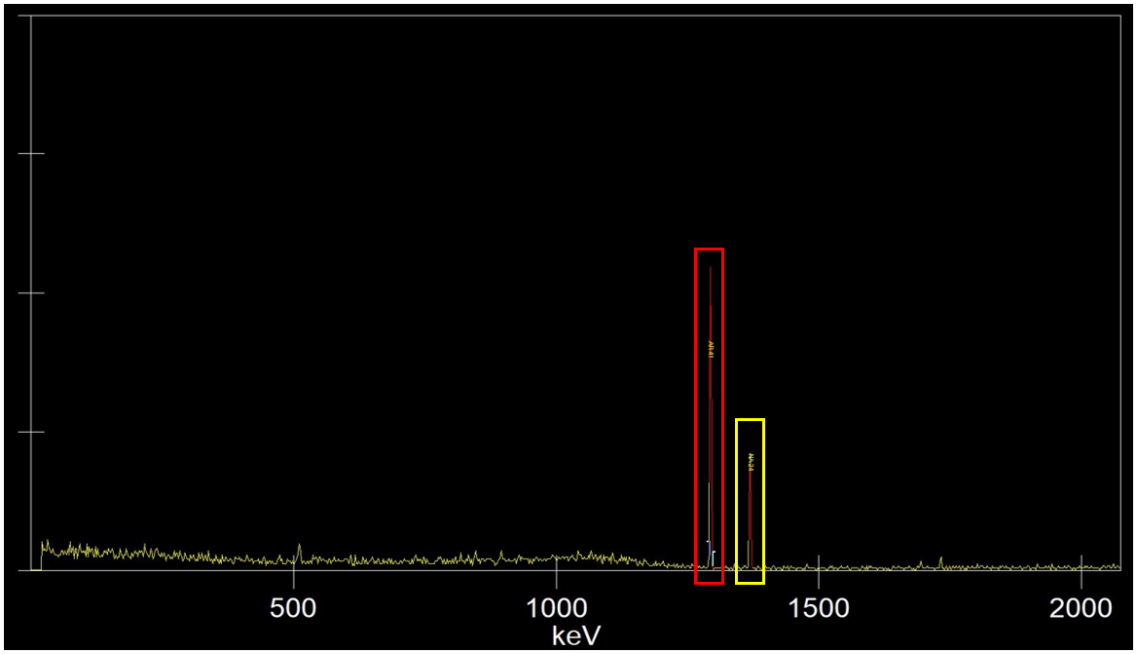

Figure 3.5: HPGe gamma spectrum of neutron activated sapphire immediately after irradiation. The red box denotes the gamma peak for ^{41}Ar, and the yellow box for ^{24}Na.

The two isotopes of greatest concern with significant activity following the analysis were ^{24}Na in NBK7 and BK7G18, and ^{141}Ce in BK7G18, both of which decay by beta and gamma emission. After each irradiation at the OSU NRL each sample was allowed to decay for 24-hours within the reactor dry tube. Upon extraction and for weeks after irradiation the two isotopes within NBK7 and BK7G18 presented the most significant radiation risk to researchers. Radiation exposure was minimized through a series of mitigating steps to ensure the dose received is as low as reasonably achievable. Gloves were worn at all times when handling samples and tongs were used to handle the radioactive samples to maximize the distance between the samples and the hands and bodies of personnel. Figure 3.6 shows the radioactive work table where optical samples were prepared

for examination, and the lead lined container for storage of radioactive materials when not in use. These radioactive work and storage areas were collocated with the PIE system

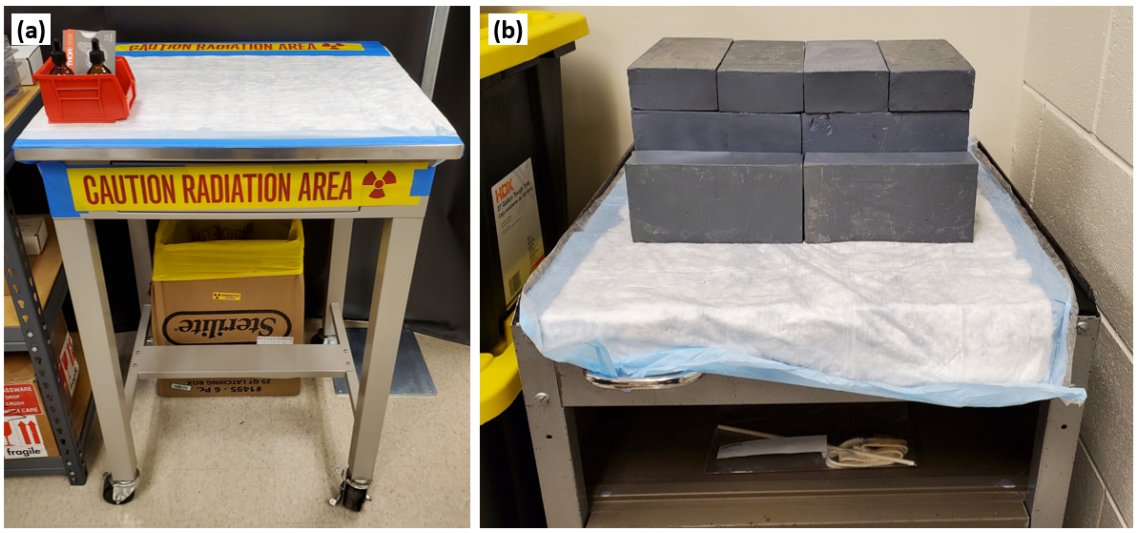

Figure 3.6: (a) The radioactive work table for cleaning and preparing optical samples for examination. (b) The lead lined container for storage of radioactive samples when not in use.

for ease of access. Each sample was measured with a handheld radiation detector upon extraction from the storage container and prior to performing work with it to determine if it safe to work with. Samples were additionally measured with a detector once in place in the Z-scan experiment to determine the dose rate in the room during experiments. It was found that the class IV laser barrier of the PIE system provided significant gamma and beta shielding while the sample was within the Z-scan. Once experiments were complete for the day and the samples were stored in the lead container, surfaces in the room, tools, and bags and clothing were scanned with a detector to ensure no radioactive material remained or was removed from the laboratory. Additionally, the staff at the OSU NRL performed routine weekly swipes of all the laboratory spaces to ensure no radioactive contamination was released. Hand and body dosimetry was worn at all times by researchers performing work with radioactive materials, and the dosimeters were evaluated every quarters to ensure dose limits were not exceeded.

Chapter 4

Radiation Induced Attenuation

4.1 Radiation Induced Attenuation Results

The radiation induced attenuation and the effects of post and concurrent-irradiation thermal annealing of S2000, I302, and sapphire are presented in this chapter. The results presented here are the spectroscopic measurements of the OD of the samples as described in Section 2.1. An analysis of the competing factors of radiation damage and thermal annealing is presented for each material.

The attenuation spectra of S2000 subjected to two neutron/gamma irradiation doses (n-Dose 1 and 2) and post-irradiation thermally annealed is shown in Figure 4.1. The corresponding attenuation spectrum of concurrent-irradiation thermally annealed S2000 irradiated to n-Dose 1 and 2 is presented in Figure 4.2. In the case of S2000 annealed post-irradiation, for both doses, its unirradiated attenuation spectrum is restored after thermal annealing to 600 °C for 30 min. A significant increase in OD is observed from n-Dose 1 to n-Dose 2. The most significant attenuation peak is centered at 213 nm, and a subdued peak is also observed at 246 nm. In the case of concurrent-irradiation thermally-annealed S2000 presented in Figure 4.2, it can be seen that the OD does not return to the unirradiated state after thermal annealing at 800 °C for the duration of irradiation.

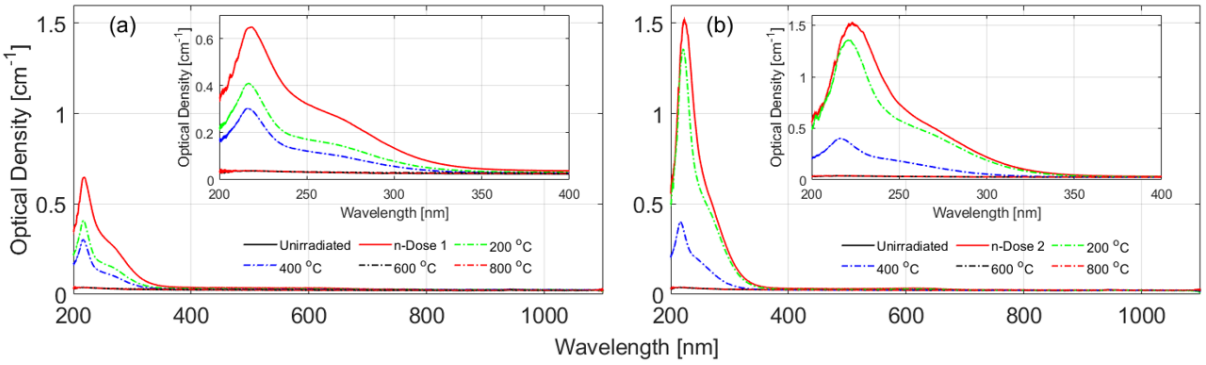

Figure 4.1: Post-irradiation thermally annealed attenuation spectra for S2000 irradiated to (a) 3.4×10^{16} n $\cdot$ cm^{-2} (n-Dose 1) and (b) 1.7×10^{17} n $\cdot$ cm^{-2} (n-Dose 2).

A residual attenuation peak remains in the S2000 centered around 213 nm, and the magnitude of the residual attenuation peak increases with dose. The gamma-irradiated S2000 did not exhibit an OD change for all of the gamma doses listed in Table 3.1, which is consistent with previous work at similar gamma doses [62].

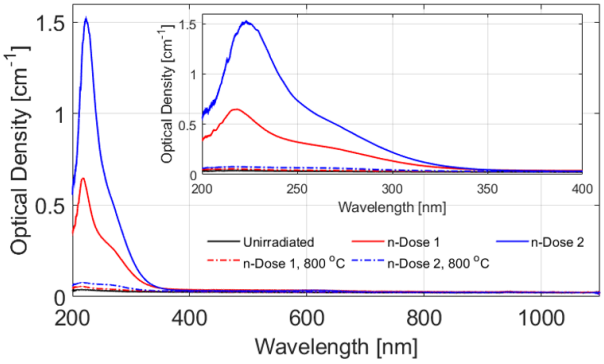

Figure 4.2: Concurrent-irradiation thermally annealed attenuation spectrum for S2000 irradiated to 3.4×10^{16} n $\cdot$ cm^{-2} and 1.7×10^{17} n $\cdot$ cm^{-2}, compared to the post-irradiation attenuation spectrum for equivalent fluences.

Figures 4.3, 4.4, 4.5, and 4.6 show the gamma- and neutron-irradiated I302 attenuation spectra for the post- and concurrent-irradiation thermal annealing cases. Increased attenuation peaks centered at 213 nm and 300 nm are observed following all gamma irradiations. In all of the gamma irradiations, the attenuation spectrum is shown to restore to the unirradiated state when annealed to 800 °C. As the gamma dose increases,

a subtle attenuation peak at 213 nm is the only gamma-enhanced attenuation feature remaining after annealing to 600 °C. Figure 4.4 also shows that the I302 is restored to its unirradiated state when concurrently annealed at 800 °C for the duration of each gamma irradiation.

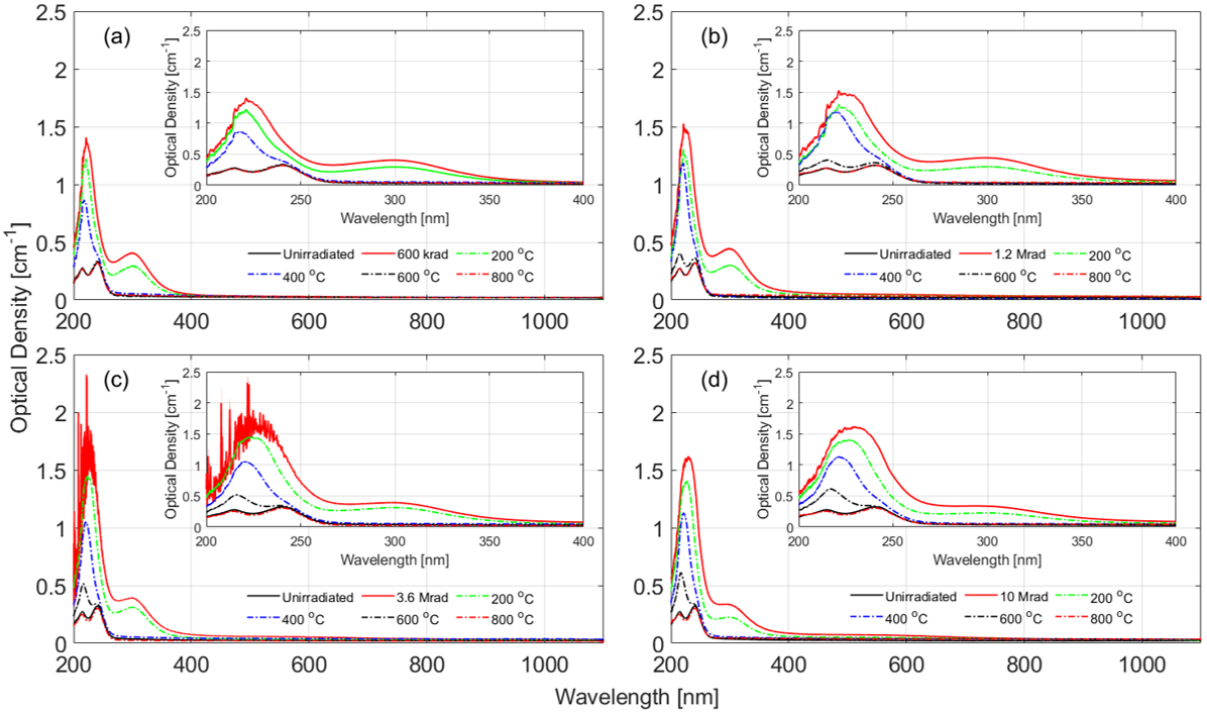

Figure 4.3: (a) Post-irradiation thermally annealed attenuation spectrum for I302 irradiated to gamma doses of 600 krad, (b) 1.2 Mrad, (c) 3.6 Mrad, and (d) 10 Mrad.

Neutron-irradiated I302 exhibits, in addition to the peaks at 213 nm and 300 nm, an additional broad attenuation band centered at 540 nm that extends up to 900 nm, which can be seen in Figure 4.5. The 540-nm attenuation band is shown to reduce to the unirradiated attenuation state after annealing to 400 °C. Annealing to 800 °C restores the I302 attenuation spectrum to the unirradiated state in the case of n-Dose 1, but after annealing to 800 °C in the case of n-Dose 2, the enhanced attenuation peak at 213 nm remains. In the case of concurrent-irradiation annealing of I302 for n-Dose 1, as seen in Figure 4.6, annealing to 800 °C for the duration of the irradiation does not restore the sample to the unirradiated state. Both attenuation spectra are nearly identical to

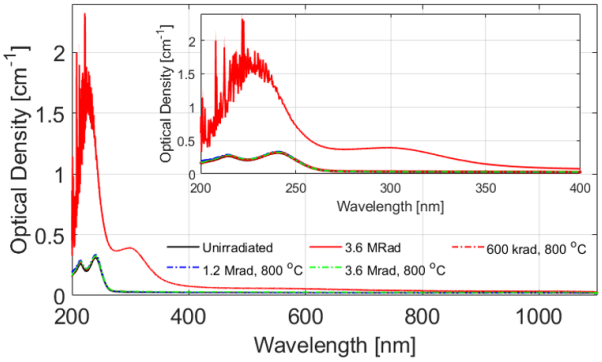

Figure 4.4: Concurrent-irradiation thermally annealed attenuation spectrum for I302 irradiated to 600 krad, 1.2 Mrad, and 3.6 Mrad, compared to the 3.6 Mrad gamma-irradiated sample attenuation spectrum.

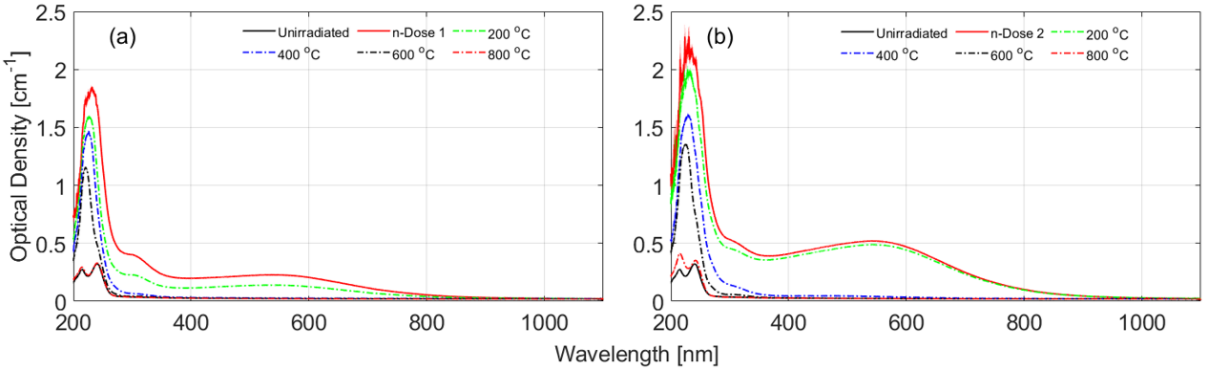

Figure 4.5: Post-irradiation thermally annealed attenuation spectra for I302 irradiated to (a) 3.4×10^{16} n $\cdot$ cm^{-2} (n-Dose 1) and (b) 1.7×10^{17} n $\cdot$ cm^{-2} (n-Dose 2).

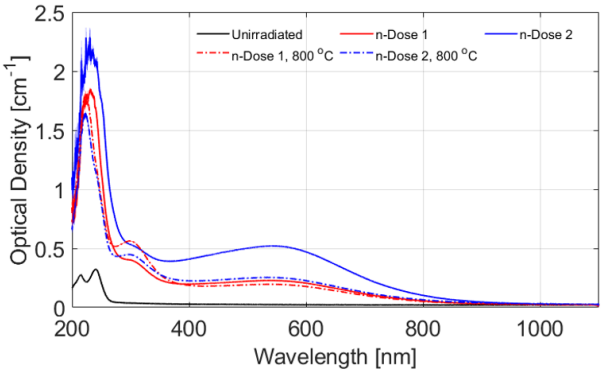

Figure 4.6: Concurrent-irradiation thermally annealed attenuation spectrum for I302 irradiated to 3.4×10^{16} n $\cdot$ cm^{-2} and 1.7×10^{17} n $\cdot$ cm^{-2}, compared to the post-irradiation attenuation spectrum for equivalent fluences.

the un-annealed n-Dose 1 spectrum, with a slightly more prominent attenuation peak centered at 300 nm compared to the un-annealed n-Dose 1 spectrum.

Figures 4.7, 4.8, and 4.9 show the sapphire attenuation spectra for the cases of gamma irradiation under concurrent-irradiation annealing, and neutron irradiation under post- and then concurrent-irradiation annealing, respectively. In Figure 4.7 the sapphire irradiated to 3.6 Mrad gamma exhibits attenuation peaks at 205 nm and 260 nm. In the same figure, the concurrent-irradiation annealed cases exhibit reduced attenuation peaks at 205 nm, consistent attenuation peaks at 260 nm, and attenuation peaks at 300 nm and 355 nm that were not present in the gamma-irradiated case without annealing.

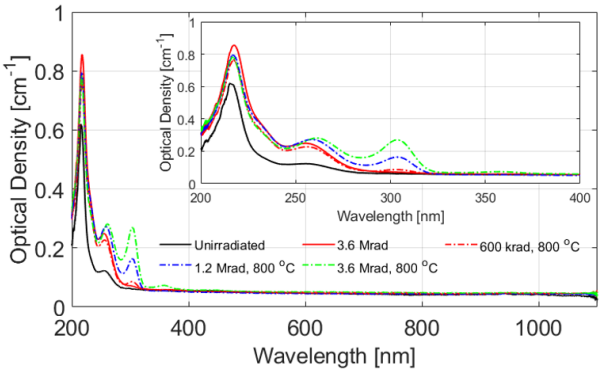

Figure 4.7: Concurrent-irradiation thermally annealed attenuation spectrum for sapphire irradiated to 600 krad, 1.2 Mrad, and 3.6 Mrad, compared to the 3.6 Mrad gamma-irradiated sample attenuation spectrum.

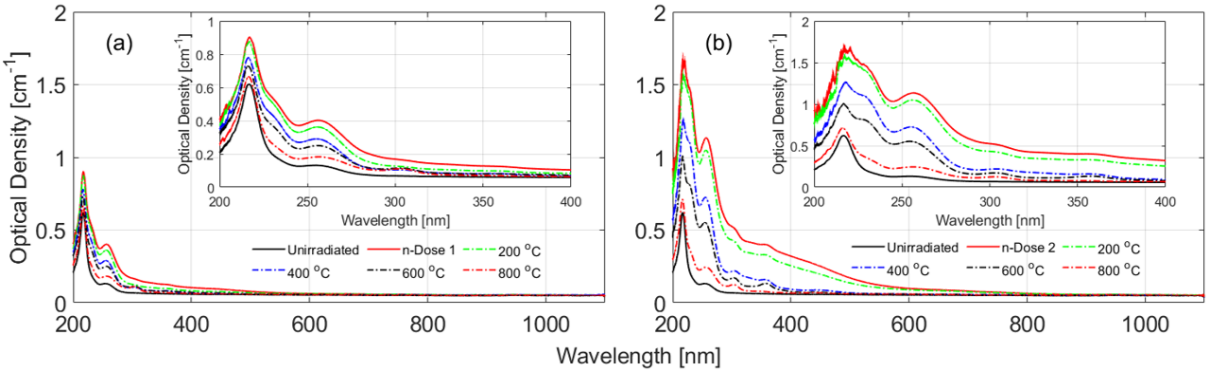

Figure 4.8: Post-irradiation thermally-annealed attenuation spectra for sapphire irradiated to (a) 3.4×10^{16} n $\cdot$ cm^{-2} (n-Dose 1) and (b) 1.7×10^{17} n $\cdot$ cm^{-2} (n-Dose 2).

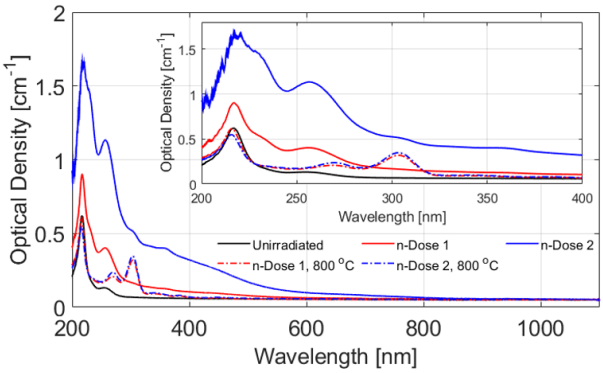

Figure 4.9: Concurrent-irradiation thermally annealed attenuation spectrum for sapphire irradiated to 3.4×10^{16} n $\cdot$ cm^{-2} and 1.7×10^{17} n $\cdot$ cm^{-2}, compared to the post-irradiation attenuation spectrum for equivalent fluences.

The attenuation spectra of neutron-irradiated sapphire in Figure 4.8 consistently show the same attenuation peaks at 205 nm and 260 nm, with a broad attenuation band extending to 800 nm. After thermally annealing to 200°C, the previously observed attenuation peaks at 300 nm and 355 nm become more prominent, in addition to another attenuation peak at 450 nm. At higher annealing temperatures, the broad attenuation band continues to decrease and the individual attenuation peaks become more prominent while also decreasing in magnitude. The neutron-irradiated sapphire attenuation spectrum for the concurrent-irradiation thermal annealing case in Figure 4.9 exhibits reduced attenuation peaks at 205 nm, 260 nm, and 355 nm, but also an increased attenuation peak at 300 nm, when compared to the n-Dose 1 attenuation spectrum.

Figure 4.10 shows the OD of all three sample types irradiated to n-Dose 2 along with Gaussian fits of the known attenuation peaks, with the associated centroids and full width at half maximum (FWHM) listed in Table 4.1 [43, 49, 63]. A generally good agreement between the features seen in measurements and the fit to the known attenuation peaks, including their centroids and widths, can be seen. Table 4.2 lists the concurrent-irradiation annealed OD peak values for all three samples for the 3.6 Mrad, and n-Dose 1 and 2 cases. This illustrates the retained RIA for each sample type under the conditions

of concurrent-irradiation thermal annealing.

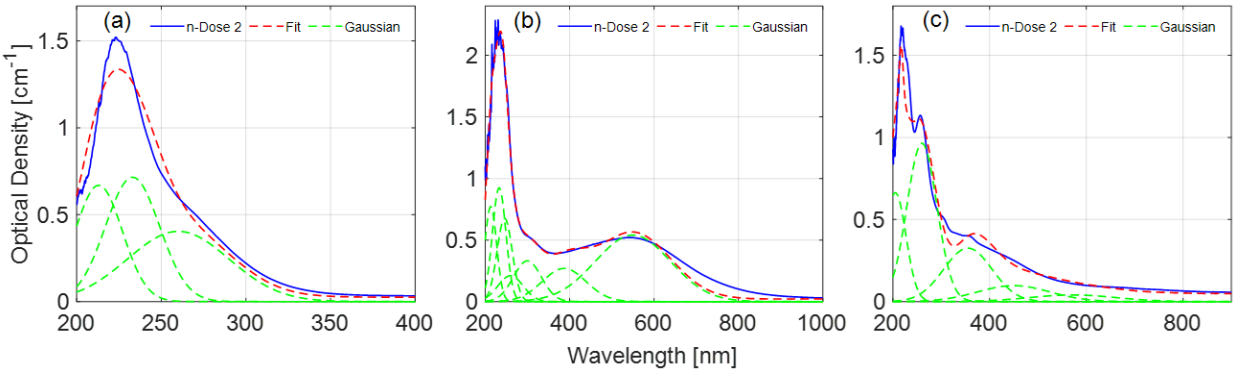

Figure 4.10: Gaussian fits (red lines) of known attenuation peaks for neutron irradiated (a) S2000, (b) I302, and (c) sapphire [43, 49, 63].

Table 4.1: Previously reported peak centroids and FWHMs for Gaussian peaks depicted in Figure 4.10.

S2000 [63]	
Centroid	FWHM
213 nm	28 nm
233 nm	32 nm
260 nm	60 nm

I302 [43, 63]	
Centroid	FWHM
213 nm	28 nm
233 nm	32 nm
246 nm	36 nm
260 nm	60 nm
300 nm	66 nm
387 nm	104 nm
550 nm	178 nm

Sapphire [43, 49, 63]	
Centroid	FWHM
205 nm	44 nm
260 nm	62 nm
300 nm	66 nm
355 nm	102 nm
450 nm	150 nm
572 nm	178 nm

Table 4.2: Concurrent-irradiation annealed OD peak values for comparison to unirradiated values to quantify the magnitude of retained RIA. All listed OD peak values are [cm^{-1}].

Peak Centroid	S2000			
	Unirradiated	3.6 Mrad, 800 °C	n-Dose 1, 800 °C	n-Dose 2, 800 °C
213 nm	0.04 ± 0.02		0.06 ± 0.01	0.08 ± 0.01
233 nm	0.04 ± 0.01		0.05 ± 0.01	0.07 ± 0.01
260 nm	0.03 ± 0.01		0.04 ± 0.01	0.07 ± 0.01
Peak Centroid	I302			
	Unirradiated	3.6 Mrad, 800 °C	n-Dose 1, 800 °C	n-Dose 2, 800 °C
213 nm	0.26 ± 0.02	0.27 ± 0.04	1.21 ± 0.04	1.29 ± 0.04
233 nm	0.26 ± 0.02	0.27 ± 0.01	1.52 ± 0.02	1.35 ± 0.01
246 nm	0.27 ± 0.01	0.28 ± 0.01	1.05 ± 0.01	1.01 ± 0.01
260 nm	0.07 ± 0.01	0.08 ± 0.01	0.62 ± 0.01	0.56 ± 0.01
300 nm	0.03 ± 0.01	0.03 ± 0.01	0.40 ± 0.01	0.45 ± 0.01
387 nm	0.02 ± 0.01	0.03 ± 0.01	0.19 ± 0.01	0.23 ± 0.01
550 nm	0.02 ± 0.01	0.03 ± 0.01	0.20 ± 0.01	0.25 ± 0.01
Peak Centroid	Sapphire			
	Unirradiated	3.6 Mrad, 800 °C	n-Dose 1, 800 °C	n-Dose 2, 800 °C
205 nm	0.29 ± 0.02	0.39 ± 0.02	0.29 ± 0.02	0.31 ± 0.02
260 nm	0.12 ± 0.01	0.28 ± 0.01	0.20 ± 0.01	0.23 ± 0.01
300 nm	0.06 ± 0.01	0.25 ± 0.01	0.30 ± 0.01	0.31 ± 0.01
355 nm	0.06 ± 0.01	0.07 ± 0.01	0.08 ± 0.01	0.09 ± 0.01
450 nm	0.05 ± 0.01	0.06 ± 0.01	0.06 ± 0.02	0.07 ± 0.02
572 nm	0.05 ± 0.01	0.05 ± 0.01	0.05 ± 0.01	0.06 ± 0.01

4.2 Discussion

The neutron-irradiated S2000 attenuation peak around 213 nm can be attributed to E' centers [1, 63] and self trapped excitons [58]. E' centers may be generated from gamma-ionization of existing precursor ODC or Si-H sites introduced into the material during manufacturing, or generated by neutron displacements of oxygen [42]. S2000 is a high-OH content fused silica and likely has a significant amount of Si-H precursors, which can be ionized to E' centers when exposed to sufficient gamma irradiation or recoil atoms from neutron interactions. Self trapped excitons optically absorb at 233 nm and may be generated from displaced oxygen [63]. There appears to be a subdued peak near 260 nm than extends the attenuation band to 350 nm in the neutron irradiated S2000 spectra. The 260-nm peak is consistent with previous work that attributes this band to ionized peroxy radical defects that form NBOHC [42]. The E' centers readily anneal possibly because of the mobility of H in fused silica, and the NBOHC have been shown to readily anneal in high-OH content, high-purity fused silica, which may explain why the S2000 sample anneals completely at 600 °C in the post-irradiation thermal annealing case [42]. This was not the case for the concurrent-irradiation annealed sample, shown in Figure 4.2, which was heated to 800 °C for the duration of irradiation. This sample exhibited a residual attenuation band at 213 nm that increases with n-Dose and indicates the competitive processes of E' center generation and thermal annealing.

With regards to the I302 sample, it is noted that the unirradiated attenuation spectrum possesses two prominent peaks at 213 nm and 246 nm. The 213-nm attenuation peak coincides with E' centers and may be present because of precursor ODC with broken silicon bonds and a trapped hole [41]. The 246-nm attenuation peak coincides with existing ODC precursors that are likely to form in low-OH content fused silica [41, 58]. The ODC precursors converted to E' centers by absorption of holes are responsible for the increased attenuation peak at 213 nm in I302 when irradiated by pure gamma irradi-

ation, as shown in Figures 4.3 and 4.4, in contrast with the lack of increased attenuation observed in S2000 for the same doses [42, 58]. The gamma-irradiated I302 in Figure 4.3 also exhibits a gamma-induced attenuation peak at 300 nm, which likely results from the generation of Al E' centers from the ionization of Al impurities [43]. I302 is a type I commercial silica glass with a lower OH content and higher concentration of metallic impurities, the most prominent being 20 ppm of Al [8]. In all gamma irradiation cases, the I302 sample is restored to its unirradiated attenuation spectrum after annealing to 800 °C, including the concurrent-irradiation annealing case as shown in Figure 4.4. The gamma-induced attenuation peak at 300 nm anneals to the unirradiated OD magnitude after annealing to 400 °C, but the gamma-enhanced attenuation peak at 213 nm does not anneal to the unirradiated OD magnitude until after annealing to 800 °C. The higher 800 °C temperature requirement to anneal and completely remove E' defects in low OH content silica, contrasted with the complete annealing of high-OH S2000 at 600 °C, has been previously observed and may be attributed to a lower concentration of diffuse molecular H species, making thermal excitation of electrons and holes the primary means of E' annealing [42].

The neutron-irradiated I302 shown in Figure 4.5 exhibited attenuation peaks at 213 nm and 300 nm, similar to the gamma-irradiated samples, but of larger magnitude. The neutron irradiation generates additional ODC which are converted to E' centers by gamma irradiation, resulting in the increased attenuation peak at 213 nm compared to the pure gamma irradiation. The gamma dose during combined neutron-gamma irradiation was over 10 times the pure gamma dose, which may explain the increased attenuation peak at 300 nm from increased Al E' center generation [43]. The neutron-irradiated I302 exhibited a broad attenuation band centered at 550 nm that may be attributed to Al precursors and the broken aluminium-oxygen bonds from gamma interactions that absorb at 387 nm and 550 nm [43, 58, 63]. The neutron-irradiated I302 annealed completely

at 800 °C for n-Dose 1, but the sample irradiated to n-Dose 2 did not completely anneal the 213-nm attenuation peak after heating to 800 °C. Also, there is a significantly larger attenuation peak remaining at 213 nm after annealing to 600 °C compared to the gamma-irradiated case. This further suggests that the low-OH content type I commercial silica requires greater temperatures and time to anneal the E' center by means of electron and hole excitation compared to high-OH type III commercial silica [42]. For the concurrent-irradiation annealed neutron-irradiated I302 (Figure 4.6), annealing in the n-Dose 1 case did not reduce the attenuation spectrum, and annealing in the n-Dose 2 case reduced the spectrum to nearly the same as the n-Dose 1 case, and the 300-nm Al E' center attenuation peak became slightly more prominent in both cases. An equilibrium may exist between the rates of thermal annealing and radiation damage that results in a nearly consistent RIA spectrum at the n-Dose 1 unannealed level, and may also mean the increased temperature enhances the generation of Al E' centers. It is noted though that the 213 nm and 300 nm peaks in the Dose-2 case are smaller in magnitude than the Dose-1 case, and additional higher dose studies are required to verify either an equilibrium state or that these RIA peaks are decreasing with longer annealing time.

Sapphire exhibited radiation damage under the condition of concurrent-irradiation thermal annealing, which is first exhibited in the case of gamma irradiation by RIA peaks at 260 nm, 300 nm, and 355 nm, and is shown in Figure 4.7. Included in this plot is the unannealed sapphire attenuation spectrum for irradiation to 3.6 Mrad. It can be seen in the figure that unannealed gamma-irradiated sapphire develops attenuation peaks at 205 nm, 260 nm, and possibly at 300 nm. Under the conditions of concurrent-irradiation thermal annealing, the 205 nm attenuation peak is slightly reduced, but the attenuation peaks at 260 nm and 300 nm actually exceed their unannealed counterparts for a lower dose of 1.2 Mrad, and at 3.6 Mrad concurrent-irradiation thermal annealing an attenuation peak develops at 355 nm. The peak at 205 nm can be attributed to F centers, at

260 nm to F^+ centers, at 300 nm to F_2 centers, and at 355 nm to F_2^+ centers [51, 64]. This result may indicate a strong temperature dependence for RIA growth in existing sapphire oxygen vacancy and divacancy sites from gamma-radiation-induced-ionization, electron-hole recombination, and increased vacancy center mobility, similar to the temperature dependence of damage efficiency in alumina from neutron bombardment [48].

The neutron-irradiated sapphire with post-irradiation annealing exhibits RIA peaks at 205 nm, 260 nm, 300 nm, 355 nm, 450 nm, and 572 nm, consistent with previous studies, with the 450 nm peak attributed to F_2^{2+} centers and the 572 nm peak attributed to Al-oxygen-hole-centers [43, 50]. Furthermore, the neutron irradiated sapphire anneals almost entirely to the unirradiated state at 800 °C and could anneal entirely if heated to 900 °C according to previous studies [49]. It is also significant to note that the unannealed sapphire attenuation peaks form a continuous attenuation band that extends to 800 nm after irradiation, and that this band quickly dissipates and develops into individual attenuation peaks with annealing near 400 °C. The neutron-irradiated sapphire under concurrent-irradiation thermal annealing shown in Figure 4.9 exhibits reduced 205 nm, 260 nm, 355 nm, and 450 nm attenuation peaks consistent with the neutron-irradiated case after thermal annealing, but also a significantly enhanced 300-nm attenuation peak that is not consistent with the post-irradiation thermally annealed case. There may be a temperature dependence that favors either the generation of F_2 centers from increased mobility combination of F centers, or the conversion of F_2^+ centers into F_2 centers by electron attenuation from F center donors, which would account for the reduced peaks at 205 nm and 260 nm and the residual peak at 300 nm.

Chapter 5

Effect of Radiation on Nonlinear Properties of Optical Materials

The significant result of Z-scan examination of irradiated optical materials is the observation of a negative NLA coefficient in all of the materials examined. The effect is first observed in gamma-irradiated I302, and then in all of the materials under mixed neutron and gamma irradiation due to higher doses. A negative NLR coefficient was also observed in BK7G18. Post-irradiation thermal annealing is shown to restore the optical materials to the unirradiated state, but concurrent-irradiation thermal annealing does not restore the optical material in all cases.

5.1 Gamma-Induced Negative Nonlinear Absorption in Quartz Glass

The NLA of I302 optical quartz glass was measured before irradiation and following gamma irradiations to 600 krad, 1.2 Mrad, 3.6 Mrad, and 10 Mrad. It was then measured again after each thermal annealing step, as described in Chapter 3. Figure 5.1 shows the Z-scan NLA curves measured for quartz glass before irradiation and immediately

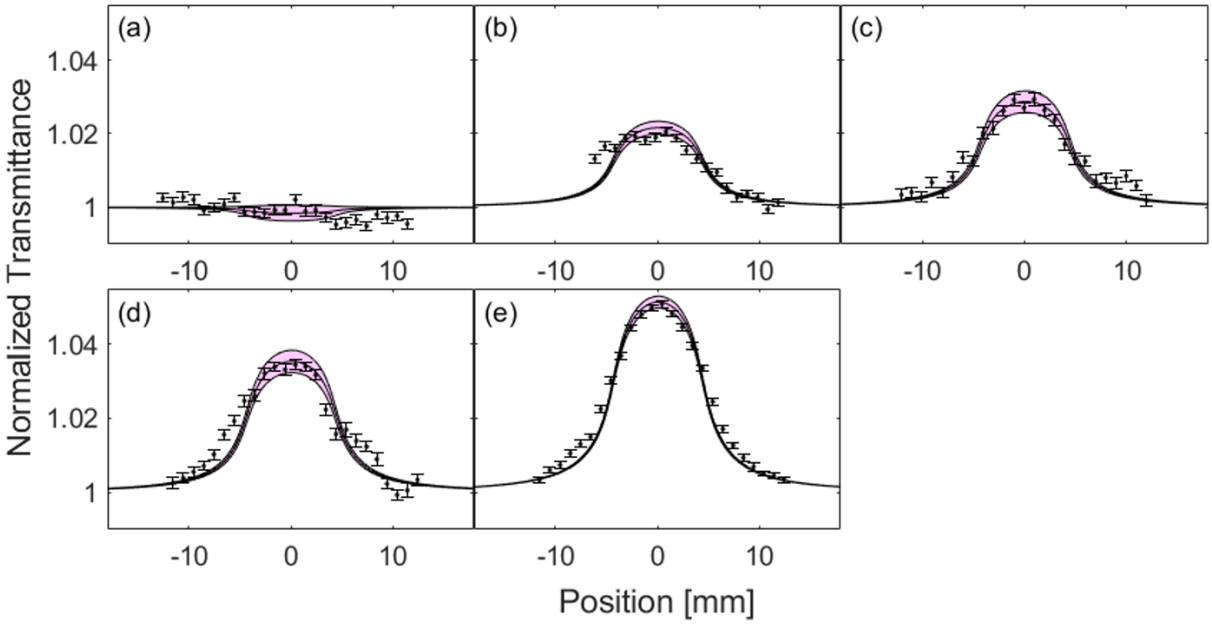

Figure 5.1: Open-aperture Z-scan measurements of I302 (a) unirradiated, (b) 600 krad, (c) 1.2 Mrad, (d) 3.6 Mrad, and (e) 10 Mrad gamma irradiation doses.

after each of the four gamma irradiations. The unirradiated NLA coefficient of quartz glass is 5×10^{-15} m/W, which is too small for our system to detect [7]. A negative NLA coefficient is measured following all four irradiations, and its magnitude increases with dose. The negative NLA coefficient persists after annealing to 200 °C, as seen in Figure 5.2. The sample exhibited its pre-irradiation NLA after annealing to 400 °C. Two I302 samples were used throughout these measurements. The first sample was irradiated to 600 krad, and the results are presented in Figures 5.1(b) and 5.2(a). A second I302 sample from the same batch was used for the 1.2 Mrad, 3.6 Mrad, and 10 Mrad irradiations with post-irradiation thermal annealing. The use of two I302 samples from the same batch demonstrates repeatable radiation-induced negative nonlinearity across multiple I302 samples from the same batch. The second I302 sample used also shows that the nonlinearity can be induced by repeated irradiation following the thermal annealing.

Table 5.1 provides the measured β values for each gamma irradiation dose post-

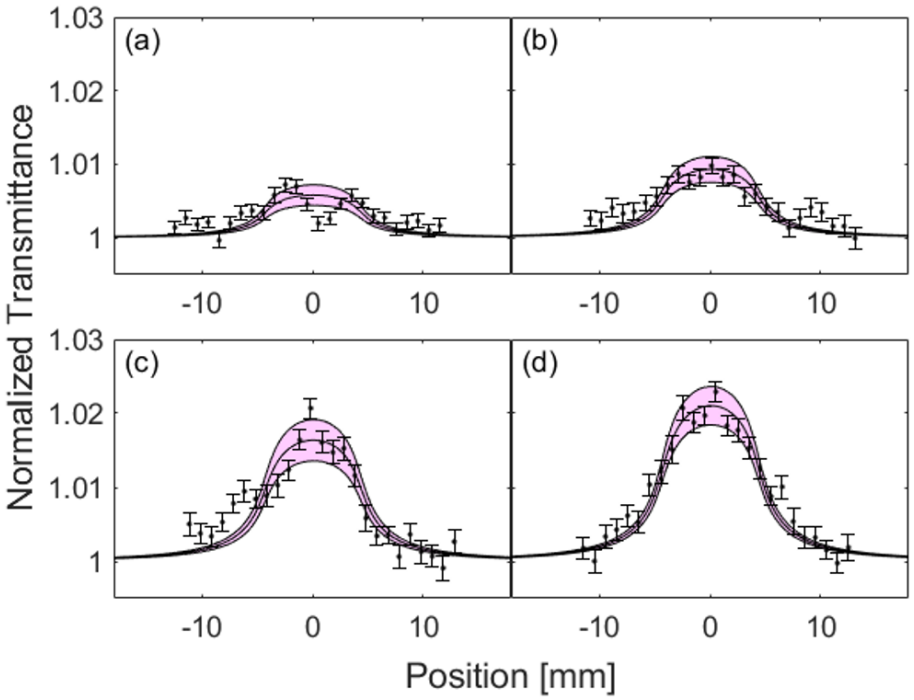

Figure 5.2: Open-aperture Z-scan measurements of I302 thermally annealed to 200 °C after (a) 600 krad, (b) 1.2 Mrad, (c) 3.6 Mrad, and (d) 10 Mrad gamma irradiation doses.

Table 5.1: Gamma irradiated I302 nonlinear absorption coefficient β [$\times$ 10^{-13} m·W^{-1}].

Gamma Dose	600 krad	1.2 Mrad	3.6 Mrad	10 Mrad
β: unannealed	-0.78 ± 0.06	-1.14 ± 0.12	-1.29 ± 0.11	-1.88 ± 0.06
β: annealed 200°C	-0.21 ± 0.05	-0.37 ± 0.07	-0.61 ± 0.10	-0.76 ± 0.09

irradiation and after thermal annealing at 200 °C. The negative NLA effect, which may be attributed to SA, increases in magnitude in Figure 5.1 as the gamma dose increases. The increasing contribution of SA and resultant increased transmission through the sample with increasing gamma dose corresponds to an increasing absolute value of negative nonlinearity, as shown in Table 5.1. The change in the NLA coefficient is nonlinear with increasing gamma dose and suggests the approach to a limit of the SA effect with increasing gamma dose.

Figure 5.2 shows the same irradiated I302 NLA measurements as Figure 5.1 after annealing to 200 °C for 30 minutes. The increased transmission attributed to the negative

NLA coefficient is shown to decrease with thermal annealing in all four cases. The NLA is returned to the unirradiated state after annealing the samples to 400 °C for 30 minutes. The change of the NLA coefficient with dose immediately after irradiation and after annealing to 200 °C for the four gamma doses is plotted in Figure 5.3. In this plot the error bars represent the propagated error of the least squares fit used to calculate the NLA coefficient. This plot further illustrates the nonlinear relationship between the increasing gamma dose and the NLA.

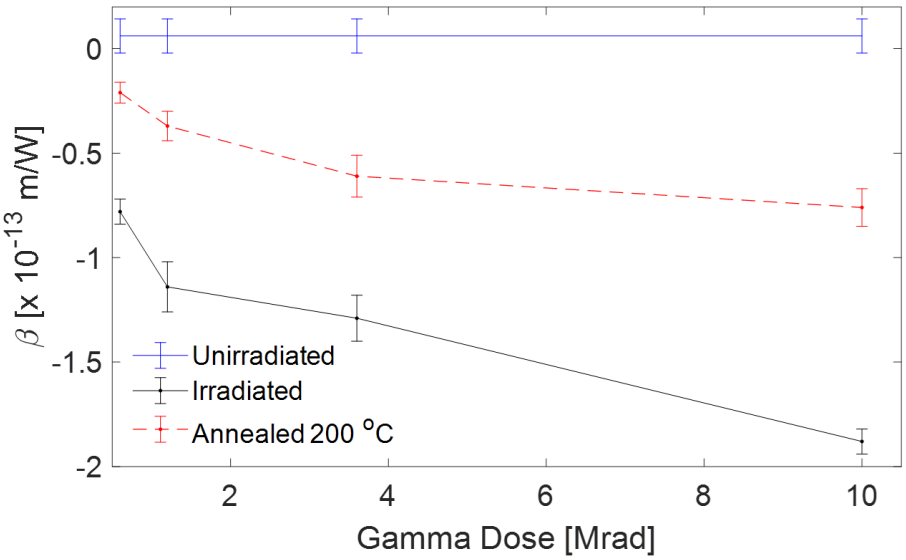

Figure 5.3: Evolution of the I302 NLA coefficient β with gamma dose and thermal annealing.

The 600 krad, 1.2 Mrad, and 3.6 Mrad gamma irradiations were repeated for I302 with concurrent-irradiation thermal annealing at 800 °C for the duration of the irradiation, and the Z-scan measurements of NLA for these irradiations are presented in Figure 5.4. It can be seen that concurrent-irradiation thermal annealing maintained the I302 NLA at its unirradiated state when compared to the plot in Figure 5.1(a). Figure 5.5 shows the post-irradiation Z-scan measurements of S2000, equivalent to the measurements for I302 in Figure 5.1, except for the 10 Mrad case. This figure shows that for the same irradiations, the NLA coefficient of S2000 remained unchanged and is discussed further

in the conclusion section.

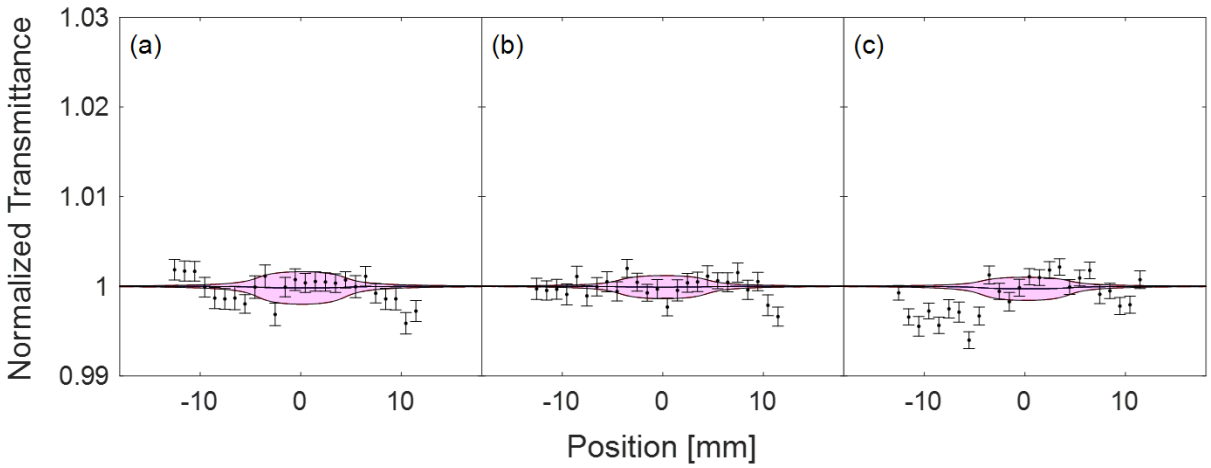

Figure 5.4: Open-aperture Z-scan measurements of I302 concurrent-irradiation thermally annealed at 800 °C after (a) 600 krad, (b) 1.2 Mrad, and (c) 3.6 Mrad gamma irradiation doses.

The linear attenuation spectrum between 200 nm and 1100 nm for I302 quartz glass irradiated to 3.6 Mrad and annealed at temperatures of up to 800 °C is presented in Figure 4.3(c) for comparison with the measurements of NLA. The expected attenuation bands are observed at 213 nm and 300 nm, consistent with gamma irradiation E' defect generation [58] and generation of Al impurity E' centers, respectively [43]. The radiation-induced linear attenuation is shown to reduce to the unirradiated state after annealing to 800 °C. The linear transmission observed at 532 nm is consistent with the sample manufacturer's listed transmission within ±1.5% and decreases by 2% after irradiation to 3.6 Mrad. The unirradiated linear transmission of 91% and irradiated minimum linear transmission of 89% at 532 nm are sufficient to allow for the observed magnitude of SA-induced increase in transmission of up to 5% shown in Figure 5.1.

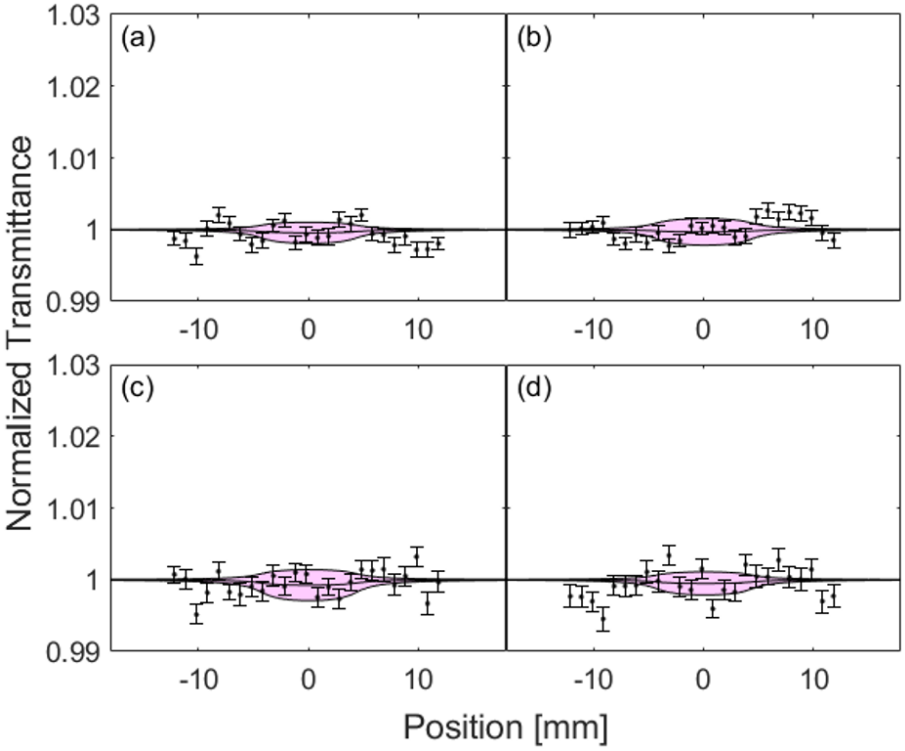

Figure 5.5: Open-aperture Z-scan measurements of S2000 (a) unirradiated, (b) 600 krad, (c) 1.2 Mrad, and (d) 3.6 Mrad gamma irradiation doses

5.2 Neutron- and Gamma-Induced Negative Nonlinearity

The reactor irradiations produced negative NLA effects in all of the optical materials due to exposure to greater gamma dose rates, in addition to neutrons, than the ^{60}Co irradiations, as listed in Table 3.1. Figures 5.6, 5.7, and 5.8 show the results of NLA measurements for n-Dose 1 and 2, with post- and concurrent-irradiation thermal annealing, for S2000, I302, and sapphire, respectively. In all plots the unirradiated Z-scan measurement is included for comparison. All three samples annealed to the unirradiated state after heating to 400 °C for 30 minutes except I302, which after n-Dose 2 required heating to 600 °C. In all three of these cases, annealing at 400 °C had the most significant effect in restoring the material's optical properties to the unirradiated state. Annealing at 200 °C had a marginal effect in reducing the negative nonlinearity. The opposite of this trend is observed later in the borosilicate glass samples. Finally, concurrent-irradiation thermal annealing at 800 °C maintained S2000 and sapphire at the unirradiated NLA state, but I302 accumulated radiation effects during concurrent-thermal annealing resulting in a negative NLA coefficient, evident in Figures 5.7(c) and 5.7(d).

Figure 5.9 shows the results of post-irradiation thermally annealed NLA measurements for NBK7 glass. The majority of thermal annealing occurs when heating the sample to 200 °C, and the sample fully anneals at 400 °C. NBK7 exhibited the greatest magnitude of negative NLA, which appears correlated with the high opacity of NBK7 after irradiation, as seen in Figure 3.4. NBK7, and to a lesser degree BK7G18, sapphire, and I302, exhibited potential photobleaching. This was apparent when performing multiple Z-scans on the same spot of an irradiated sample and obtaining increasing transmission peak magnitudes in each subsequent Z-scan. Examples of photobleaching observed post irradiation to n-Dose 1 and n-Dose 2 for these materials are presented in Figures 5.13, 5.14, 5.15, and 5.16,

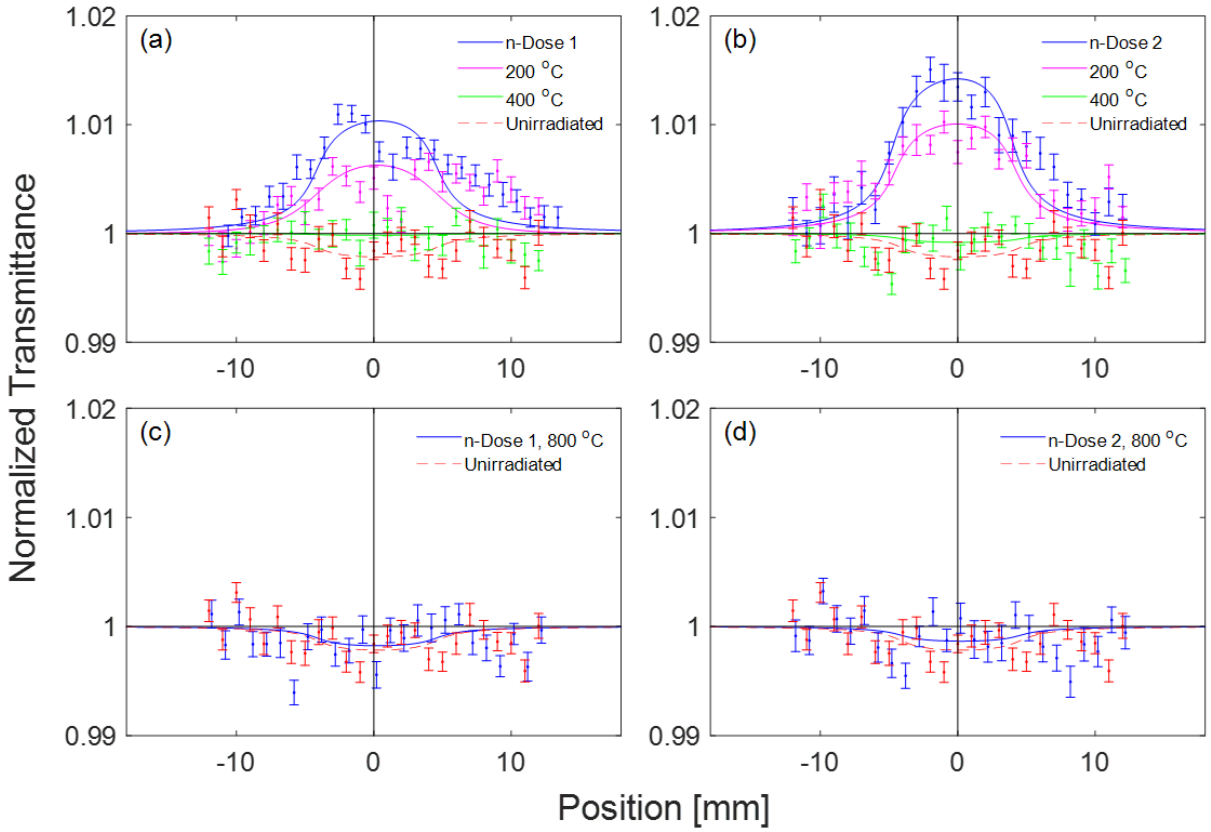

Figure 5.6: NLA measurements of S2000 after (a) irradiation to n-Dose 1 and post-irradiation thermal annealing through 400 °C, (b) irradiation to n-Dose 2 and post-irradiation thermal annealing through 400 °C, (c) irradiation to n-Dose 1 with concurrent-irradiation thermal annealing at 800 °C, and (d) irradiation to n-Dose 2 with concurrent-irradiation thermal annealing at 800 °C.

with the coefficient values for each scan provided in Table 5.3. This was tested in NBK7 irradiated to n-Dose 2 and is shown in Figure 5.11. During this test the irradiated NBK7 sample was moved to the position of maximum transmission (0 mm position) and the laser was pulsed continuously through the sample at the same location within the sample. Measurements of the open aperture and reference photodiodes were taken at periodic time intervals over 3 hours; the ratio of the open aperture to reference diode with a power fit are plotted in Figure 5.11. It can be seen that over time the photobleaching effect decreases and has a tendency to eventually plateau.

BK7G18 similarly exhibited a negative NLA coefficient that annealed after heating

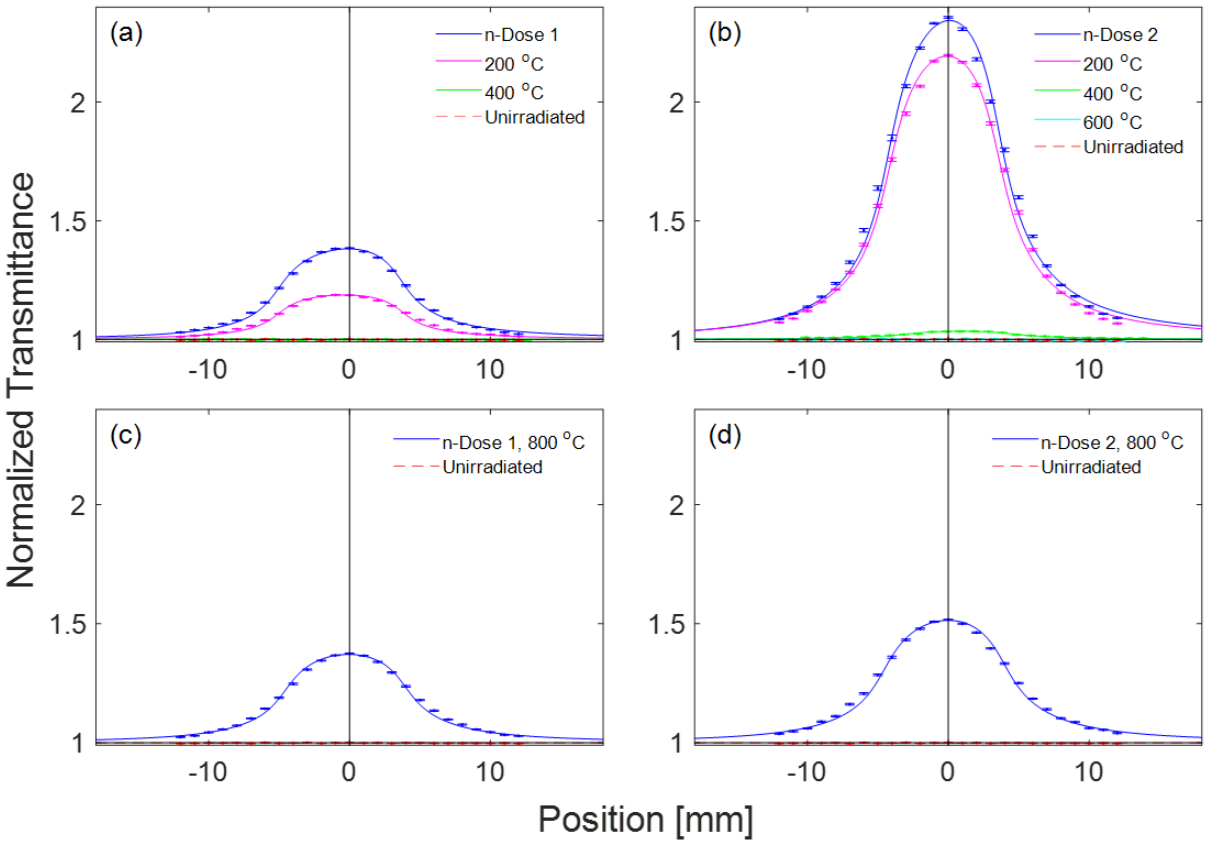

Figure 5.7: NLA measurements of I302 after (a) irradiation to n-Dose 1 and post-irradiation thermal annealing through 400 °C, (b) irradiation to n-Dose 2 and post-irradiation thermal annealing through 400 °C, (c) irradiation to n-Dose 1 with concurrent-irradiation thermal annealing at 800 °C, and (d) irradiation to n-Dose 2 with concurrent-irradiation thermal annealing at 800 °C.

to 400 °C, shown in Figures 5.10(a) and 5.10(b). BK7G18 also exhibited a negative NLR index that had a consistent and estimable form, shown in Figures 5.10(c) and 5.10(d) with fit lines. The unirradiated and 400 °C annealed NLR curves were not discernable, possibly due to darkening that has been observed during Z-scans in some BK7 samples [15]. The irradiated curves, however, were very symmetric and consistent, and a NLR index was extracted from these. It is also observed that after annealing to 400 °C the NLR curves have more significant decreases in transmission than the unirradiated curves, which may be due to the previously noted darkening enhanced by irradiation.

Table 5.2 lists the NLA and NLR coefficients measured for irradiated and thermally

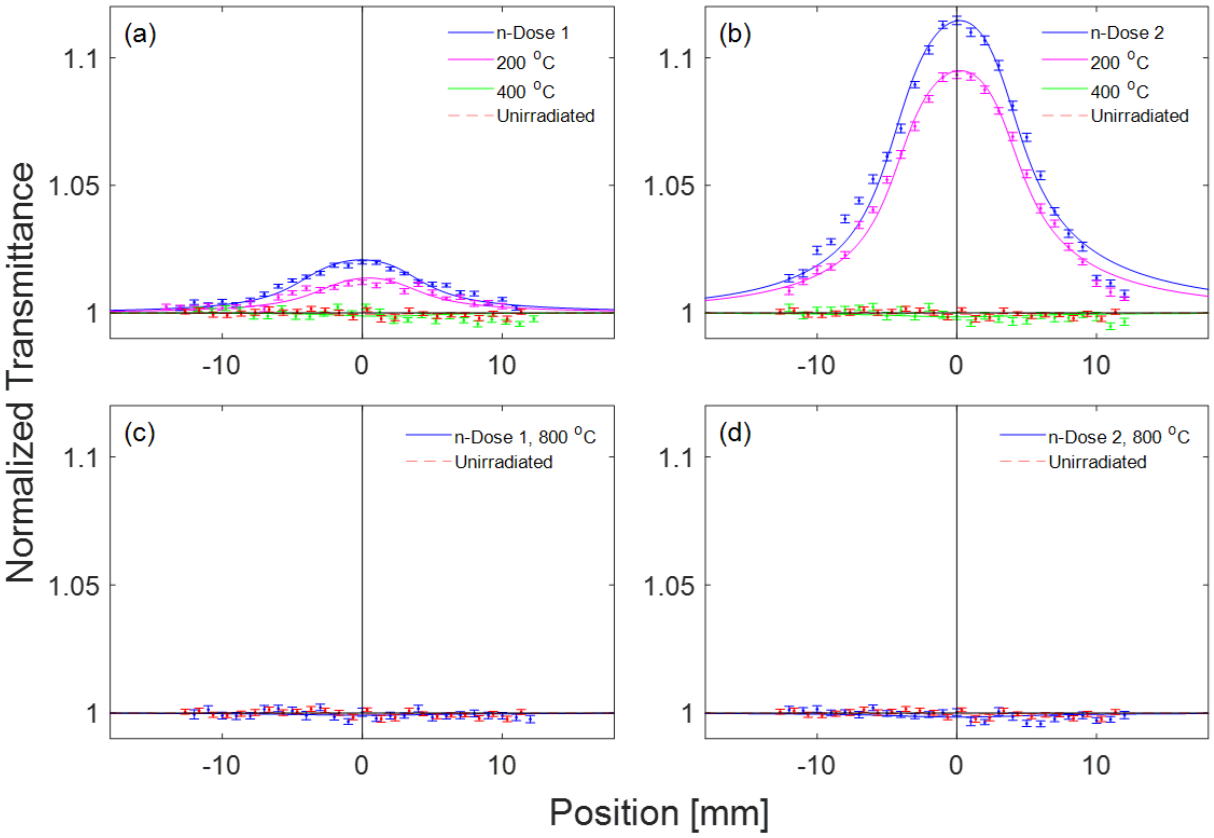

Figure 5.8: NLA measurements of sapphire after (a) irradiation to n-Dose 1 and post-irradiation thermal annealing through 400 °C, (b) irradiation to n-Dose 2 and post-irradiation thermal annealing through 400 °C, (c) irradiation to n-Dose 1 with concurrent-irradiation thermal annealing at 800 °C, and (d) irradiation to n-Dose 2 with concurrent-irradiation thermal annealing at 800 °C.

annealed samples. The unirradiated NLA coefficients are obtained from literature and are used to calibrate the Z-scan using an NBK7 sample [7, 35]. Irradiated n_2 values are omitted for all samples except BK7G18 because the irradiated closed aperture Z-scans were inconsistent and the nonlinear index of refraction was not able to be determined by simulation fitting. Attempts were made to determine n_2 by dividing the closed aperture measurement by the open aperture measurement to obtain an accurate NLR estimate in the presence of NLA, but were not successful [13]. Concurrent-irradiation thermal annealing NLA coefficient values for borosilicate glass samples are omitted because, as mentioned in the experiment section, the melting point of borosilicate glass precluded it

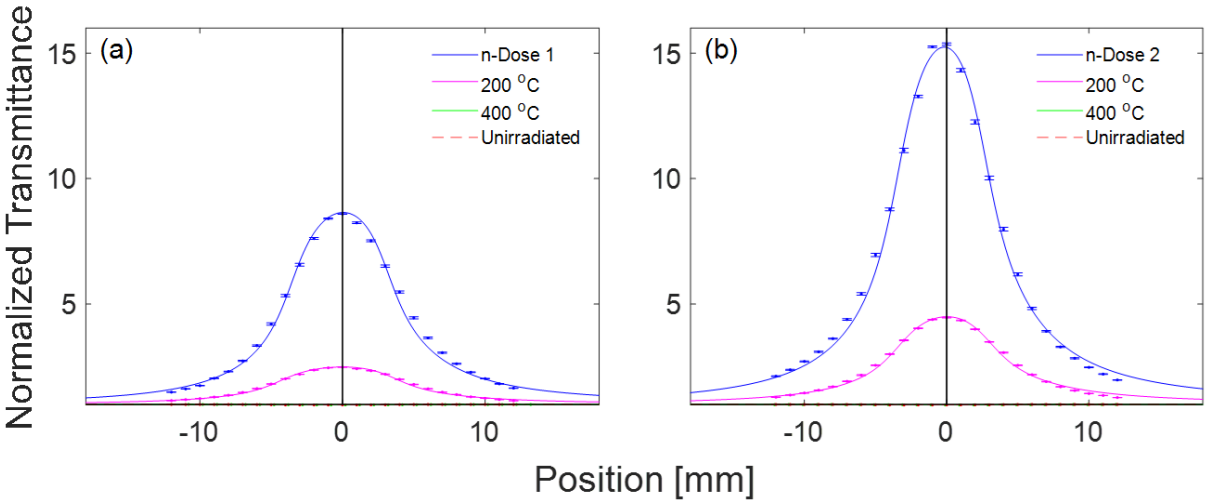

Figure 5.9: NLA measurements of NBK7 after (a) irradiation to n-Dose 1 and post-irradiation thermal annealing through 400 °C and (b) irradiation to n-Dose 2 and post-irradiation thermal annealing through 400 °C.

from being thermally annealed to 800 °C. Finally, only I302 has an NLA coefficient listed for n-Dose 2 thermally annealed to 600 °C because all of the other samples annealed to the unirradiated state at 400 °C.

Table 5.2: Z-scan measured nonlinear coefficient values. The unirradiated values are from literature [7].

Nonlinearity	n-Dose Anneal Temperature	Optical Sample				
		S2000	I302	Sapphire	NBK7	BK7G18
β [m·W^{-1}]	Unirradiated	$(< 5) \times 10^{-15}$	$(< 5) \times 10^{-15}$	$(< 1.6) \times 10^{-14}$	$(2.8) \times 10^{-14}$	$(2.8) \times 10^{-14}$
β [m·W^{-1}] Post-irradiation Annealing	n-Dose 1	$(-1.96 \pm 0.31) \times 10^{-14}$	$(-1.21 \pm 0.01) \times 10^{-12}$	$(-4.04 \pm 0.20) \times 10^{-14}$	$(-1.01 \pm 0.02) \times 10^{-11}$	$(-1.86 \pm 0.27) \times 10^{-14}$
	n-Dose 1 200 °C	$(-7.01 \pm 1.20) \times 10^{-15}$	$(-7.61 \pm 0.07) \times 10^{-13}$	$(-2.37 \pm 0.21) \times 10^{-14}$	$(-1.67 \pm 0.05) \times 10^{-12}$	$(1.53 \pm 0.32) \times 10^{-14}$
	n-Dose 1 400 °C	$(2.50 \pm 2.31) \times 10^{-15}$	$(5.16 \pm 4.40) \times 10^{-15}$	$(2.50 \pm 3.86) \times 10^{-15}$	$(2.91 \pm 0.30) \times 10^{-14}$	$(2.86 \pm 0.25) \times 10^{-14}$
	n-Dose 2	$(-2.33 \pm 0.32) \times 10^{-14}$	$(-5.01 \pm 0.02) \times 10^{-12}$	$(-1.74 \pm 0.04) \times 10^{-13}$	$(-1.99 \pm 0.05) \times 10^{-11}$	$(-5.77 \pm 0.27) \times 10^{-14}$
	n-Dose 2 200 °C	$(-1.55 \pm 0.21) \times 10^{-14}$	$(-4.48 \pm 0.02) \times 10^{-12}$	$(-1.47 \pm 0.04) \times 10^{-13}$	$(-4.41 \pm 0.02) \times 10^{-12}$	$(-1.23 \pm 0.24) \times 10^{-14}$
	n-Dose 2 400 °C	$(1.20 \pm 2.50) \times 10^{-15}$	$(-9.17 \pm 0.55) \times 10^{-14}$	$(1.99 \pm 2.62) \times 10^{-15}$	$(2.84 \pm 0.31) \times 10^{-14}$	$(2.66 \pm 0.51) \times 10^{-14}$
	n-Dose 2 600 °C	-	$(2.85 \pm 6.33) \times 10^{-15}$	-	-	-
β [m·W^{-1}] Concurrent-irradiation Annealing	n-Dose 1 800 °C	$(2.66 \pm 3.41) \times 10^{-15}$	$(-1.27 \pm 0.02) \times 10^{-12}$	$(1.15 \pm 1.85) \times 10^{-15}$	-	-
	n-Dose 2 800 °C	$(2.03 \pm 3.21) \times 10^{-15}$	$(-1.98 \pm 0.01) \times 10^{-12}$	$(2.25 \pm 2.54) \times 10^{-15}$	-	-
n_2 [m^2·W^{-1}] Post-irradiation Annealing	n-Dose 1	-	-	-	-	$(-1.70 \pm 0.04) \times 10^{-19}$
	n-Dose 1 200 °C	-	-	-	-	$(-1.67 \pm 0.03) \times 10^{-19}$
	n-Dose 2	-	-	-	-	$(-3.13 \pm 0.02) \times 10^{-19}$
	n-Dose 2 200 °C	-	-	-	-	$(-2.91 \pm 0.02) \times 10^{-19}$

Table 5.3: Z-scan post-irradiation measured nonlinear coefficient values for 3 consecutive Z-scans to test photobleaching effect.

Nonlinearity	n-Dose Scan #	Optical Sample			
		I302	Sapphire	NBK7	BK7G18
β [m·W^{-1}] Post-irradiation	n-Dose 1 Scan 1	$(-8.27 \pm 0.01) \times 10^{-13}$	$(-3.20 \pm 0.25) \times 10^{-14}$	$(-9.26 \pm 0.04) \times 10^{-12}$	$(-2.58 \pm 0.29) \times 10^{-14}$
	n-Dose 1 Scan 2	$(-1.05 \pm 0.01) \times 10^{-12}$	$(-3.52 \pm 0.20) \times 10^{-14}$	$(-1.00 \pm 0.03) \times 10^{-11}$	$(-2.44 \pm 0.30) \times 10^{-14}$
	n-Dose 1 Scan 3	$(-1.21 \pm 0.01) \times 10^{-12}$	$(-4.04 \pm 0.20) \times 10^{-14}$	$(-1.01 \pm 0.02) \times 10^{-11}$	$(-1.86 \pm 0.27) \times 10^{-14}$
	n-Dose 2 Scan 1	$(-4.35 \pm 0.02) \times 10^{-12}$	$(-1.58 \pm 0.03) \times 10^{-13}$	$(-1.94 \pm 0.01) \times 10^{-11}$	$(-5.84 \pm 0.26) \times 10^{-14}$
	n-Dose 2 Scan 2	$(-4.54 \pm 0.02) \times 10^{-12}$	$(-1.66 \pm 0.03) \times 10^{-13}$	$(-1.95 \pm 0.06) \times 10^{-11}$	$(-5.71 \pm 0.33) \times 10^{-14}$
	n-Dose 2 Scan 3	$(-5.01 \pm 0.02) \times 10^{-12}$	$(-1.74 \pm 0.04) \times 10^{-13}$	$(-1.99 \pm 0.05) \times 10^{-11}$	$(-5.77 \pm 0.27) \times 10^{-14}$
n_2 [m^2·W^{-1}] Post-irradiation	n-Dose 1 Scan 1				
	n-Dose 1 Scan 2				$(-1.08 \pm 0.03) \times 10^{-19}$
	n-Dose 1 Scan 3				$(-1.70 \pm 0.04) \times 10^{-19}$
	n-Dose 2 Scan 1				$(-2.05 \pm 0.02) \times 10^{-19}$
	n-Dose 2 Scan 2				$(-2.39 \pm 0.02) \times 10^{-19}$
	n-Dose 2 Scan 3				$(-3.13 \pm 0.02) \times 10^{-19}$

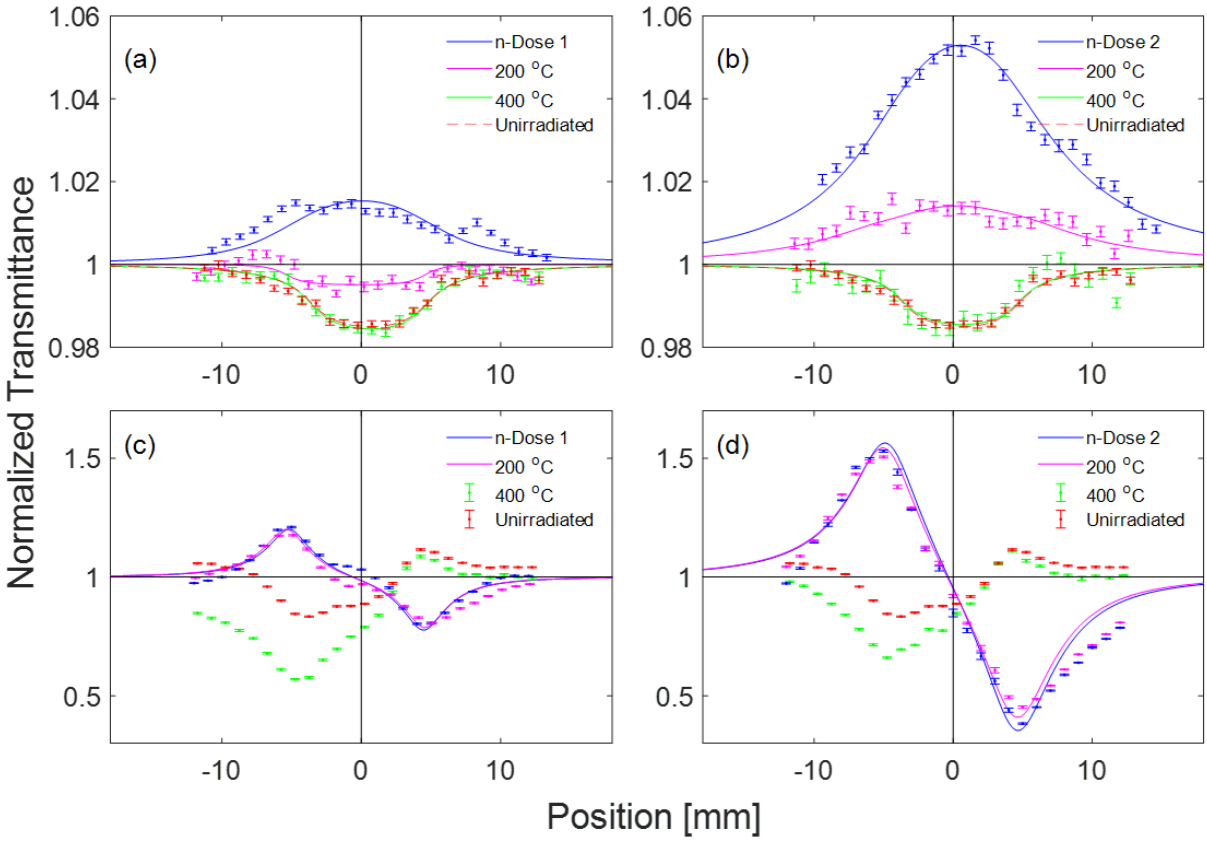

Figure 5.10: NLA measurements of BK7G18 after irradiation to (a) n-Dose 1 and (b) n-Dose 2, both with post-irradiation thermal annealing through 400 °C, and the corresponding NLR measurements of BK7G18 after irradiation to (c) n-Dose 1 and (d) n-Dose 2 both with post-irradiation thermal annealing through 400 °C.

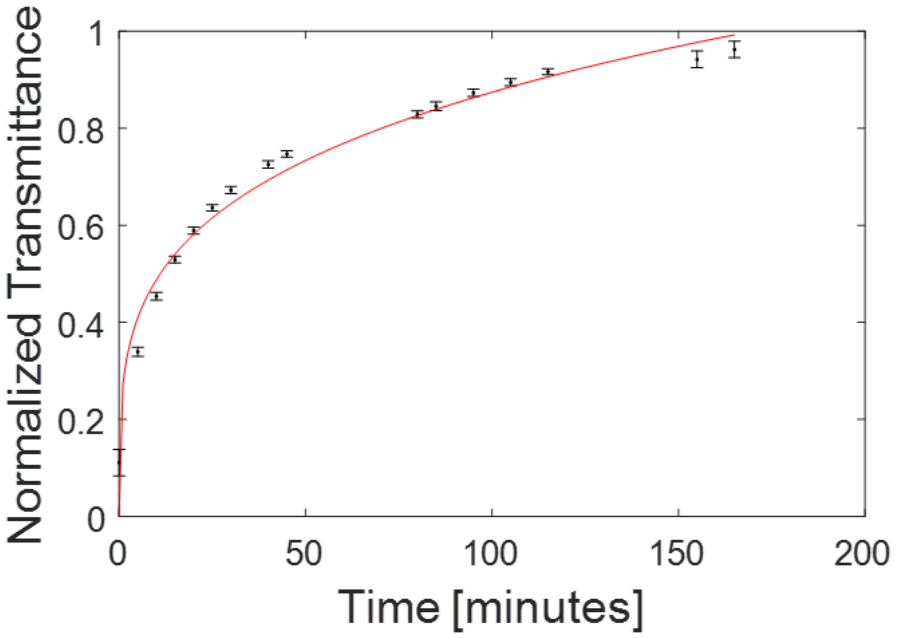

Figure 5.11: Photobleaching test of NBK7 sample irradiated to n-Dose 2. The sample is moved to the position of maximum transmitted intensity (0 mm position) and the laser is pulsed continuously at a repetition rate of 10 Hz. At each time interval identified in the plot 120 pulses are recorded and the ratio of power transmitted to the open aperture photodiode and to the reference photodiode is plotted with a power fit (red).

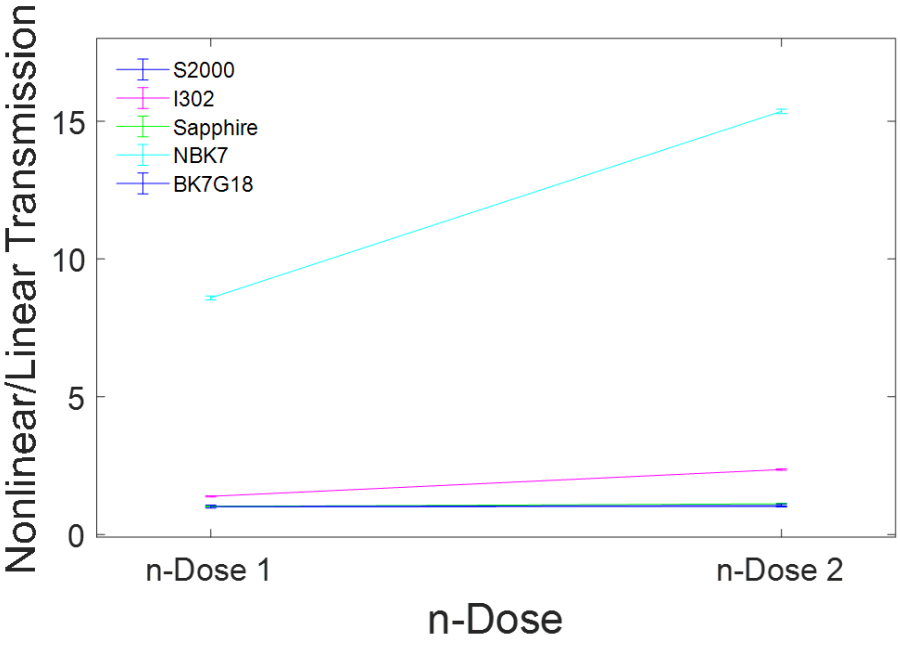

Figure 5.12: Comparison of the 532 nm radiation induced nonlinear transmission and linear transmission after n-Dose 1 and 2 for S2000, I302, Sapphire, NBK7, and BK7G18.

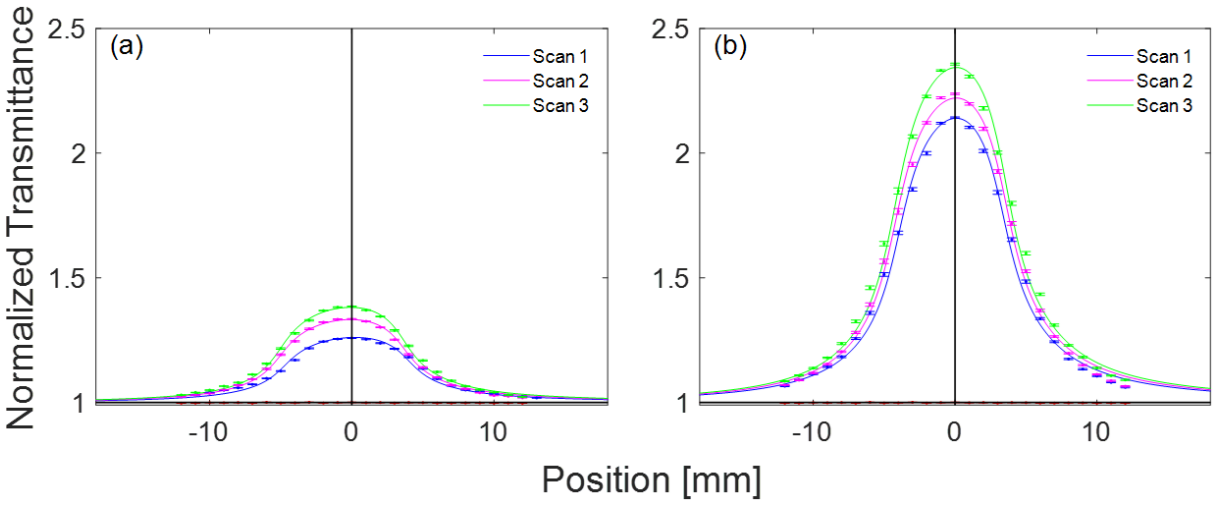

Figure 5.13: Three consecutive NLA Z-scans of I302 at the same location in the sample after irradiation to (a) n-Dose 1 and (b) n-Dose 2, performed to test the photobleaching effect.

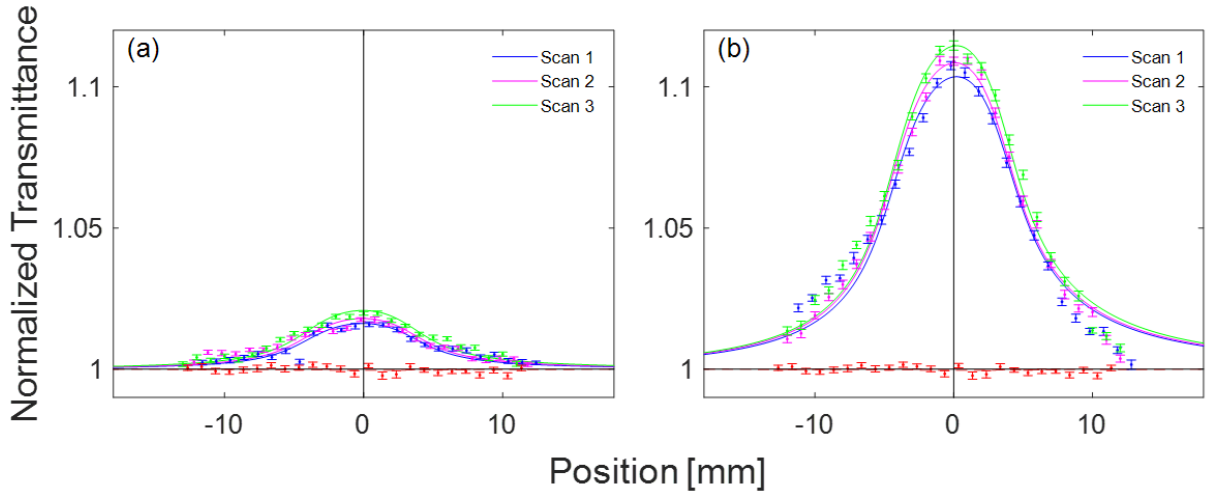

Figure 5.14: Three consecutive NLA Z-scans of Sapphire at the same location in the sample after irradiation to (a) n-Dose 1 and (b) n-Dose 2, performed to test the photobleaching effect.

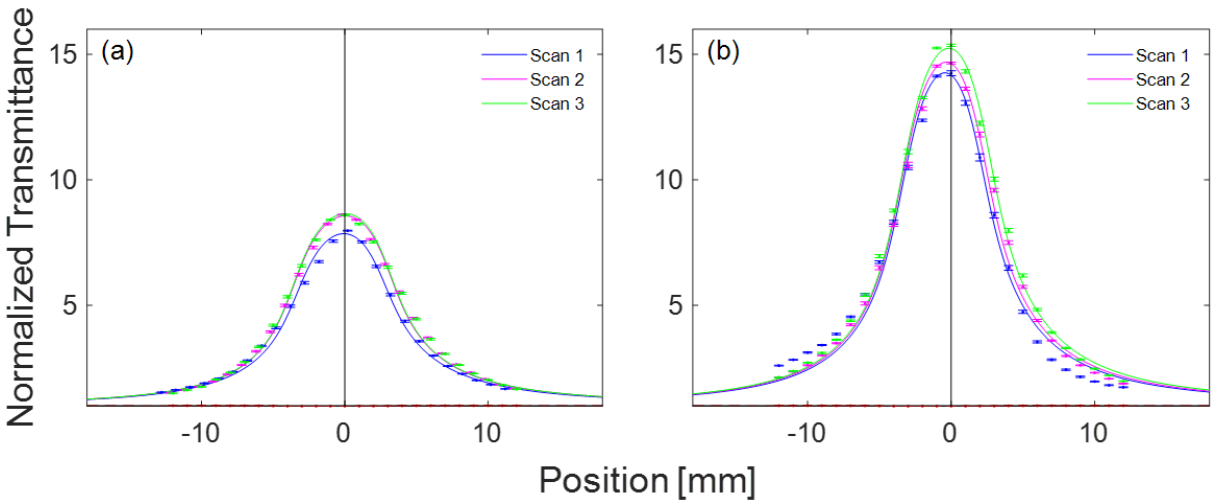

Figure 5.15: Three consecutive NLA Z-scans of NBK7 at the same location in the sample after irradiation to (a) n-Dose 1 and (b) n-Dose 2, performed to test the photobleaching effect.

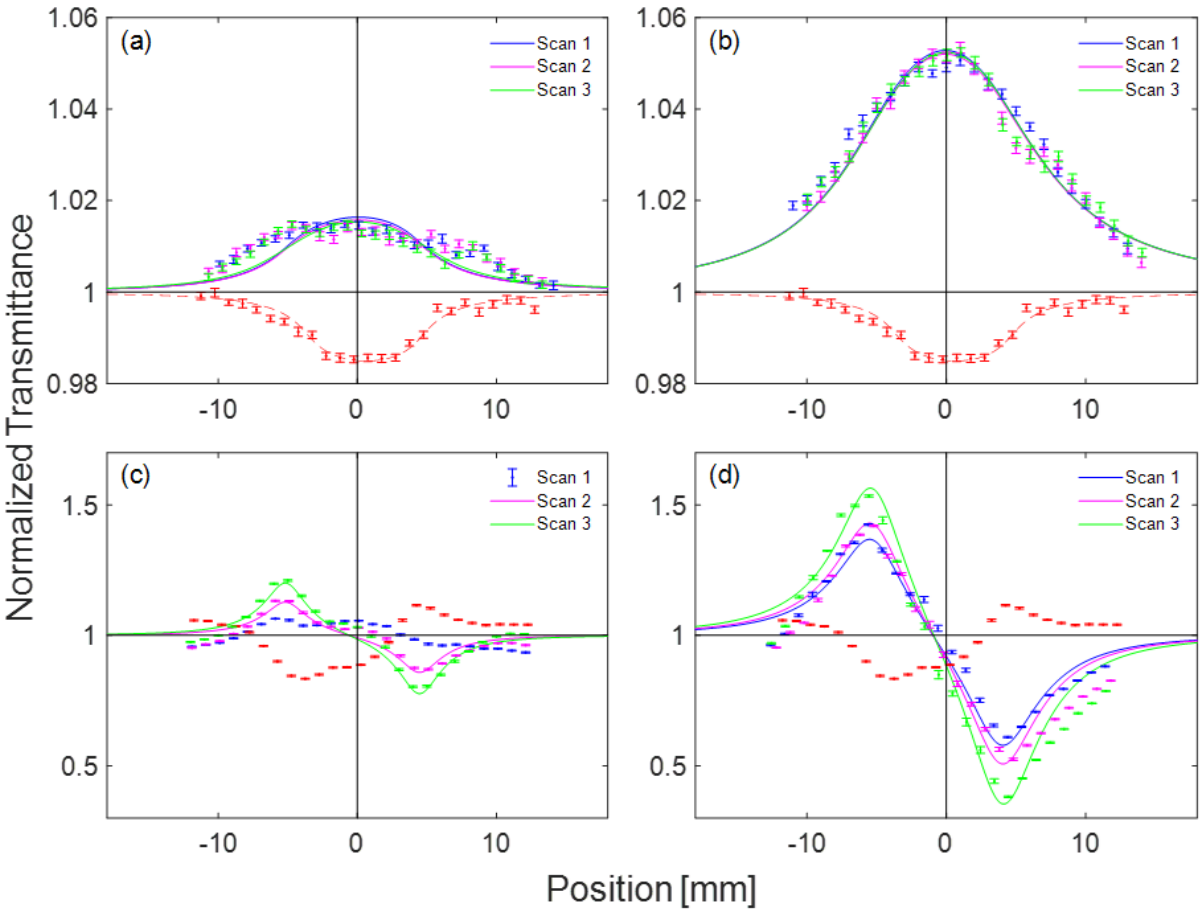

Figure 5.16: Three consecutive NLA Z-scans of BK7G18 at the same location in the sample after irradiation to (a) n-Dose 1 and (b) n-Dose 2, performed to test the photobleaching effect. The corresponding three NLR Z-scans are provided in (c) and (d).

5.3 Discussion

The gamma induced negative NLA observed in I302 and described in Section 5.1 is attributable to the SA effect. Thermal annealing reduces the SA effect, ultimately restoring the gamma irradiated quartz glass nonlinear optical properties to the unirradiated state at a temperature of 400 °C. SA is not typically observed in bulk optical materials, and understanding the relationship between SA and gamma dose in optical quartz glass is important for intense laser applications in radioactive environments. As previously described, I302 is a type I commercial silica glass manufactured by the electric melting of natural quartz crystal in vacuum or an inert gas at low pressure [8]. This process results in the presence of metallic impurities in the crystalline optical quartz glass. Heraeus S2000, a type III synthetic fused silica manufactured by the hydorlyzation of $SiCl_4$ sprayed into an OH flame, is much purer than type I silica glass but has a higher water content [8]. S2000 was subjected to the same gamma doses as I302 but did not display a negative radiation-induced nonlinearity. This suggests that the radiation-induced SA in I302 may be due to the metallic impurities, specifically aluminium (Al $\simeq$ 20 ppm), induced by the manufacturing process. Al-oxygen-hole-centers generated by gamma irradiation have been shown to cause an absorption band at 537 nm which may be responsible for the absorption and SA observed [43].

Neutron irradiated S2000, I302, sapphire, NBK7, and BK7G18 all exhibit negative NLA at 532 nm for nanosecond pulse duration, which could be attributed to the simultaneous effects of ultrafast TPA nonlinearity and the slow SA nonlinearity. These negative nonlinearities accompany radiation-induced linear attenuation, which we observed in the recent experiments with gamma-irradiation of quartz glass [65]. The negative NLA acts to compensate some of the radiation-induced linear absorption. S2000 and I302 each have trace elements of aluminium at $\leq$ 10 ppb and $\approx$ 20 ppm, respectively, and sapphire is composed of crystalline Al_2O_3. Al-oxygen-hole-centers generated by gamma irradiation

have been shown to cause an absorption band at 537 nm (FWHM 152 nm), which may be responsible for the radiation-induced linear absorption in S2000, I302, and sapphire, and may also result in the SA effect resulting in negative nonlinear absorption [43, 58]. The difference in the magnitude of the NLA between S2000 and I302 may be associated with the significantly greater concentration of aluminium in I302. The reason that I302 requires 600 °C to anneal, and that it retains a negative NLA coefficient during concurrent-irradiation thermal annealing, may be due to the low-OH content and inability to passivate E' centers because of the lack of mobile OH, and instead annealing the Al-oxygen-hole-centers centers by means of electron and hole excitation [42]. Sapphire undergoes development of and transition to multiple types of oxygen vacancy site F-centers due to neutron and gamma irradiation and thermal annealing [64, 65]. The complex development and annealing of multiple types of F-centers may explain the fact that sapphire exhibits a small negative NLA magnitude at 532 nm compared to I302, even though it is primarily composed of aluminium and oxygen.

NBK7 is a lead and arsenic-free version of BK7 borosilicate glass. NBK7 sensitivity to radiation-induced attenuation and darkening is well known, and it is not surprising therefore that with significant radiation-induced attenuation NBK7 also exhibits the greatest NLA effect in all of the samples measurement [47]. It is interesting to compare the nonlinear response of NBK7 to BK7G18. BK7G18 is 1.8 w% cerium doped to achieve radiation resistance. The cerium may be responsible for the significantly reduced negative nonlinearity compared to the NBK7 measurement, but it is also notable that *in-situ* measurements of irradiated BK7G18 have revealed that radiation induced attenuation in BK7G18 exceeds that of NBK7 during irradiation [47]. The cerium doping does not negate the radiation damage in BK7G18 but makes the damage more thermally unstable and assists the annealing process, so that it is possible BK7G18 may exhibit a significant NLA effect when under irradiation. Finally, the observable NLR in BK7G18 may by pro-

moted by the cerium doping as that is the most significant difference from NBK7 which had an uninterpreted NLR Z-scan similar to the other samples.

Photobleaching has also been observed within low-OH content I302, NBK7, and BK7G18. Photobleaching makes a minor contribution to the observed negative nonlinearity, evident by the fact that all the Z-scan curves restore back to unity transmission after the sample transits the point of maximum intensity (position 0 mm). The photobleaching may provide a small annealing-like effect induced by the high-intensity laser pulse that, in conjunction with SA, reduces the radiation-induced attenuation losses.

Chapter 6

Conclusion

6.1 Summary and Conclusion

Fused silica, sapphire, and borosilicate glass have all demonstrated novel linear and nonlinear optical characteristics under conditions of post and concurrent-irradiation thermal annealing that recommend their successful application as supporting components of optical instruments for fission reactors. High-OH and high-purity content S2000 fused silica demonstrated the strongest resistance to RIA throughout the experiments, and exhibit a small negative NLA coefficient after neutron irradiation to 1.7×10^{17} n $\cdot$ cm^{-2}. S2000 under concurrent-irradiation thermal annealing exhibited no perceptible radiation-induced change to its nonlinear optical properties. By comparison, low-OH content I302 fused silica exhibited significant RIA and radiation-induced negative NLA under concurrent-irradiation thermal annealing. I302 demonstrated the competition between annealing and damage mechanisms under concurrent-irradiation thermal annealing for the dose rates in this research, and is a useful comparison to S2000 which again demonstrated significant resistance to radiation damage. Sapphire, similar to S2000, was resistant to radiation damage under concurrent-irradiation thermal annealing for LIBS wavelengths of interest at 532 nm and 1064 nm. However, sapphire exhibits RIA peaks in the ultraviolet (UV)

due to the competing generation and annealing of various F-centers which may have an impact on the spectroscopy portion of a LIBS instrument, as would the residual spectra observed in I302.

The radiation-induced negative NLA coefficient observed in all materials tested is a significant discovery of this research and has promising implications not only for optical instrumentation of fission reactors, but also for inertial confinement fusion and space fusion propulsion where energy efficiency is important. The presence of a negative NLA coefficient implies that a portion of the RIA may be compensated for by increased intensity of the light transmitting the irradiated material. The presence of radiation-induced negative NLA could benefit laser-driven inertial fusion applications by allowing a greater laser energy to be transmitted through any final focusing optics that would be exposed to fast neutrons abundantly produced in the target chamber. The radiation-induced negative NLA was observed in all materials tested and was proportional to the RIA, suggesting that many optical materials have some capacity to compensate a portion of the RIA with increased applied laser intensity. The benefit gained from a negative NLA is limited however by the intensity damage threshold of the material, which was found to remain constant throughout the irradiations for each material. Based on the results presented here the negative NLA can not fully compensate for the RIA, but it does negate a significant portion.

In all of the materials except for BK7G18, the post irradiation measurements of NLR in the presence of strong negative NLA were inconsistent and were not able to be resolved by Z-scan simulation. That is likely due to the strong influence of NLA on the closed aperture Z-scan measurement. Attempts were made to resolve the closed aperture measurement using the NLA as background according to literature but were unsuccessful [13]. Another limitation to this study is the resolution of the contribution of photobleaching to enhancing the observed negative NLA due to high intensity laser

exposure. The negative nonlinear absorption coefficient was observed to continuously improve transmission through the sample with sustained high intensity laser pulsing through the sample. This effect was tested over three hours in NBK7 and while the rate of transmission increase did slow down, it did not entirely stop. The photobleaching process may be annealing the the volume of the material exposed to the focused and high intensity Z-scan laser, thus enhancing the linear transmission which is reflected in an enhanced negative NLA.

6.2 Future Work

This research has begun to explore the knowledge gap of radiation and thermal effects on nonlinear optical properties to inform the development of novel optical spectroscopic sensors for advanced fission reactors. The dose rates of this research were limited based on the facilities available at the OSU NRL and PSU RSEC, and the temperatures were limited based on the melting points of the materials and the operating temperatures of fast fission reactors. Additional similar research may be beneficial for higher dose rates and temperatures to examine further the competition between damage and annealing effects for different environments, such as may be experienced in inertial confinement fusion. For example, the performance of sapphire at higher doses and temperatures may be interesting to study for high-temperature applications due to its higher melting point than fused-silica and its favorable mechanical properties.

Photobleaching was observed in low-OH content I302, sapphire, NBK7, and BK7G18. Photobleaching makes a minor contribution to the observed negative nonlinearity, and may provide a small annealing-like effect induced by the high-intensity laser pulse that, in conjunction with SA, reduces the RIA losses. The photobleaching effect found in this study also warrants further investigation. Photobleaching studies of each of the

materials may be conducted over time frames greater than 3-hours using the Z-scan with the sample positioned on the z-axis at the point of greatest transmission. At this position the laser may be left to continuously pulse through the sample to observe the enhancement of transmission over time to determine better how the rate of photobleaching changes. The contribution of photobleaching to the reduction of RIA may also be studied with a continuous-wave (CW) laser of the same wavelength as the Z-scan laser, and same diameter as the Z-scan laser at maximum focus, transmitted on the same path as the Z-scan. The CW laser passed on the same path as the Z-scan can be used to measure the change in linear transmission caused by potential annealing from photobleaching induced by the high intensity Z-scan laser by measuring the linear transmission at various times during continuous pulsing of the Z-scan laser through he sample positioned for maximum nonlinear transmission. The use of a laser of the same diameter of the Z-scan laser at maximum focus is necessary because the photobleaching effect is confined to only the volume of the sample within the path of the Z-scan laser. The laser at maximum focus in nearly 34 μm in diameter. The light beam passed through the optical sample for linear transmission measurements is 5 mm in diameter, meaning the Z-scan laser cross-section area is only 0.005 % of the cross-section of the linear transmission measurement. The sample volume photobleached by the Z-scan laser is likely too small to produce a detectable change in linear transmission measured by the spectroscopy beam of 5 mm diameter, hence a CW laser with a diameter matching that of the Z-scan laser can be used to precisely measure the linear transmission on the Z-scan path.

The temporal duration of the negative NLA effect may also be measured with a CW 'probe' laser, again of the same wavelength and diameter of the Z-scan laser, and a slow photodiode with a rise and recover time greater than the duration of the nonlinear mechanism. The probe laser should be the same wavelength as the Z-scan laser because nonlinear effects are dependent on wavelength and pulse duration and light of a separate

wavelength may not experience the induced nonlinear effects. The Z-scan laser can then be pulsed through the optical sample with the sample located at the position of maximum transmission. Simultaneously the CW laser is transmitted co-axially with the Z-scan laser and the diode is triggered by the Z-scan laser. Polarizers and half wave plates can be used to condition and separate the CW laser from the Z-scan laser, both of the same wavelength, so that only the CW laser is incident upon the photodiode. Finally, the change in transmission over time of the CW laser following the induction of nonlinear effects by the Z-scan laser is measured by the triggered photodiode to determine the temporal duration of the negative NLA. Fast nonlinearities may also be measured in this manner by using a picosecond or femtosecond pulsed laser in the Z-scan, which would negate the effects of slow nonlinearities.

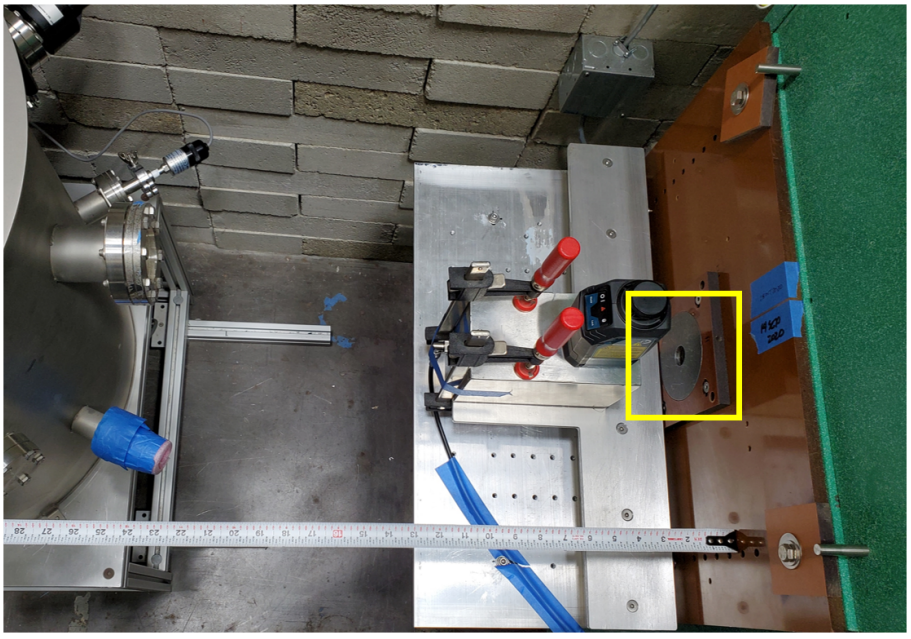

Figure 6.1: The OSU NRL 1.25 inch diameter external beam port to the research reactor. The port aperture is denoted by the yellow box.

The PIE system can be improved to provide a truly *in-situ* measurement of the nonlinear properties of the irradiated, and thermally annealed, optical samples. While it may be impractical to place a Z-scan experiment within the dry-tubes of the ^{60}Co

irradiator or nuclear reactor, the OSU NRL and other facilities posses beam ports which allow the projection of slow and fast neutron fluxes, with or without gamma filtering, onto targets external to the reactor, as shown in Figure 6.1. Beam ports have work spaces external to the reactor that would accommodate the optics for translation of an optical sample and passage of a laser through the optical sample for Z-scan. The majority of the optical table space for the current PIE setup is consumed with beam conditioning and power modulation optics. Integration of a Gaussian laser would reduce the size of the Z-scan experiment, but regardless only the focusing lens, sample translation stage, and necessary mirror to steer the laser beam need be placed within the beam port. The photodiodes are compact enough to easily fit within the beam port work area as well to reduce the complexity of the experiment. A compact furnace may even be manufactured that allows passage of the Z-scan laser to the sample to perform concurrent-irradiation thermal annealing experiments.

References

[1] J. F. Latkowski, A. Kubota, M. J. Caturla, S. N. Dixit, J. A. Speth, and S. A. Payne, "Fused silica final optics for inertial fusion energy: radiation studies and system-level analysis," *Fusion Science and Technology*, vol. 43, no. 4, pp. 540–558, 2003.

[2] M. Burger, L. Garrett, A. J. Burak, V. Petrov, A. Manera, P. Sabharwall, X. Sun, and I. Jovanovic, "Trace xenon detection in helium environment via laser-induced breakdown spectroscopy," *Journal of Analytical Atomic Spectrometry*, vol. 36, pp. 824–828, 2021.

[3] E. Colby, G. Lum, T. Plettner, and J. Spencer, "Gamma radiation studies on optical materials," *IEEE Transactions on Nuclear Science*, vol. 49, no. 6, pp. 2857–2867, 2002.

[4] C. D. Orth, "Vista – a vehicle for interplanetary space transport application powered by inertial confinement fusion," tech. rep., Lawrence Livermore National Laboratory, 03 2003.

[5] D. A. Cremers and L. J. Radziemski, *Handbook of Laser-Induced Breakdown Spectroscopy*. West Sussex, UK: John Wiley & Sons, Ltd., 2013.

[6] A. Williams and S. Phongikaroon, "Laser-induced breakdown spectroscopy (libs) measurement of uranium in molten salt," *Applied Spectroscopy*, vol. 72, no. 7, pp. 1029–1039, 2018.

[7] L. L. Chase and E. W. V. Stryland, *Handbook of Laser Science and Technology Supplement 2: Optical Materials*, vol. 2, pp. 269–366. New York: CRC Press, 5 ed., 1995.

[8] R. Kitamura, L. Pilon, and M. Jonasz, "Optical constants of silica glass from extreme ultraviolet to far infrared at near room temperature," *Applied Optics*, vol. 46, no. 33, pp. 8118–8133, 2007.

[9] P. W. Levy, "Color centers and radiation-induced defects in Al_2O_3," *Physical Review*, vol. 123, no. 4, p. 1226, 1961.

[10] W. Primak and E. Edwards, "Radiation-induced dilatations in vitreous silica," *Physical Review*, vol. 128, pp. 2580–2588, Dec 1962.

[11] S. Girard, J. Kuhnhenn, A. Gusarov, B. Brichard, M. V. Uffelen, Y. Ouerdane, A. Boukenter, and C. Marcandella, "Radiation effects on silica-based optical fibers: Recent advances and future challenges," *IEEE Transactions on Nuclear Science*, vol. 60, pp. 2015–2036, 2013.

[12] M. Sheik-bahae, A. A. Said, and E. V. Stryland, "High-sensitivity, single-beam n_2 measurements," *Optics Letters*, vol. 14, pp. 955–957, September 1989.

[13] E. V. Stryland and M. Shiek-Bahae, *Z-Scan Measurements of Optical Nonlinearities*. New York: Marcel Dekker, Inc., 1998.

[14] C. Giuliano and L. Hess, "Nonlinear absorption of light: Optical saturation of electronic transitions in organic molecules with high intensity laser radiation," *IEEE Journal of Quantum Electronics*, vol. 3, no. 8, pp. 358–367, 1991.

[15] F. Billard, T. Olivier, and H. Akhouayri, "Study and experimental setting of the z-scan method for accurate nonlinear refractive index and absorption metrology," *Proceedings SPIE*, vol. 5273, 2004.

[16] D. J. Musgraves, J. Hu, and L. Calvez, eds., *Springer Handbook of Glass*, pp. 169–191. Gewerbestrasse 11, 6330 Cham, Switzerland: Springer International Publishing, 2019.

[17] R. A. Fisher, P. L. Kelley, and T. K. Gustafson, "Subpicosecond pulse generation using the optical kerr effect," *Applied Physics Letters*, vol. 14, no. 4, pp. 140–143, 1969.

[18] J. F. Ward and G. H. C. New, "Optical third harmonic generation in gases by a focused laser beam," *Physical Review Letters*, vol. 185, pp. 57–72, 1969.

[19] M. N. Polyanskiy, "Refractive index database." `https://refractiveindex.info`. Accessed on 2022-04-25.

[20] W. Primak and J. Luthra, "Radiation induced expansion and increase in refractive index of magnesium oxide; evidence for the **F** center," *Physical Review*, vol. 150, pp. 551–561, Oct 1966.

[21] K. S. Chiang, "Intermodal dispersion in two-core optical fibers," *Optics Letters*, vol. 20, no. 9, pp. 997–999, 1995.

[22] M. Liu, K. S. Chiang, and P. Shum, "Evaluation of intermodal dispersion in a two-core fiber with non-identical cores," *Optics Communications*, vol. 219, no. 1, pp. 171–176, 2003.

[23] T. H. Maiman, *1960. Stimulated optical radiation in ruby*, pp. 113–114. Chicago, IL, USA: University of Chicago Press, 2005.

[24] G. J. Pogatshnik, Y. Chen, and B. D. Evans, "A model of lattice defects in sapphire," *IEEE Transactions on Nuclear Science*, vol. 34, no. 6, pp. 1709–1712, 1987.

[25] J. Wen, G.-D. Peng, W. Luo, Z. Xiao, Z. Chen, and T. Wang, "Gamma irradiation effect on rayleigh scattering in low water peak single-mode optical fibers," *Optics Express*, vol. 19, no. 23, pp. 23271–23278, 2011.

[26] E. Caglioti, S. Trillo, S. Wabnitz, and G. I. Stegeman, "Limitations to all-optical switching using nonlinear couplers in the presence of linear and nonlinear absorption and saturation," *Journal of the Optical Society of America B*, vol. 5, no. 2, pp. 472–482, 1988.

[27] J. Olesiak-Banska, M. Waszkielewicz, K. Matczyszyn, and M. Samoc, "A closer look at two-photon absorption, absorption saturation and nonlinear refraction in gold nanoclusters," *RSC Advances*, vol. 6, pp. 98748–98752, 2016.

[28] P. Rairoux, H. Schillinger, S. Niedermeier, M. Rodriguez, F. Ronneberger, R. Sauerbrey, B. Stein, D. Waite, C. W. H. Wille, L. Wöste, , and C. Ziener, "Remote sensing of the atmosphere using ultrashort laser pulses," *Applied Physics B*, vol. 71, no. 4, pp. 573–580, 2000.

[29] A. E. Kaplan, "'external' self-focusing of light by a nonlinear layer," *Radiophysics and Quantum Electronics*, vol. 12, no. 6, pp. 692–696, 1999.

[30] A. Dragomir, J. G. McInerney, and D. N. Nikogosyan, "Two-photon absorption properties of commercial fused silica and germanosilicate glass at 264 nm," *Applied Physics Letters*, vol. 80, no. 7, pp. 1114–1116, 2002.

[31] Y.-L. Huang, C.-K. Sun, J.-C. Liang, S. Keller, M. P. Mack, U. K. Mishra, and S. P. DenBaars, "Femtosecond z-scan measurement of **GaN**," *Applied Physics Letters*, vol. 75, no. 22, pp. 3524–3526, 1999.

[32] T. Miyoshi, N. Matsuo, P. Maly, F. Trojanek, P. Nemec, and J. Kudrna, "Negative and positive nonlinear absorption in **CdS**-doped glasses," *Journal of Materials Science Letters*, vol. 20, pp. 343–345, 2001.

[33] A. Scalisi, G. Compagnini, L. D'Urso, and O. Puglisi, "Nonlinear optical activity in **Ag**–**SiO2** nanocomposite thin films with different silver concentration," *Applied Surface Science*, vol. 226, no. 1, pp. 237–241, 2004.

[34] V. Sreeja, A. Cheruvalathu, R. Reshmi, E. Anila, S. Thomas, and M. Jayaraj, "Effect of thickness on nonlinear absorption properties of graphite oxide thin films," *Optical Materials*, vol. 60, pp. 450–455, 2016.

[35] B. W. Morgan, M. P. Van Zile, P. Sabharwall, M. Burger, and I. Jovanovic, "Gamma-radiation-induced negative nonlinear absorption in quartz glass," *Optical Materials Express*, vol. 12, pp. 1188–1197, 2022.

[36] A. Thilagam, "Pauli blocking effects in quantum wells," *Physical Review B*, vol. 59, no. 4, pp. 3027–3032, 1999.

[37] J. Wang, B. Gu, H.-T. Wang, and X.-W. Ni, "Z-scan analytical theory for material with saturable absorption and two-photon absorption," *Optics Communications*, vol. 283, no. 18, pp. 3525–2528, 2010.

[38] M. C. Nuss, W. Zinth, and W. Kaiser, "Femtosecond carrier relaxation in semiconductor-doped glasses," *Applied Physics Letters*, vol. 49, no. 25, pp. 1717–1719, 1986.

[39] Q. Bao, H. Zhang, Y. Wang, Z. Ni, Y. Yan, Z. X. Shen, K. P. Loh, and D. Y. Tang, "Atomic-layer graphene as a saturable absorber for ultrafast pulsed lasers," *Advanced Functional Materials*, vol. 19, no. 19, pp. 3077–3083, 2009.

[40] H. I. Elim, J. Yang, J.-Y. Lee, J. Mi, and W. Ji, "Observation of saturable and reverse-saturable absorption at longitudinal surface plasmon resonance in gold nanorods," *Applied Physics Letters*, vol. 88, no. 8, p. 083107, 2006.

[41] L. N. Skuja, A. N. Streletsky, and A. B. Pakovich, "A new intrinsic defect in amorphous siO_2: Twofold coordinated silicon," *Solid State Communications*, vol. 50, no. 12, pp. 1069–1072, 1984.

[42] P. Martín, M. León, A. Ibarra, and E. R. Hodgson, "Thermal stability of gamma irradiation induced defects for different fused silica," *Journal of Nuclear Materials*, vol. 417, no. 1-3, pp. 818–821, 2011.

[43] H. Hosono and H. Kawazoe, "Radiation-induced coloring and paramagnetic centers in synthetic siO_2:Al glasses," *Nuclear Instruments and Methods in Physics Research Section B: Beam Interactions with Materials and Atoms*, vol. 91, no. 1, pp. 395–399, 1994.

[44] L. Skuja, K. Kajihara, M. Hirano, and H. Hosono, "Visible to vacuum-UV range optical absorption of oxygen dangling bonds in amorphous SiO_2," *Physical Review B*, vol. 84, p. 205206, 2011.

[45] L. Skuja, M. Hirano, H. Hosono, and K. Kajihara, "Defects in oxide glasses," *Physica Status Solidi C*, vol. 2, no. 1, pp. 15–24, 2005.

[46] H. Bach and N. Neuroth, eds., *The properties of optical glass*. Berlin, Heidelberg: Springer, 1998.

[47] S. Girard, T. Allanche, P. Paillet, V. Goiffon, M. V. Uffelen, L. Mont-Casellas, C. Muller, A. Boukenter, Y. Ouerdane, and W. D. Cock, "Growth and decay kinetics of radiation-induced attenuation in bulk optical materials," *IEEE Transactions on Nuclear Science*, vol. 65, no. 8, pp. 1612–1618, 2017.

[48] G. P. Pells, "Radiation damage effects in alumina," *Journal of the American Ceramic Society*, vol. 77, no. 2, pp. 368–377, 1994.

[49] M. Izerrouken and T. Benyahia, "Absorption and photoluminescence study of al2o3 single crystal irradiated with fast neutrons," *Nuclear Instruments and Methods in Physics Research Section B: Beam Interactions with Materials and Atoms*, vol. 268, no. 19, pp. 2987–2990, 2010.

[50] C. M. Petrie, A. Birri, and T. E. Blue, "Optical transmission and dimensional stability of single-crystal sapphire after high-dose neutron irradiation at various temperatures up to 688 °C," *Journal of Nuclear Materials*, vol. 559, p. 153432, 2022.

[51] S. V. Solov'ev, I. I. Milman, and A. I. Syurdo, "Thermal- and photo-induced transformations of luminescence centers in α-Al_2O_3 anion-defective crystals," *Physics of the Solid State*, vol. 54, no. 4, pp. 726–734, 2012.

[52] C. M. Petrie, A. Birri, and T. E. Blue, "High-dose temperature-dependent neutron irradiation effects on the optical transmission and dimensional stability of amorphous fused silica," *Journal of Non-Crystalline Solids*, vol. 525, p. 119668, 2019.

[53] R. D. Guenther, ed., *Encyclopedia of Modern Optics*, pp. 247–256. Oxford, UK: Elsevier, 2005.

[54] T. Olivier, F. Billard, and H. Akhouayri, "Z-scan studies of the nonlinear refractive index of fused silica in the nanosecond regime," *Proceedings SPIE*, vol. 5252, pp. 391–401, 2004.

[55] P. B. Chapple, J. Staromlynska, J. A. Hermann, and T. J. McKay, "Single-beam z-scan: Measurement techniques and analysis," *Journal of Nonlinear Optical Physics and Materials*, vol. 6, no. 3, pp. 251–293, 1997.

[56] B. W. Morgan, M. Van Zile, P. Sabharwall, M. Burger, and I. Jovanovic, "Post-irradiation examination of optical components for advanced fission reactor instrumentation," *Review of Scientific Instruments*, vol. 90, no. 10, p. 105107, 2021.

[57] J. A. Hermann and R. G. McDuff, "Analysis of spatial scanning with thick optically nonlinear media," *Journal of the Optical Society of America B*, vol. 10, no. 11, pp. 2056–2064, 1993.

[58] C. D. Marshall, J. A. Speth, and S. A. Payne, "Induced optical absorption in gamma, neutron and ultraviolet irradiated fused quartz and silica," *Journal of Non-Crystalline Solids*, vol. 212, pp. 59–73, 1997.

[59] A. E. Siegman, "How to (maybe) measure laser beam quality," in *DPSS (Diode Pumped Solid State) Lasers: Applications and Issues*, (Oxford, UK), pp. 247–256, Optica Publishing Group, 1998.

[60] S. White, "Neutron Spectrum Measurement within the 6.5-inch Tube Furnace," tech. rep., The Ohio State University, 09 2021.

[61] M. P. Van Zile, *Performance of a Silicon-carbide Heated Furnace and Activation at High Neutron Flux*. Ohio State University, 2020.

[62] D. P. Hawn, C. M. Petrie, T. E. Blue, and W. Windl, "In-situ gamma radiation induced attenuation in silica optical fibers heated up to 600°C," *Journal of Non-Crystalline Solids*, vol. 379, pp. 192–200, 2013.

[63] S. Girard, T. Allanche, P. Paillet, V. Goiffon, M. V. Uffelen, L. Mont-Casellas, C. Muller, A. Boukenter, Y. Ouerdane, and W. D. Cock, "Overview of radiation induced point defects in silica-based optical fibers," *Reviews in Physics*, vol. 4, p. 100032, 2019.

[64] M. Itou, A. Fujiwara, and T. Uchino, "Reversible photoinduced interconversion of color centers in α-Al_2O_3 prepared under vacuum," *The Journal of Physical Chemistry C*, vol. 113, no. 49, pp. 20949–20957, 2009.

[65] B. W. Morgan, M. P. Van Zile, C. M. Petrie, P. Sabharwall, M. Burger, and I. Jovanovic, "Optical absorption of fused silica and sapphire exposed to neutron and gamma radiation with simultaneous thermal annealing," *Under review*, 2022.